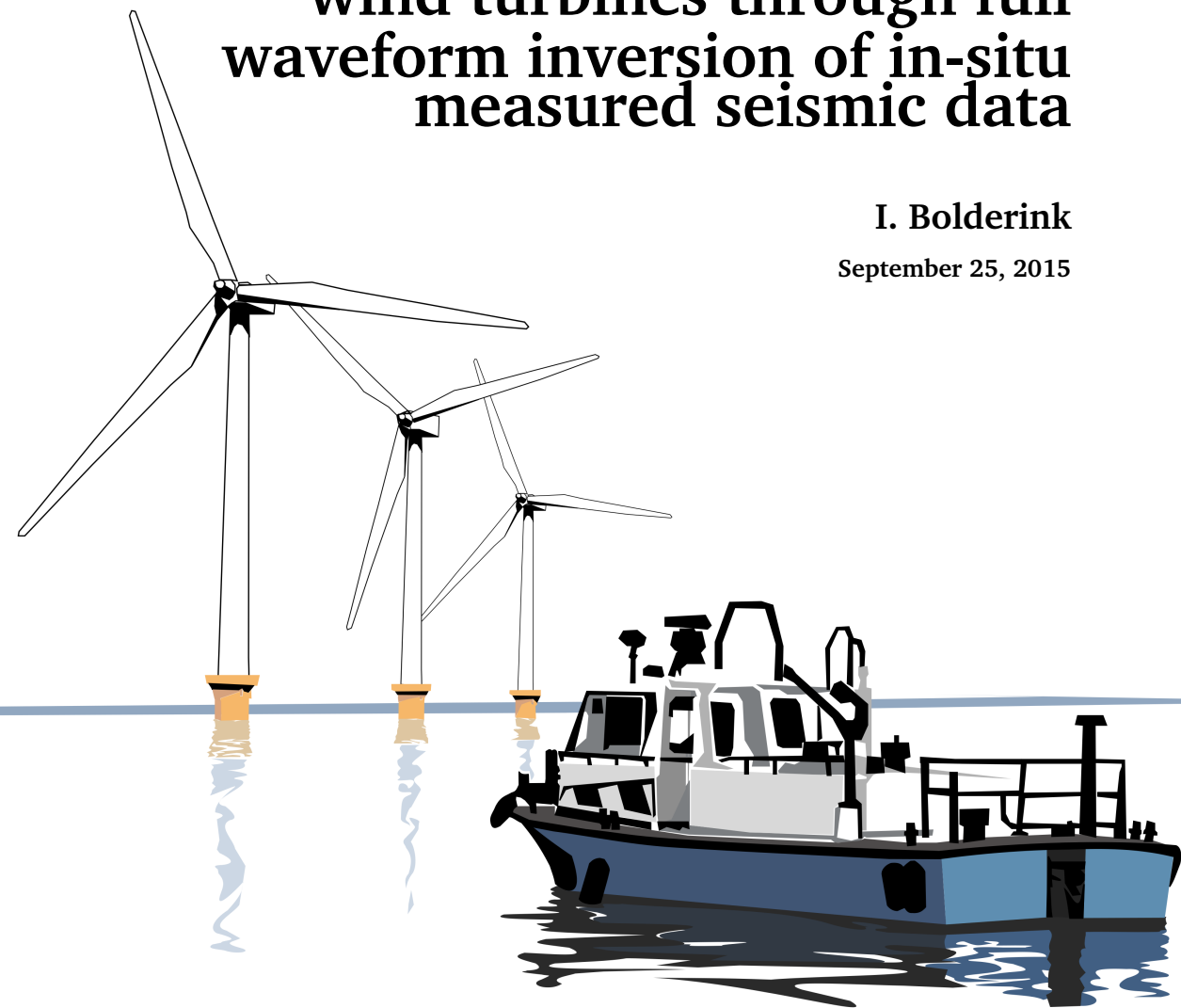


Identification of dynamic soil properties relevant for offshore wind turbines through full waveform inversion of in-situ measured seismic data

I. Bolderink

September 25, 2015



Identification of dynamic soil properties relevant for offshore wind turbines through full waveform inversion of in-situ measured seismic data

Master of Science Thesis

Author: I. Bolderink

supervisor Prof.dr. A. Metrikine TU Delft
Dr. ir. D.J. Verschuur TU Delft
Dr. ir. K.N. van Dalen TU Delft
Ir. W.G. Versteijlen Siemens Wind Power

September 25, 2015

Summary

Wind energy needs to become cheaper in order to take on the competition with current non-durable energy sources. Innovative design procedures and better understanding of structural behavior are aimed for to improve the current wind turbine design. A better understanding of turbine behavior consists of several fields and one of these fields is soil-structure interaction. Currently input parameters for soil-structure interaction models are based on empirical methods. The objective is to estimate the dynamic soil parameters in the first 50m of soil in an offshore environment.

In this thesis, a non-invasive seismic measurement is performed in order to identify dynamic soil parameters relevant for offshore wind turbines. The seabed surface response of an active source is measured through a streamer of hydrophones and results in a so called shot record. The data obtained from this measurement is used in a newly developed routine that can identify an estimate of the shear wave velocity profile. Furthermore the routine is adapted to incorporate a second unknown parameter, the compressional wave velocity structure. These two parameters are the main contributors to the shear modulus, bulk modulus and Poissons ratio of the soil.

An analytical linear-elastic full-waveform calculation is performed for a homogeneous, isotropic representation of the soil where the soil is assumed to be perfectly horizontally stratified and is overlain by a water layer. A genetic inversion algorithm is then used to update an initial guess of the soil model.

The results show that full waveform inversion has high potential to successfully estimate the complex shear wave profiles. In addition, material damping has a large influence on the shape of the spectrum and should be included in the inversion.

Acknowledgements

Studying in Delft was a challenging experience. When I started my study at the faculty of aerospace engineering, I never would have guessed I would end up in the ground. But at the end of the summer of 2014 I had the opportunity to start at Siemens Windpower on the topic of soil dynamics. I am very grateful for this opportunity and would like to thank David and Pim for trusting me to to the job. The success and fun I had during the final stage of my master's degree was not possible without the many people who helped me.

Karel, thank you for the support you gave throughout the project. Especially in the final stage of the project, this was especially though and I wouldn't have succeeded without your view on the matter. Eric, thank you for the fruitful discussions we had regarding the theory. I think that none of the meetings with you ended in time or stayed within the subject I had in mind. Thank you especially with helping me figure out the measurement data. Pim, thanks for being so patient with me during the many meetings. Thanks for helping me plan the meetings that were absolutely necessary to finish the thesis in time. The weekly discussions we had kept me focused on the goal and gave me good insights in the continuation of the project. Andrei, thank you for finding time in your already busy schedule and for understanding my personal situation.

Gwendolyn thank you for the wise words you gave, never realized that you were the wisest of us three. And I'm really looking forward to the pie you promised to make. Mom and Dad thanks for everything. Furthermore, I would like to thank my fellow "klusheld" for doing all the "shitty" jobs in the weekends. In addition, I want to express my gratitude to the bright side of Siemens Windpower, because I don't think I would have survived the office life in a different atmosphere than the one I was welcomed in. May the loads be with you, always.

Ingmar Bolderink
Delft, september 2015

Contents

Summary	i
Acknowledgements	ii
Nomenclature	vii
1 Introduction	1
1.1 Research objective	1
1.2 Near-surface geophysical measurements	3
1.3 Inversion of seismic data	4
1.4 Thesis outline	5
2 Theory on wave propagation in a 2D continuum	7
2.1 Wavefield components	7
2.1.1 Surface waves	8
2.1.2 Body waves	9
2.2 The wave equations	12
2.2.1 Acoustic wave equation	12
2.2.2 Elastic wave equation	14
2.3 Full waveform response for horizontally stratified soil	17
2.3.1 System of equations	21
2.3.2 Damping	22
2.3.3 Dispersion- or surface response spectrum	23
3 Inversion method and verification	25
3.1 Inversion problem	25
3.1.1 Suitability	25
3.1.2 Inversion method	27
3.2 Results of pressure wave velocity inversion	28
3.3 Impact of finite length measurements	29

3.3.1	Truncation in space and time	29
3.3.2	Shear wave velocity	35
3.3.3	Compressional wave velocity	37
3.4	Summary and conclusions	40
4	Near-surface geophysical measurements in practice	41
4.1	Data acquisition in space-time domain	41
4.1.1	Measurement set-up	42
4.1.2	Locations and background profiles	48
4.1.3	Post processing	49
4.1.4	Concatenation of multiple offsets	50
4.1.5	Reconstruction of concatenated datasets	51
4.2	Spectral analysis	53
4.2.1	2D Fourier domain	53
4.2.2	Restrictions and limitations	53
4.2.3	Limits to wavenumber and frequency	53
4.2.4	Streamer length or aperture	54
4.2.5	Scaling and windowing of the shot record	56
4.3	Summary and conclusions	58
5	Full waveform inversion of in-situ measured seismic data	61
5.1	Measurement data	61
5.2	Initial soil model	63
5.2.1	Damping	64
5.2.2	Impact of RMS scaling	64
5.2.3	Windowed spectra	65
5.2.4	Increase of amount of layers in model	65
5.2.5	Near-surface damping	67
5.2.6	Higher mode surface wave	70
5.3	Inversion of measurement data	72
5.3.1	Inversion runs	72
5.4	Summary and conclusions	84
6	Conclusions	85
7	Recommendations	89

A	Derivation of acoustic and elastic wave equations	93
A.1	Basic relations for wave propagation	93
A.1.1	Conservation of momentum	95
A.1.2	Conservation of mass	96
A.2	Acoustic media	97
A.2.1	Hooke's law in acoustic media	97
A.2.2	The acoustic wave equation	98
A.3	Elastic media	98
A.3.1	The elastic wave equation	100
B	Fourier transforms and conventions	101
B.1	The Fourier transform	101
B.2	Truncation in time and space	102
C	Mathematical conventions	105
C.1	Coordinate system	105
C.2	Calculation of the full wavefield	106
C.3	Einstein summation convention	106
D	A short guide to the numerical inversion tool	107
D.1	Program functions	107
D.2	Program outline	108
D.3	Short explanation of the subroutine	108
D.3.1	Truncation	112
D.4	Basic input and output of the program	115
D.4.1	Input	115
D.4.2	Output	115
E	Additional inversion results	117
E.1	Additional run 1	117
E.2	Additional run 2	121
F	Possible improvements	125
	Bibliography	127

Nomenclature

Latin symbols

p	Pressure	Pa
c	Velocity	ms^{-1}
c_p	P- or compressional wave velocity	ms^{-1}
c_s	S- or Shear wave velocity	ms^{-1}
D	Layer thickness	m
f	Frequency	Hz
\bar{F}	Source vector in full waveform method	N
\bar{f}^{ext}	External source vector (in wave equation)	N
k_x	Wavenumber	m^{-1}
M	Coefficient matrix	
n_f	Number of frequency points used	
n_k	Number of wavenumber points used	
\bar{u}	Displacement vector	m
\bar{v}	Velocity vector	ms^{-1}
X	Aperture or streamer length	m
T	Duration of measurement	s
D_p	P-wave damping ratio	
D_s	S-wave damping ratio	
D_λ	Damping ratio of Lamé's first constant	
D_μ	Damping ratio of Lamé's second constant	
G	Transfer function	

Greek symbols

θ	Angle of incidence of wave	rad
----------	----------------------------	-------

Δx	Receiver spacing	m
Δt	Time discretisation in measurement	s
ϵ	Strain	
η	Viscosity	Nsm^{-2}
κ	Elastic modulus	Nm^2
λ	Lamé's first constant	Nm^{-2}
λ	Wavelength	m
μ	Shear modulus, Lamé's second constant	Nm^{-2}
ρ	Density	kgm^{-3}
ρ_l	Water density	kgm^{-3}
σ	Stress	Nm^{-2}
σ	Standard deviation	
ϕ	Velocity potential	m^2s^{-1}
Φ	Elastic p-wave potential	m^2s^{-1}
ϵ	Stabilization factor, used to stabilize the suitability calculation	
Ψ	Elastic shear wave potential	m^2s^{-1}
ω	Frequency	rad/s

Abbreviations

SRS	Surface response spectrum defined in fk domain
CPT	Cone penetration test
OWT	Offshore wind turbine
FD	Finite difference
FW	Full waveform method
FFT	Fast Fourier transform
p-wave	Primary or compressional-wave
s-wave	Secondary or shear-wave
RMS	Root mean square
Stdv	Standard deviation
<i>suit</i>	Suitability, expression for the fitness of a profile

Chapter 1

Introduction

Windenergy has become a major contributor to the energy problem. The future of windenergy has been questioned publicly, whether it is regarding independency of government subsidies or as seen by many as horizon pollution. Better design of offshore windfarms could pose a solution to many issues regarding windenergy. A better design approach or better understanding of windturbine behavior leads to cheaper designs and would make it possible to install windturbines in deeper waters. Several aspects of windturbine design can be improved. This thesis focuses on one aspect in particular: soil-structure interaction and in particular dynamic soil parameter identification.

1.1 Research objective

Parameters for soil-structure interaction are currently defined through design standards. The need for a better understanding of the soil structure interaction is required, but limited knowledge is available regarding this topic. Siemens Windpower and TU delft have collaborated to gain more insight in matter of soil behavior through the DISSTINCT project. This thesis forms a small part of the overall project and focuses on the identification of dynamic soil properties that could form the input for a improved soil-structure interaction model.

Propagation of waves in acoustic and elastic media are largely governed by the characteristic propagation velocities of the media. In acoustic media, wave propagation is directly related to pressure. No shear can be taken up by such a layer, and hence only pressure waves occur. The pressure wave existing in an acoustic medium is in fact the propagation of sound through this medium. In elastic media, wave propagation is related to the elastic properties of the soil. Perturbations in shear and

normal stress fields cause the existence of two types of waves; compressional waves and shear waves. When the compressional wave velocities and shear wave velocities of the subsoil can be identified, the stiffness of the soil can be identified provided that densities are known.

The research objective of this thesis is described as:

“Is it possible to derive information regarding the dynamic properties of soil from actual measurements through full waveform inversion?”

The properties of interest in this thesis are shear wave speed and pressure wave speed, which are characteristic properties of the soil. These velocities are related to the shear modulus μ , bulk modulus λ , and can be related to the Poisson's ratio ν . The attenuation of a measured wavefield could be used to identify damping properties of the soil; this is not part of this thesis.

Typical frequencies used in seismic inversion research, can range for shear waves from 0-140 Hz and for compression waves the frequency content can even be as high as 3000 Hz [5]. In oil and gas exploration, typical frequency content of 5-150 Hz is used to identify the substratum. The question remains whether the parameters identified can be related to extremely low frequency soil behavior as typically found in offshore wind turbines (OWTs), where the eigenfrequency of the first bending mode is often around 0.3 Hz.

A detailed layered soil profile, with layers with thickness of approximately 1-10m, is required for current design purposes regarding soil-structure interaction. Cone penetration tests (CPTs) and borehole measurements show deposits of clay and peat even smaller than 1m in thickness alternated by thicker sand layers. The question remains whether an inversion parameter identification can be done for the required precision and whether such precision (in scale) is relevant for soil-structure interaction.

The research goal can be subdivided into two sections. The first is related to the practical aspect of the measurement procedure. The second is the actual prediction of shear and compression wave velocities through the application and adaption of a genetic inversion tool designed by de Winter [6].

1.2 Near-surface geophysical measurements

In seismic measurements several options are available to capture the wavefield of the subsoil. In the master thesis of de Winter a discussion was made between a vertical streamer array and horizontal streamer array. Through finite-difference (FD) modeling and literature research a trade-off was made.

One of the first conclusions drawn is the difference in installation. A lack of flexibility of installation of the vertical streamer array is a huge disadvantage for this set-up. The vertical arrays have to be installed in the soil and are not easily replaced. The horizontal receiver arrays however, are noninvasive and can be relocated with ease. The noninvasive nature of the horizontal streamer does not require drilling, and therefore does not disturb the soil.

Another huge advantage for the horizontal streamer is the visibility of the dispersive character of the wavefield in the fk domain. Geometric dispersion is mainly dependent on the shear wave velocity profile of the soil for a few wavelengths deep. A proper visibility of the dispersion is highly beneficial for the success of retracing the velocity profiles. In addition, the p-wave velocity changes could be measured and could be included in the inversion. For these reasons a horizontal streamer is considered in this thesis.

In addition, de Winter looked at the differences between an active and a passive source. From FD modeling it was found that active sources show the best potential. The main disadvantage of a passive source was that a passive source would only work if no knowledge of the source was required for the inversion. For the full waveform inversion (FWI), and in particular the forward calculation of the full waveform, knowledge is required regarding the source. In addition, p-wave events are difficult to retrace from a passive source using a vertical streamer. However, the choice for an active source was mainly based on research done by Socco et. al. [22]. In this article the use of horizontal streamer arrays and active sources are discussed. This article shows that shear wave velocity inversion for near-surface applications are used successfully.

The measurements performed were part of the DISSTINCT project [26]. A collaboration of Fugro Nederland, Fugro France and Siemens Nederland resulted in a seismic measurement of two locations in the Westermeerwind park in the IJsselmeer near Urk. The measurements performed are hydrophone measurements along the

seabed surface, an active source type in the form of an airgun is used to perturb the soil.

1.3 Inversion of seismic data

A typical seismic inversion process consists of the iteration of the following steps:

1. An initial guess of a profile of soil layers with certain elastic properties is defined,
2. From this initial guess, a representation of the wavefield is calculated using a simplified theoretical forward model: the wavefield is described through a measurable quantity; usually velocities, accelerations or pressures (pressure is typically used for offshore conditions),
3. A comparison between the modeled response and measurement data is performed,
4. An update is made of the initial guess based on the differences found in the previous step.

When enough iterations of this loop are performed a corresponding soil profile is the result. A proper soil profile is obtained when a match is found between modeled and measured data. This is only possible when a proper modeling of the soil response is considered. The inversion statement is usually ill-posed and highly non-linear and therefore the forward and initial model are the main contributors to the success of the inversion.

De Winter discussed the use of two different modeling approaches; the surface wave method (SW) and the full waveform (FW) method. The SW method only calculates the modes of the response from the dispersion equation. This method seemed to be too simplistic for our cause: a discrete representation of the location of the surface waves and their dispersive character were the result. The FW method includes the source function in the solution of the forward problem. Reflections, refractions and, near-field effects are included in the response. In addition, the energy distribution over the modes and all other visible phenomena are predicted. The inclusion of other wave phenomena and the energy distribution made the FW method more beneficial, especially since part of the properties to be inverted is the p-wave velocity

profile. This usually requires knowledge regarding reflections and refractions or in general body wave related events.

The compressional wave velocity profile can be obtained from picking refraction arrival times [23]. Refraction methods use the refractive properties at interfaces between two layers and is widely used to estimate the depth and morphology of the bedrock. There are several limitations to this technique caused by hidden layers, gradual velocity variations, and velocity inversions. Foti et al. [11] and Piatti et al. [17] use a joint inversion of seismic refraction and the surface wave method to retrace both p-wave and s-wave velocities. They also state that several limitations of the two techniques can be overcome by this cross interpretation.

Full waveform inversion should not necessarily require the use of two different techniques for shear wave and p-wave velocity inversion since body wave related events are inherent to this modeling technique. In addition, body wave related events should be visible in surface wave measurements (although this might be site specific). Large contrast between layers in a specific soil are more likely to show usable and visible body wave related events at the surface.

Ernst [9] states that the fundamental mode of the Rayleigh wave is not dependent on the p-wave velocity. However, the higher modes are influenced by p-wave velocity. He shows that for a subsurface with thick shallow layers, p-wave velocity can be retraced properly in addition to s-wave velocity and layer thickness. This process works for relatively simple models even when the fundamental mode is non-dispersive. An extension is provided by Boiero et al. [4] who not only includes higher modes of surface waves in the inversion, but also so called acoustic guided modes or p guided waves.

The FWI has as major benefit that it should be able to use all events visible in the surface response spectrum (SRS) including the fundamental mode, its higher modes as well as all body wave related events like acoustic guided modes.

1.4 Thesis outline

The report is structured to provide a good insight in the different steps of the thesis. The subjects discussed in this report can be subdivided into two sections; the first is propagation of waves in a soil, the second is the actual inversion process. For both

sections a distinction can be made between theory and practice.

The first section concerns the wave propagation in a continuum. The theory on wave propagation is discussed in chapter 2. Typical wave phenomena that can be found in a seismic measurement are discussed. After that the description of the model is provided and the full wavefield forward model is explained. This requires the derivation of the so called wave equations for a 2D continuum. Finally, through boundary- and interface conditions a simplified model representation can be given. In this process several assumptions are made and could lead to an improper representation of actual measured data.

In chapter 3 an elaboration will be given regarding the inversion routine. The process of genetic inversion is explained and the objective function is described. Several estimations are done to give a verification of the inversion of s-wave and p-wave velocity profiles of ideal synthetic untruncated and truncated data.

The practical limitations for measuring the wavefield are provided in chapter 4. First, the measurement set-up and measurements performed are discussed. The data processing is briefly summarized, the process of concatenating different datasets is explained and the surface response spectrum (SRS) is provided. Several limitations to the measurements are provided that will be driving factors for the comparison between modeled data. Together with the assumptions made these limitations could provide a good insight in the match between modeled and measured data.

Finally, in chapter 5, the routine is used on the actual measurement data. A starting model is defined that will allow a better match between model and measured data. Several properties of the initial soil model are provided from CPT and borehole measurements and several forward models are discussed. The runs are performed subsequently and are based on the forward models proposed.

Concluding remarks and input for continuation of this research is provided in the chapters 6 and 7.

The appendices contain background information regarding the derivation of the wave equations, mathematical conventions, the inversion program and improvements of the measurements.

Chapter 2

Theory on wave propagation in a 2D continuum

Propagation of waves through a soil media due to an excitation is a characteristic for every soil. Several types of waves and typical wave phenomena occur in a soil and are described briefly in this section. These phenomena can be mathematically described through a coupled set of (potential) wave equations. The model consists of several elastic soil layers with on top an acoustic water layer that overlay a solid elastic halfspace. The full waveform equations are defined for acoustic or elastic media and coupled through certain constraints on the interfaces or boundaries of the layers. This chapter will elaborate on the wave equations and model proposed.

2.1 Wavefield components

The analysis can be done in several domains, in this report the focus lies on the two dimensional Fourier domain. A two dimensional Fourier transform is applied to decompose the measured signal in to a sum of plane waves propagating through the soil, each with their own frequency-wavenumber combination, amplitude, and phase. This decomposition will show the interference between several wave components and the phases of the waves propagating in the soil. A visualization of characteristic interference patterns is the result representing all components of the wavefield, e.g. surface waves, guided modes, multiples, refraction etc.. This will form a characteristic spectrum for the specific soil under the assumption of a horizontally stratified soil representation, and is referred to as dispersion spectrum or surface response spectrum (SRS).

2.1.1 Surface waves

The first subclass of wave phenomena are related to interfacial waves, that are waves propagating parallel to the surface and show an exponential decay in depth. Different kinds of this type of waves can be found in soil, called Rayleigh waves, Scholte waves or Love waves. Love waves are a special type of surface waves since these waves are horizontally confined to the plane of the surface i.e. the particle motion is from side to side. A presentation for the Rayleigh wave and love wave is presented in figure 2.1. This thesis is only concerned with two dimensional representation of the soil, therefore the Love waves will not be considered in this thesis. The other waves have their particle motion out of the plane of the surface i.e. up and downward particle motion. The only difference between them is the difference in interface media. Scholte waves are the offshore equivalent of Rayleigh waves and they converge to Rayleigh waves with decreasing water layer thickness. These waves are usually referred to as surface waves, since these waves propagate parallel to the water-sediment interface. Scholte waves are of significant importance in seismic parameter identification due to so-called geometric dispersion.

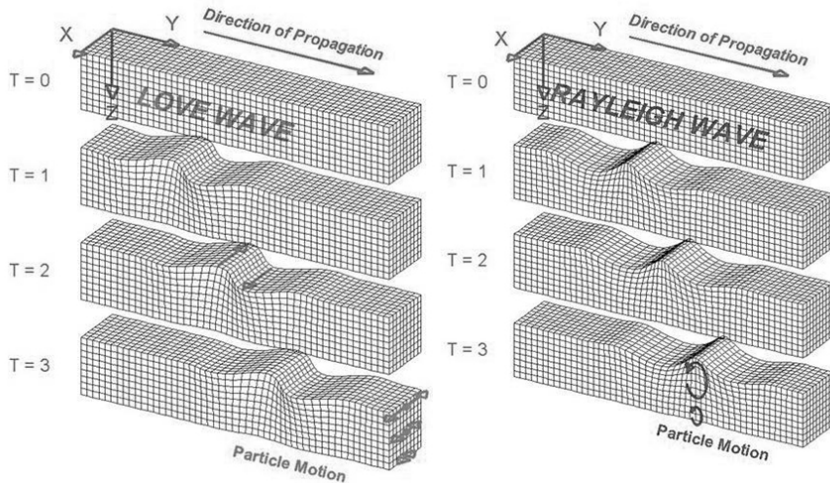


Figure 2.1: Representation of Rayleigh waves and Love waves.

Geometric dispersion of surface waves

Dispersion is the frequency dependency of parameters in general. In the case of geometric dispersion, it is caused by the stratification of the soil. The variability of the several parameters, shear moduli, elastic moduli, layer thickness, and densities give rise to the dispersive nature of surface waves. For surface waves the seismic energy is primarily located in the part of the soil one wavelength deep. Propagation of surface waves can be described by its phase velocity. The phase velocity is the propagation velocity of a certain phase of the wave e.g. the crest or trough and is represented by the division of wave frequency over its corresponding wavenumber, equation 2.1. The phase velocity of waves with longer wavelengths are influenced by more or deeper layers than short waves. Surface waves with different frequencies have different corresponding wavelengths and therefore propagate with different phase velocity. The phase velocity of surface waves is closely related to the shear-wave velocities below the seabed, and hence can be inverted to estimate the shear wave velocity profile in depth.

$$c(f) = \frac{f}{k(f)} = f \cdot \lambda(f) \quad (2.1)$$

Higher modes of surface waves are also present in the soil, they differ in motion behavior and dispersion characteristics and are therefore in a different manner dependent on the stratification of the soil. This can be used to increase the precision of the estimated inversion of the shear wave velocity [28].

2.1.2 Body waves

Next to the waves propagating along interfaces, wave propagation also occurs through the soil body. These waves are referred to as body waves and can be distinguished in two separate wave groups. The first are called primary, compressional, longitudinal or simply p-waves and the second are called secondary, transverse, shear waves or in short s-waves. The distinction between the two can be made by comparing the particle motion with respect to the direction of propagation.

The particle motion of p-waves is in the direction of propagation and caused by either a pressure or normal stress depending on the medium. For shear waves the particle motion is perpendicular to the wave propagation and the distortion is caused by shear stresses. The difference between the two is graphically represented in figure 2.2 to clarify these differences.

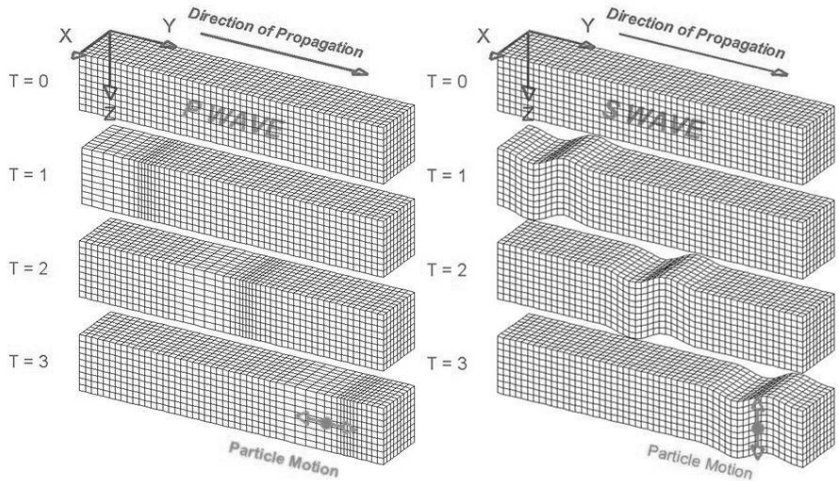


Figure 2.2: Representation of the two types of body waves

Reflection, refraction and Snell's law

In a homogeneous medium, waves propagate in three dimensions and will spread out like spheres, where the outer shell of the sphere is referred to as the wavefront. Another way to interpret wave propagation is normal to the wavefront, this is referred to as the ray concept. The ray concept is of fundamental value in seismic investigation, especially when soil consists of multiple layers of different soil types. When a wave front meets a boundary, some energy is transmitted through the boundary and some energy is reflected; the amount of energy is completely dependent on the differences between the two layers. Ray parameters make it easier to interpret the process of refraction and reflection. The concept of Ray parameter can be interpreted by the relation between the angle of incidence of an incoming wave and the characteristic wave velocities in the two neighboring media, see figure 2.3. This can be represented in equation form as:

$$\frac{\sin \theta_1}{c_1} = \frac{\sin \theta_2}{c_2} \quad (2.2)$$

Where θ and c are the wave angles with the vertical and c the wave velocity of the media. The terms on both sides of the equality are referred to as the *ray parameter*. The general form of equation 2.2 also holds for the two characteristic wave velocities

that exist in a medium; the shear wave speed, c_s and compressional wave speed, c_p .

$$\frac{\sin \theta_p}{c_p} = \frac{\sin \theta_s}{c_s} \quad (2.3)$$

This results in the fact that an incoming p-wave at an interface between two layers, reflects a p-wave and an s-wave and also transmits a p-wave and an s-wave. Moreover, an incoming s-wave reflects a p-wave and a s-wave and transmits a p-wave and a s-wave.

A special case of Snell's law occurs when the angle of the incoming wave is equal or lower than the critical angle. Below this critical angle evanescent waves occurs, the wave is not transmitted into the media but propagates along the boundary. When the wave velocity of the upper wave is smaller than the velocity of the wave traveling in the interface refraction occurs.

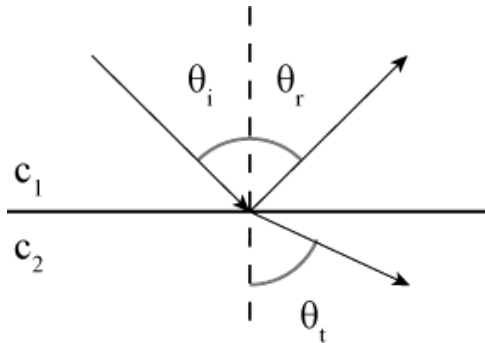


Figure 2.3: Representation of Snell's law.

The body waves propagating through the soil are reflected at boundaries and interfaces. So depending on the soil parameters the waves are reflected and refracted in a certain manner. This results in a characteristic interference pattern in the fk domain. Three different waves can be distinguished: direct arrivals, reflections, and refraction. Commonly, in the characterization of the near-surface, reflection and refraction methods are utilized.

Body wave related events

The wavefield in a soil is completely dependent on interference between waves found in the soil. Interference between evanescent waves, waves that propagate parallel to the interfaces and show an exponential decay in depth, form the surface waves. In addition, interference between body waves also show typical interference patterns. The complexity of the wavefield is due to the reflected, refracted p- and s-waves. Some other phenomena are guided elastic- and/or acoustic modes and leaking modes.

Guided waves are reflected multiples that travel in layers separated from the surrounding medium by high-velocity contrast and therefore are a common phenomenon of wave propagation of layered media [8]. The main property of guided waves is their dispersive character. Guided waves have proven to contain significant data regarding the p-wave velocity profile of seabed and land seismic data. It is stated that these guided waves can either improve or replace the current reflection and refraction seismic methods [3] and [16].

Guided s-waves have slower phase velocities and in the f_k spectrum these modes appear as higher modes of wave propagation. However, p-guided waves have larger phase velocities usually higher than the pressure wave velocity of the water layer and show in a different part of the spectrum.

2.2 The wave equations

Soil model

The soil is assumed to consist of several layers that are perfectly horizontally stratified. A liquid water layer is considered to lie on top of a series of solid soil layers that in turn lie on a solid soil halfspace. The soil layers in itself are considered to be homogeneous and isotropic throughout the layer i.e. density, shear wave velocity and compressional wave velocity are constant per layer, see figure 2.4. This model allows the analysis of these parameters through the calculation of the wavefield.

2.2.1 Acoustic wave equation

An acoustic wave runs through an acoustic medium after this medium is excited. This wave is nothing more than a displacement in direction of propagation caused

water	$V_{SW} = 0$	V_{PW}	ρ_W	H_W
	V_{S1}	V_{P1}	ρ_1	H_1
	V_{S2}	V_{P2}	ρ_2	H_2
	(...)			
	V_{Sn}	V_{Sn}	ρ_n	$H = \infty$

Figure 2.4: Schematic representation of the soil model.

by a perturbation of the pressure. The velocity field and pressure are closely related according to the following equation (for a detailed view of this derivation, reference is made to appendix A):

$$\nabla p = -\rho \frac{\partial \bar{v}}{\partial t}. \tag{2.4}$$

In this equation p denotes the pressure field, ρ is the density of the medium and \bar{v} the velocity field. This relation allows us to describe the propagation of a wave in acoustic media in terms of the pressure i.e. the acoustic wave equation can be written in terms of pressure. This results in equation 2.5 as derived in appendix A:

$$\frac{1}{\rho c^2} \frac{\partial^2 p}{\partial t^2} - \nabla \cdot \left(\frac{1}{\rho} \nabla p \right) = 0, \tag{2.5}$$

where c is the acoustic wave propagation velocity or pressure wave velocity. For homogeneous media ρ and c are considered constant, which allows us to simplify equation 2.5;

$$\frac{1}{\rho c^2} \frac{\partial^2 p}{\partial t^2} - \frac{1}{\rho} \nabla^2 p = 0. \tag{2.6}$$

Velocity potential

The velocity field of an acoustic medium can be written in terms of a scalar velocity potential, when assuming that an acoustic media can be resembled as an irrotational field.

$$\bar{v} = \nabla\phi. \quad (2.7)$$

Since pressure and velocity are related through equation 2.4, pressure can be written in terms of the velocity potential.

$$p = -\rho \frac{\partial\phi}{\partial t}. \quad (2.8)$$

And in turn the acoustic wave equation is also described by the velocity potential. A more straightforward to solve equation is the result, for which holds that both pressure and velocity can be written in terms of the velocity potential ϕ .

$$\frac{1}{c^2} \frac{\partial^2\phi}{\partial t^2} - \nabla^2\phi = 0. \quad (2.9)$$

2.2.2 Elastic wave equation

The wave equation for linear-elastic media also needs to take into account the effect of shear stresses. The derivation of the elastic wave equation given in equation 2.10 is provided in appendix A. This wave equation is given in the vector form:

$$\nabla [\lambda (\nabla \cdot \bar{u})] + \nabla \cdot \left[\mu \left(\nabla \bar{u} + (\nabla \bar{u})^T \right) \right] - \rho \frac{\partial^2 \bar{u}}{\partial t^2} = -\bar{f} + \nabla \cdot \bar{\sigma}_{ext}. \quad (2.10)$$

In this equation λ and μ are the Lamé's parameters (μ is also referred to as the shear modulus), f_i is an external volumetric force and σ_{ext} an external stress. If no external forces are considered and the body is assumed to be homogeneous and isotropic (λ and μ are constant), the equation reduces to:

$$\rho \frac{\partial^2 \bar{u}}{\partial t^2} = \lambda \nabla [(\nabla \cdot \bar{u})] + \mu \left[\nabla \cdot \left(\nabla \bar{u} + (\nabla \bar{u})^T \right) \right]. \quad (2.11)$$

Or in an even simpler form:

$$\rho \frac{\partial^2 u}{\partial t^2} = (\lambda + \mu) \nabla (\nabla \cdot \bar{u}) + \mu \nabla^2 \bar{u}. \quad (2.12)$$

In order to solve this equation a scalar and vector potential are introduced; this allows us to separate the solution into a divergence free part and a irrotational part of the equation. The method will result in separate equations of motion for p-waves and s-waves i.e. the wavefield can be written as a superposition of these two types of wave propagation.

Scalar potentials, vector potentials, and the Helmholtz decomposition

The equation of motion will be solved in the Fourier domain, which allows us to define two potential functions that will help us solve the equation of motion as a combination of harmonic waves. Furthermore this transformation allows us to define a scalar potential and vector potential, that make it possible to built up the wavefield as a combination of different types of uncoupled harmonic waves. So applying this transformation results in the frequency domain representation of equation 2.10 in the following form:

$$\rho\omega^2\tilde{u} + (\lambda + \mu) \nabla (\nabla \cdot \tilde{u}) + \mu\nabla^2\tilde{u} = \bar{0}. \quad (2.13)$$

The two wave components can be defined as: the irrotational part of the wavefield $\tilde{u}_{\tilde{\Phi}}$ related to a scalar potential $\tilde{\Phi}$; and the divergence free part of the wavefield $\tilde{u}_{\tilde{\Psi}}$ related to a vector potential $\tilde{\Psi}$. The displacement field can then be written as:

$$\tilde{u} = \tilde{u}_{\tilde{\Phi}} + \tilde{u}_{\tilde{\Psi}} = \frac{1}{\rho\omega^2} \left(\nabla\tilde{\Phi} + \nabla \times \tilde{\Psi} \right). \quad (2.14)$$

This decomposition is referred to as the Helmholtz decomposition theorem [1]. Since the wavefield related to the scalar potential is defined as irrotational the following identity must hold:

$$\nabla \times \tilde{u}_{\tilde{\Phi}} = \frac{1}{\rho\omega^2} \nabla \times \left(\nabla\tilde{\Phi} \right) \equiv 0. \quad (2.15)$$

In mathematical terms this means the curl of this part of the wavefield equals zero. For the divergence free part of the wavefield the divergence must be zero or:

$$\nabla \cdot \tilde{u}_{\tilde{\Psi}} = \frac{1}{\rho\omega^2} \nabla \cdot \left(\nabla \times \tilde{\Psi} \right) \equiv 0. \quad (2.16)$$

Substitute equation 2.14 into the vector wave equation 2.10 and remembering the above mentioned equalities, the wave equation results in the following:

$$\left(\nabla\tilde{\Phi} + \nabla \times \tilde{\Psi} \right) + \frac{(\lambda + \mu)}{\rho\omega^2} \nabla \left(\nabla\tilde{\Phi} \right) + \frac{\mu}{\rho\omega^2} \nabla^2 \left[\nabla \left(\nabla^2\tilde{\Phi} \right) + \nabla \times \left(\nabla^2\tilde{\Psi} \right) \right] = \bar{0}. \quad (2.17)$$

This equation can be solved when separating the two parts for the scalar potential and vector potential:

$$(\lambda + 2\mu)\nabla^2\tilde{\Phi} + \rho\omega^2\tilde{\Phi} = 0, \quad (2.18)$$

$$\mu\nabla^2\tilde{\Psi} + \rho\omega^2\tilde{\Psi} = 0. \quad (2.19)$$

This is point where the characteristic parameters of interest in this thesis are found: the p-wave or irrotational wave propagation velocity c_p and the s-wave or divergence free wave propagation velocity c_s . These are defined as follows:

$$c_p = \sqrt{\frac{\lambda + 2\mu}{\rho}}, \quad (2.20)$$

$$c_s = \sqrt{\frac{\mu}{\rho}}. \quad (2.21)$$

Two dimensional representation

The equations described concern three dimensions. However, in this thesis the soil is simplified to a two dimensional problem. Only depth (z) and a direction along the wave propagation (x) are considered. The model is assumed to be invariant perpendicular to this direction of wave propagation.

So the displacement field shall be written in z and x direction only:

$$\tilde{u}(x, z, \omega) = \tilde{u}_p(x, z, \omega) + \tilde{u}_s(x, z, \omega) = \nabla\tilde{\Phi}(x, z, \omega) + \nabla \times \tilde{\Psi}(x, z, \omega). \quad (2.22)$$

The propagation of p-waves in a 2D medium is described by the following equation of motion:

$$\nabla^2\tilde{\Phi} - \frac{\omega^2}{c_p^2}\tilde{\Phi} = 0. \quad (2.23)$$

When examining the curl of the vector potential more closely, it can be seen that the s-wave propagation velocity only depends on the y direction of the vector potential Ψ_y :

$$\frac{1}{\rho\omega^2}\nabla \times \tilde{\Psi}(x, z, \omega) = \frac{1}{\rho\omega^2} \left(\bar{i} \frac{\partial\Psi_y(x, z, \omega)}{\partial z} + \bar{j} 0 - \bar{k} \frac{\partial\Psi_y(x, z, \omega)}{\partial x} \right). \quad (2.24)$$

The \bar{i}, \bar{j} and \bar{k} and unit vectors in x, y and z direction, respectively. This means that the propagation of s-waves in a 2D medium can be described by the following equation:

$$\nabla^2 \tilde{\Psi}_y - \frac{\omega^2}{c_s^2} \tilde{\Psi}_y = 0. \quad (2.25)$$

2.3 Full waveform response for horizontally stratified soil

The wave equations derived in an earlier stage can only describe a continuous medium. For a layered model these equations describe the wave propagation in the single layers, but nothing is mentioned regarding the discontinuities at the interfaces of the different layers. The coupling between the separate layers is done through so called interface and boundary conditions. These relations describe the manner at which the propagating waves are reflected and refracted at these boundaries. However, before these relations can be formulated the inputs of these relations must be derived. Typically interface- and boundary conditions are described through displacements, stresses and/or pressure.

Pressure and displacements in acoustic layers

A solution to the acoustic wave equation must be proposed in order to obtain pressure, velocities, and/or displacements of an acoustic layer. The wave equation will be solved in the 2D Fourier domain or fk domain by applying the transform to equation 2.5 yields:

$$\left(\frac{\omega}{c}\right)^2 \tilde{\phi} + \frac{\partial^2 \tilde{\phi}}{\partial z^2} - k_x^2 \tilde{\phi} = 0. \quad (2.26)$$

The proposed solution is presented in a form such that an upward propagating wave and a downward propagating wave are present.

$$\tilde{\phi}(\omega, k_x) = a_1 \exp^{-\sqrt{k_x^2 - \frac{\omega^2}{c_p^2}} z} + b_1 \exp^{-\sqrt{k_x^2 - \frac{\omega^2}{c_p^2}} (D_1 - z)}, \quad (2.27)$$

where ω is the radial frequency in rad/s , k_x is the wavenumber (spatial equivalent of frequency) in rad/m , c_p the pressure wave velocity of water in m/s and D_1 is the thickness of the water layer. The amplitudes of the propagating waves a_1 and b_1 are complex-valued and are the only unknown parameters in the acoustic layer. As mentioned earlier the velocity field and pressure of an acoustic medium are completely described by the velocity potential:

$$\bar{v} = \nabla\phi, \quad (2.28)$$

$$p = -\rho \frac{\partial\phi}{\partial t}. \quad (2.29)$$

The 2D fourier representation of the velocity field of a two dimensional wavefield is given by:

$$\tilde{v}_x = -ik_x\tilde{\phi}, \quad (2.30)$$

$$\tilde{v}_z = \frac{\partial\tilde{\phi}}{\partial z}. \quad (2.31)$$

The velocity field is the time derivative of the displacement field. This transformation from the velocity field to the displacement field in the fk domain is in fact a simple division by $i\omega$ (one of the major advantages of the Fourier domain).

$$\tilde{u} = \frac{\tilde{v}}{i\omega}. \quad (2.32)$$

The fk domain representation of pressure can be given in the following form:

$$\tilde{p} = -i\omega\rho_l\tilde{\phi}. \quad (2.33)$$

This representation of pressure shall also be used to represent the surface response of pressure and allows us to compare the modeled response to the hydrophone data.

Stresses and displacements in elastic layers

In a similar manner a solution for the elastic wave equations need to be found before stresses, velocities, and displacements can be formulated. The stresses and displacements can be described in terms of the elastic wave potentials. The elastic wave equations for p-waves and s-waves in the fk domain are given by:

$$\frac{\partial^2 \tilde{\Phi}}{\partial z^2} - k_x^2 \tilde{\Phi} + \frac{\omega^2}{c_p^2} \tilde{\Phi} = 0, \quad (2.34)$$

$$\frac{\partial^2 \tilde{\Phi}_y}{\partial z^2} - k_x^2 \tilde{\Psi}_y + \frac{\omega^2}{c_s^2} \tilde{\Psi}_y = 0. \quad (2.35)$$

Notice that only the spatial Fourier transform needs to be performed since the temporal Fourier transform has already been performed. For the fk domain representation the assumption is made that the waves are fully developed in x direction and in this direction the solution can be seen as a combinations of harmonic waves. The solutions to these equations can be defined in a similar way as the acoustic layer. The solutions per soil layer i can therefore be defined as follows:

$$\tilde{\Phi}_i(\omega, k_x) = a_i \exp\left[-\sqrt{k_x^2 - \frac{\omega^2}{c_{p,i}^2}} z\right] + b_i \exp\left[-\sqrt{k_x^2 - \frac{\omega^2}{c_{p,i}^2}} (Di - z)\right], \quad (2.36)$$

$$\tilde{\Psi}_{y,i}(\omega, k_x) = c_i \exp\left[-\sqrt{k_x^2 - \frac{\omega^2}{c_{s,i}^2}} z\right] + d_i \exp\left[-\sqrt{k_x^2 - \frac{\omega^2}{c_{s,i}^2}} (Di - z)\right]. \quad (2.37)$$

To prevent “exploding” wave amplitudes far away from the source and upward propagating waves into the halfspace, the real part of the exponent is chosen such that $Re\left[\sqrt{k_x^2 - \frac{\omega^2}{c_{p,i}^2}}\right] > 0$. The displacements can be written according to equation 2.38 in terms of the proposed solution as follows:

$$\tilde{u}(\omega, x) = \frac{1}{\rho\omega^2} \left(\nabla \tilde{\Phi} + \nabla \times \tilde{\Psi} \right). \quad (2.38)$$

The fk representation of displacement for the two dimensional case is given by:

$$\tilde{u}_x^i = \frac{1}{\rho\omega} \left(-ik_x \tilde{\Phi}_i - \frac{\partial \tilde{\Psi}_{y,i}}{\partial z} \right), \quad (2.39)$$

$$\tilde{u}_z^i = \frac{1}{\rho\omega^2} \left(\frac{\partial \tilde{\Phi}_i}{\partial z} - ik_x \tilde{\Psi}_{y,i} \right). \quad (2.40)$$

The stresses can be found from Hooke's law for an isotropic elastic medium derived in appendix A. Applying the 2D Fourier transform yields:

$$\tilde{\sigma}_{zz}^i = \frac{\lambda_i}{\rho\omega^2} \left(-k_x^2 \tilde{\Phi}_i + \frac{\partial^2 \tilde{\Psi}_{y,i}}{\partial z^2} \right) + 2 \frac{\mu_i}{\rho\omega^2} \left(\frac{\partial^2 \tilde{\Phi}_i}{\partial z^2} - ik_x \frac{\partial \tilde{\Psi}_{y,i}}{\partial z} \right), \quad (2.41)$$

$$\tilde{\sigma}_{zx}^i = \frac{\mu_i}{\rho\omega^2} \left(-2ik_x \frac{\partial \tilde{\Phi}_i}{\partial z} - k_x^2 \tilde{\Psi}_{y,i} - \frac{\partial^2 \tilde{\Psi}_{y,i}}{\partial z^2} \right). \quad (2.42)$$

Boundary conditions

Now that the displacements, stresses, and pressures for every soil layer are defined, the soil layers can be coupled through a system of equations. The only unknowns are the complex valued amplitudes of the solutions to the wave equations.

The lowermost layer is a specific case, it is considered to be a so called half-space. A halfspace is a layer that extends to infinity, and obeys the Sommerfeld radiation condition. This means that no inward radiation is possible. The amplitudes of the upward going waves of the solutions defined by equations 2.36 are set to zero.

The following boundary and interface conditions are applied:

- Pressure at the free surface equals zero
- No shear stress can be transferred at the soil-liquid interface (shear stress equals zero)
- Continuity of vertical stress at the soil-water interface
- Continuity of horizontal displacements at the soil-liquid interface

- Continuity of horizontal and vertical displacements at every soil-soil interface
- Continuity of horizontal and vertical stress at every soil-soil interface
- No inward radiation at the infinitely far away boundaries of the halfspace

In total $2 + n_{soil} \cdot 4 + 2$ unknowns require the same amount of conditions to become a solvable system.

Source

Implementation of the external force is applied through the boundary conditions. The continuity of vertical stress at soil-water interface can be defined in the following form:

$$p_f(z_f = D_f) = -\sigma_z z(z_1 = 0) + \sigma_{z,ext}, \quad (2.43)$$

where $\sigma_{z,ext}$ is the vertical stress resembling the source function. The source is assumed to be a point source in space and therefore only dependent on frequency.

2.3.1 System of equations

The system of equations can be seen as a matrix vector multiplication:

$$\begin{bmatrix} M_{1,1} & M_{1,2} & \cdots & M_{1,i} \\ M_{2,1} & M_{2,2} & \cdots & M_{2,i} \\ \vdots & \vdots & \ddots & \vdots \\ M_{i,1} & M_{i,2} & \cdots & M_{i,i} \end{bmatrix} \cdot \begin{pmatrix} a_1 \\ b_1 \\ \vdots \\ d_i \end{pmatrix} = \begin{pmatrix} 0 \\ \sigma_{z,ext} \\ \vdots \\ 0. \end{pmatrix} \quad (2.44)$$

The solution to amplitude vector of system of equations can be found by:

$$\bar{A} = \bar{M}^{-1} \cdot \bar{F}, \quad (2.45)$$

A small amount of damping is applied to account for the singularity of matrix \bar{M} . Because of this singularity, the matrix is not invertible and therefore the set of equations can not be solved.

2.3.2 Damping

Damping affects the shape of the SRS significantly. It can be caused by several phenomena; energy conversion at layer boundaries (reflection and refractions), spatial or geometric damping and through material properties. The damping applied here is material damping. Two simple damping models are considered in this thesis, one viscous (frequency dependent) and one hysteretic model.

Kelvin-Voight model The damping that is applied in this model is visco-acoustic or visco-elastic. It is considered to be material damping hence only variant in time and not in space. The assumption is made is the lame parameters are considered to be linearly dependent on frequency in the frequency domain.

$$\lambda^* = \lambda_0 (1 + i\omega\varepsilon_\lambda), \quad (2.46)$$

$$\mu^* = \mu_0 (1 + i\omega\varepsilon_\mu). \quad (2.47)$$

Through this relation a complex representation of characteristic velocities can be found for the p-waves and s-waves:

$$c_s^* = c_s \sqrt{1 + i\omega\varepsilon_s}, \quad (2.48)$$

$$c_p^* = c_p \sqrt{1 + i\omega\varepsilon_p}. \quad (2.49)$$

The star denotes that the parameter is complex valued. In the above equations the small values of ε_λ , ε_μ , ε_p and ε_s are not necessarily the same values. The relation between them are defined as follows:

$$\varepsilon_\lambda = \frac{\lambda_0\varepsilon_p + 2\mu_0(\varepsilon_p - \varepsilon_s)}{\lambda_0}, \quad (2.50)$$

$$\varepsilon_\mu = \varepsilon_s. \quad (2.51)$$

Note that when ε_s and ε_p are the same ε_λ equals ε_p . The damping terms in the Kelvin-Voight mode are linearly dependent on frequency. However, Aki and Richards stated that for small frequencies found in seismic data this is not the case and damping can be considered effectively constant [1].

Hysteretic model The Kelvin-Voight model can be rewritten to account for frequency independent damping terms. A hysteretic damping model is the result. The following conditions are required to hold:

$$\varepsilon_{\lambda}\omega = 2D_{\lambda}, \quad (2.52)$$

$$\varepsilon_{\mu}\omega = 2D_{\mu}, \quad (2.53)$$

where D_{λ} and D_{μ} are the damping ratios of the bulk- and shear modulus, respectively. Similar as for the frequency dependent ratios, the damping ratios for shear waves and compressional waves (D_s and D_p , respectively) can be related to the damping ratios for bulk- and shear modulus:

$$D_{\lambda} = \frac{\lambda_0 D_p + 2\mu_0 (D_p - D_s)}{\lambda_0} \quad (2.54)$$

2.3.3 Dispersion- or surface response spectrum

The boundary conditions will result in a system of equations governing the response of the soil. The unknown amplitude vector can now be readily solved. Upon substitution of these amplitudes into the corresponding response function, the response e.g. velocities, pressure etc., at any given location can be represented as a function of frequency and wavenumber. To compare the calculated response to the measurements the pressure response at the soil-liquid interface shall be calculated.

Chapter 3

Inversion method and verification

In the inversion process we try to estimate a proper shear wave velocity from an initial Earth model. A genetic algorithm is used for the inversion process. The genetic algorithm is based on natural selection defined by diversity among populations living organisms. The cross correlation between the measured response, either synthetic for the ideal case or actual data, and modeled response is defined as the objective function and is maximized. First a small introduction is given to the idea of genetic inversion, then information regarding settings and the objective function are provided. Later on several inversion scenario's are provided where synthetic data is used as "measured" data, regarding inversion of the compressional wave velocity profile and the influence of receiver length.

3.1 Inversion problem

3.1.1 Suitability

The objective function that will be maximized is the cross correlation between measured and modeled surface response spectra and can be described according to:

$$suit = \frac{1}{n_f \cdot n_k} \sum_{k=1}^{n_k} \sum_{f=1}^{n_f} \frac{\left(P^{(meas)}(k, f) - \overline{P^{(meas)}}(f) \right) \cdot \left(P^{(mod)}(k, f) - \overline{P^{(mod)}}(f) \right)}{\sigma^{(meas)}(f) \cdot \sigma^{(mod)}(f) + \epsilon^2}, \quad (3.1)$$

where P is the vertical pressure of the modeled and measured surface response. The \bar{P} is the averaged pressure across the wavenumbers used. The standard deviation σ is defined as:

$$\sigma = \sqrt{\frac{1}{n_k} \sum_{k=1}^{n_k} (P(k, f) - \bar{P}(f))^2}. \quad (3.2)$$

The epsilon is a stabilization term that prevents division by zero and must be handled such that the effect of noise on the suitability is minimized. It is related to the maximum standard deviation of a reference spectrum chosen to be the starting model:

$$\epsilon = \varepsilon \cdot [\sigma_{ref}^{(mod)} \cdot \sigma_{ref}^{(meas)}]_{max}. \quad (3.3)$$

The value of ε lies typically between 1 % and 5 % [7]. The reference value is obtained from the predefined initial soil model and used throughout the inversion, this makes sure that within an inversion the stabilization factor does not change.

The pressure can be written as the multiplication of the transfer function from the source to pressure at the surface G_{PS} and the power spectrum of the source, S :

$$P(k, f, f) = G_{PS}(k, f) \cdot S(f). \quad (3.4)$$

Substitution of equation 3.4 into equation 3.1 yields an expression where the source terms falls out of the equation, provided that the stabilization factor is zero. Depending on the value of stabilization, the influence of the source terms will change. The effect of the source will diminish with decreasing value of the stabilization factor and lower energetic frequencies will have an increased influence on the suitability of the response. It is common that in typical source spectra the higher frequencies are less present. Part of the objective of this thesis is to invert for pressure waves and since pressure waves have more influence on the SRS at higher frequencies, a source independent objective function can be beneficial. Moreover, the source is in fact an unknown parameter in the measurement and can not easily be retrieved, resulting in another benefit of source independent objective function.

3.1.2 Inversion method

The inversion method used in this program is a global scheme. A local scheme is often used which requires accurate data on the background profile in order to find the global solution i.e. the starting solution must be close to the global solution to ensure convergence. However, the global scheme tries to mitigate the chance of ending up in a local minimum, by using a clever algorithm that tries many possible solutions.

Natural selection is the foundation of the genetic algorithm. It uses the diversity found in a population of living organisms to find solutions that can better adjust in that situation. In a biological community it is usually the case that the individuals that can best adjust to its surrounding environment will dominate the species. These individuals will more likely survive the hostile environment they live in and pass on their superior genes to the next generation and with time these genes will control the diversity of the population. If no genetic mutation would be present the population would converge to this “ideal” genetic package if enough time would pass. Mutation in the genes of individuals of upcoming generations allows certain individuals to find properties that can adjust even better in a certain situation. Although mutation usually is not beneficial, it does make sure that diversity keeps existing in the population. This is especially beneficial when the environment is always changing, as in nature. Diversity and mutation can also be beneficial to a problem that is highly non-linear i.e. multiple local minimums. This principle is combined with a randomized parallel search method and can be applied to a variety of complex problems.

The algorithm is built up from individuals that have their own genetic package. In the case of seismic data inversion these individuals can be any parameter that defines the wavefield. In this thesis, these parameters are shear wave velocity and compressional wave velocity, but parameters like density, layer thickness, or damping parameters can be incorporated as well. The profile of the velocity in depth is the string of genes that show diversity. A randomized search method is used to find the best fit solution. The suitability describes the fitness of every individual within a population that has been randomly generated. Starting from an initial population, the fitness or suitability defines the chances of certain individuals to pass on their genes (i.e. velocity profile) to the next generation. In appendix D a detailed overview is provided of the genetic inversion program as developed by de Winter [6]. An adaption to this program is made to include the inversion of compressional wave velocity profile.

3.2 Results of pressure wave velocity inversion

The program was initially intended to invert for the SRS of velocities, the initial p-wave inversion program therefore also inverted for velocities in stead of the pressure at the surface. Bear in mind that the results covered in this section are still related to velocities. All other sections use the surface response of pressure.

Initially the inversion of p-wave velocity was done using the full SRS up to 120 Hz, body wave related events as well as surface waves were taken into account for the inversion. Figure 3.1 shows the results of a p-wave inversion for frequencies up to 120 Hz. In this case only the pressure wave is the unknown and the shear wave velocity profile is known. The results show that only the first layer is estimated properly and the other layers are not. A pulse load is used during this inversion. The initial soil model has 4 layers overlaying a halfspace. The initial soil model is displayed in table 3.1.

Table 3.1: Background profiles for density, layer thickness and s-wave velocity.

	Thickness	Density	c_s
layer i	m	kg/m^3	m/s
1	4	1000	0
2	6	1500	140
3	10	1600	150
4	5	1700	160
5	5	1500	140
Halfspace	∞	180	

The proper estimation of the first layer is probably caused by the fact that dispersion curves of the fundamental mode and the higher modes are highly influenced by the shear wave speed and the p-wave speed of the upper layer. The p-wave velocities of the lower layers only influence the dispersion of surface waves to a small extent. In addition, the acoustic guided modes at these frequencies do not contribute to the fitness enough to overcome the high influence of surface waves. The separation of guided modes and an increase of the frequency range was introduced that could lead to a better prediction of the pressure wave profile.

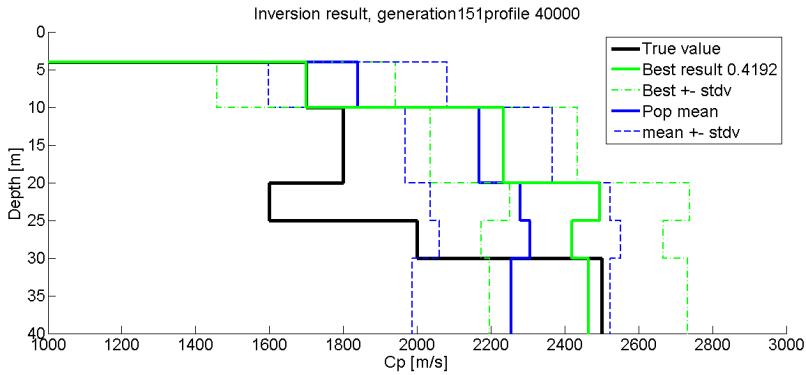


Figure 3.1: “Inversion crime” estimation of C_p , no convolution, frequencies up to 120 Hz, wavenumber up to 0.5 m^{-1} with the response based on the impulse function.

As a second attempt a window of the SRS was taken to separate the body wave related events from the surface waves. The frequencies and wavenumbers used ranged between $\pm 120 \text{ Hz}$ to $\pm 250 \text{ Hz}$ and 0 to 0.25 m^{-1} , respectively. This inversion showed better results, as can be seen in figure 3.2. The cut off at 0.25 m^{-1} is done to take away the major influence on the suitability of the fundamental mode and its higher modes, figure 3.3. The SRS shows the interference patterns of body waves in this range, figure 3.4. It is clearly visible that the dominance of the fundamental mode must be either diminished or not taken into account for inversion of the p-wave velocities.

3.3 Impact of finite length measurements

3.3.1 Truncation in space and time

The effect of receiver length can be interpreted by a multiplication in xt domain of the shot record with a boxcar function or as a convolution in fk domain with the sinc function (or a windowed version as is generally the case). Proper convolution requires the presence of all modes, therefore the stepsize in wavenumber should be sufficiently small. From de Winter [6] it became clear that the peak width of the modes are generally 0.001 m^{-1} and a stepsize of 0.00024 m^{-1} is recommended to capture all the characteristic modes. For P wave guided modes the peaks could be smaller and a smaller stepsize could be beneficial.

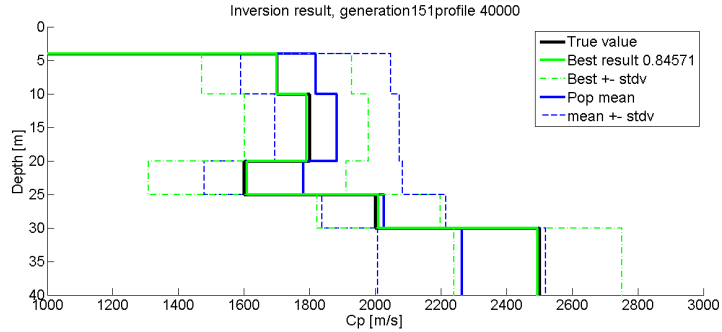


Figure 3.2: “Inversion crime” estimation of C_p , no convolution, frequencies ranging from 120 Hz to 250 Hz, wavenumber up to 0.25 m^{-1} with the response based on the impulse function.

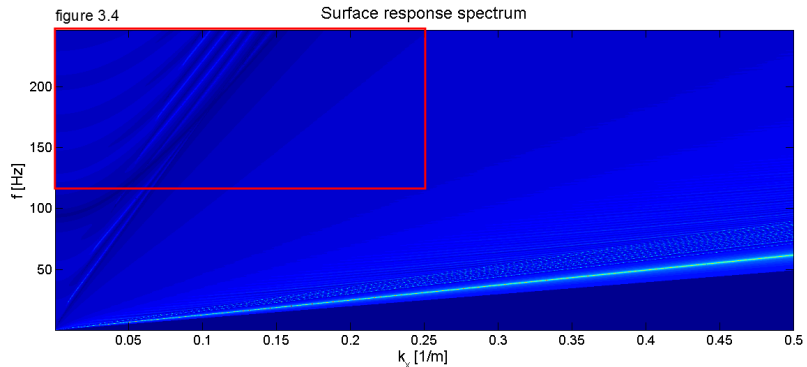


Figure 3.3: Actual SRS of the pressure wave interference pattern at frequencies up to 250 Hz of the impulse response. The figure shows the spectrum to power 1/3 in order to make the smaller peaks visible i.e. $V_z^{0.3}$.

Truncation of the response is performed through a Fast Fourier Transform algorithm or a convolution algorithm. The FFT truncation transforms the SRS from fk to xt , truncates the response in space and time and transforms it back to the fk domain. The convolution algorithm uses the convolution theorem to directly take into account the truncation, it must be noted that only truncation in space is applied not in time. The assumption is made that larger restrictions are put on the receiver length than on measurement time, which is generally the case.

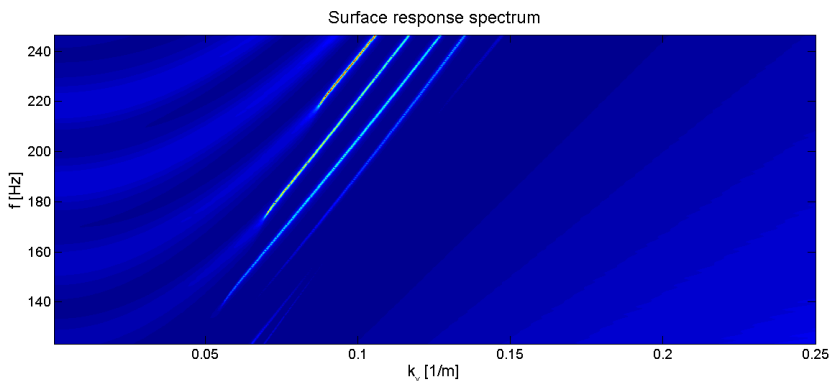


Figure 3.4: SRS used to estimate the p-wave velocity profile. Frequencies between 120Hz and 250Hz and wavenumbers up to 0.25m^{-1} are used in the inversion. Notice that no influence of the surface waves was considered, hence also no scaling is applied to make these peaks visible.

Due to the nature of the Fourier transform the signal is considered periodic in space and time; the signal will therefore wrap around in the space time domain, as can be seen in figure 3.5. The stepsize in f and k should be sufficiently small to take this in to account, since dk and df are inversely related to the maximum offset and time duration. This puts restrictions on higher frequencies if these need to be taken into account i.e. smaller stepsize with larger frequency range means more steps. No limitations are set on the convolution algorithm with respect to stepsize in k , which is an advantage of the convolution algorithm.

Convolution

The convolution routine is represented as follows and is performed for every frequency:

$$w(k) = \sum_j u(j) s(k - j + 1). \quad (3.5)$$

In this equation s is the sinc window, u is the initial SRS and w is the convolved version of the SRS. The length of w becomes $m + n - 1$, when considering the length of u equal to m and the length of s equal to n . The parameters k and j are the wavenumbers of the initial SRS and j is a pseudo-wavenumber which will form the new wavenumber set.

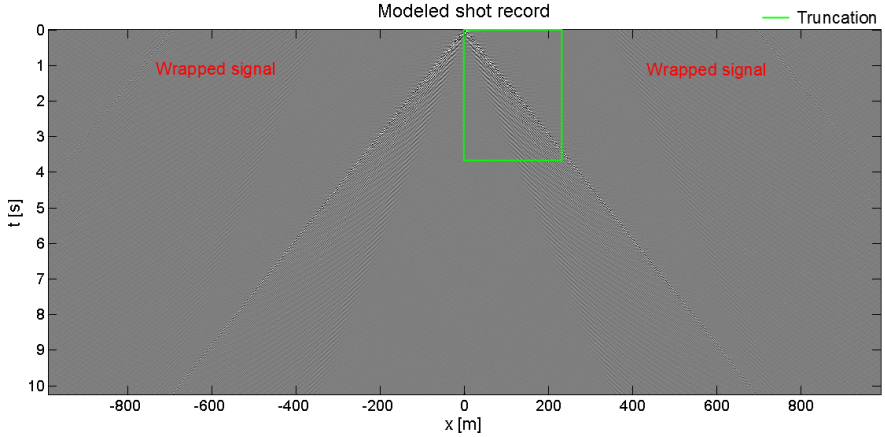


Figure 3.5: A modeled response of a shot record for a slightly damped soil model. The wrapped signal is shown and should be sufficiently far away from the area of interest, represented by the green square.

FFT truncation

The truncation in space and time requires the transformation from frequency to time and from wavenumber to space and their inverse transforms. The numerical Fourier transforms are provided in appendix B. The real Fourier transform can be used to transform the data from frequency to time, it relies on the fact that the surface response in the space time domain is real valued. This suggests that across frequency the spectrum corresponding to negative frequencies should be the complex conjugate of the spectrum corresponding to the positive frequencies. This reduces the required calculations needed for the transformation. However, across wavenumber this is not the case and the more generally formulated complex Fourier transform is required. Due to symmetry of the model (horizontally stratified soil) the pressure is symmetric across wavenumbers; therefore, only the spectrum for positive frequencies and wavenumbers is required to describe the xt domain. This is however not the case when lateral variations are considered. For more detail on complex and real Fourier transform a reference is made to appendix B and [21]. The process of truncation is schematically represented in figure 3.6.

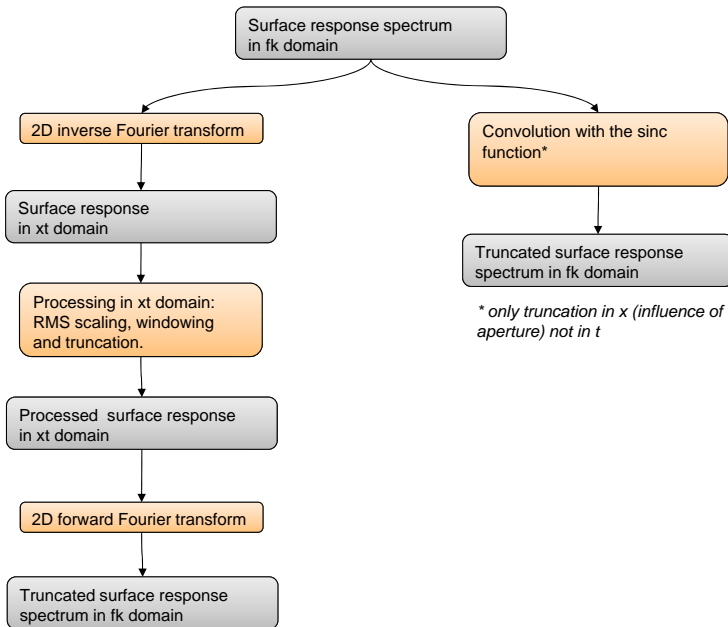


Figure 3.6: Schematic overview of the FFT process.

Choice of truncation method

The FFT routine was preferred over the convolution routine due to the following reasons:

- calculation time
- no possibility of xt domain related processing e.g. scaling (also applied to the measurements)

Convolution routines are slow with respect to FFT routines and become rapidly slower when the window size increases. The window size of the convolution window is related to the width of the main lobe and the attenuation of the sidelobes of the sinc function [21]. Although the sinc function, especially when windowed, can

provide a relatively short window, the fact that no processing of the data can be performed in the xt domain rules out the use of the convolution routine. The processes performed in the xt domain are schematically represented in figures 3.7 and 3.8.

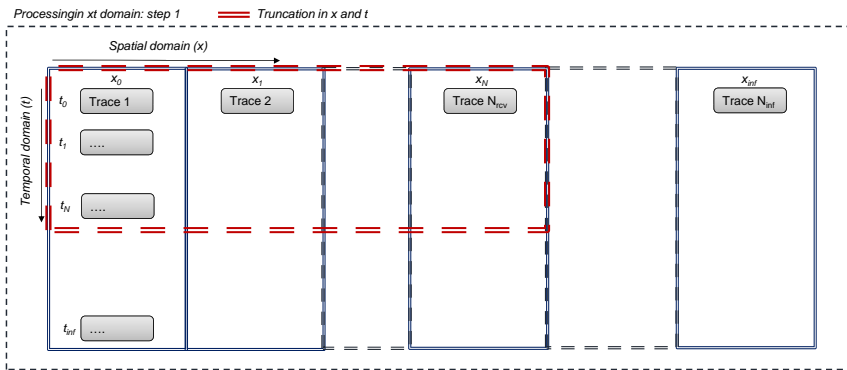


Figure 3.7: Schematic overview of the processing in xt domain: step 1 truncation of measurement in xt domain to include the influence of aperture and measurement time.

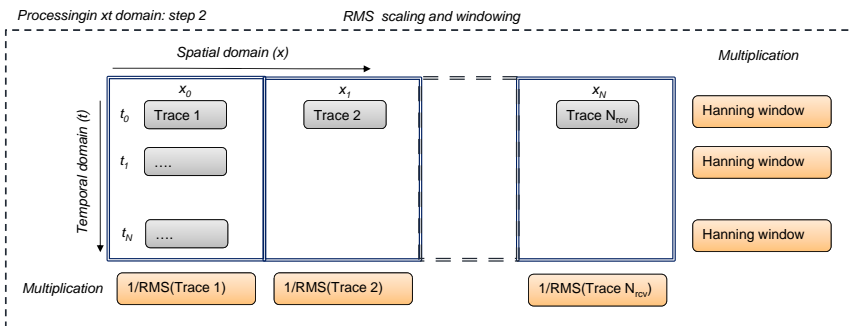


Figure 3.8: Schematic overview of the processing in xt domain: step 2 RMS scaling applied to each trace and windowing applied to each timestep.

3.3.2 Shear wave velocity

The effect of truncation can best be represented through slices of the dispersion spectrum. Several slices at frequency 16 Hz, 32 Hz and 48 Hz are presented in figure 3.9. The spectra that are visible correspond to a response that is not truncated and for one that is truncated at 240 m in space and 4 s in time. The plots show the spectral leakage caused by truncation in x domain, in addition the effect of sidelobing is shown.

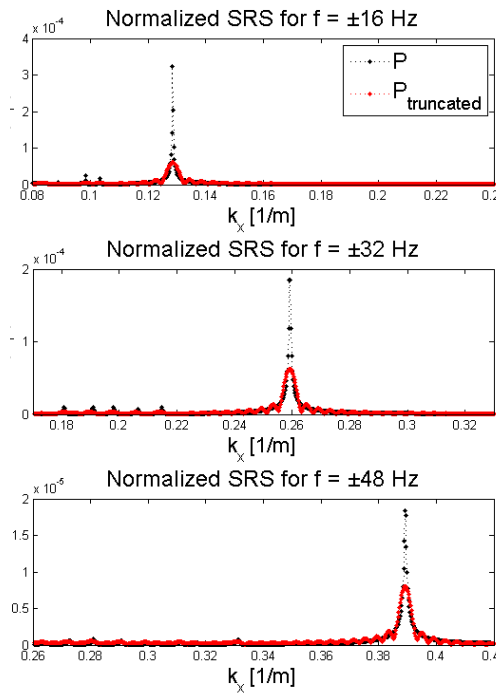


Figure 3.9: Frequency slices of the spectrum at 16 Hz, 32 Hz and 48 Hz. The black figure shows the untruncated result and the red figure shows the result of the truncated measurement of 240m in space and 4s in time.

The shear wave velocity profile is inverted without truncation and with truncation of a 240 m receiver. The model used consists of 4 layers and it is assumed that background profiles regarding density, layer thickness and p-wave velocity are known. The background profiles are displayed in table 3.2. The source used is a Ricker wavelet with a central frequency of 20 Hz. The damping ratios used for the inversion are equal for both shear wave velocity and compressional wave velocity and considered to have a value of $D_p = D_s = 1e - 3$. The settings of the forward model and inversion program are presented in tables 3.3 and 3.4.

Table 3.2: Background profiles for density, layer thickness and p-wave velocity.

	Thickness	Density	c_p
layer i	m	kg/m^3	m/s
1	4	1000	1500
2	6	1500	1700
3	10	1600	1800
4	5	1700	1600
5	5	1500	2100
Halfspace	∞	2500	

Table 3.3: Settings for forward model of inversion.

Settings	df/dt	f_{max}/T	dk/dx	k_{max}/X	n_t	n_x
	Hz/s	Hz/s	m^{-1}/m	m^{-1}/m	-	-
Forward model	0.125/7.828-3	63.875/4	2.44e-4/1	0.5/240	1024	4096

Table 3.4: Settings for forward model of inversion.

Settings	Gen.	Pop.	$\#_{conts}$	P_{mut}	$\#_{dads}$	$c_{s,range}$
	-	-	-	-	-	m/s
Genetic algorithm	100	90	35	0.25	30	100-300

The results of the inversion of c_s was performed allowing the profile to range between 100 and 300 m/s. The inversion is done using synthetic data, to be more precise the “inversion crime” is performed meaning that the measured response is obtained through the same forward calculation as the modeled response. The result for the truncated signal is represented in figure 3.10. This figure shows the result found with the best fit.

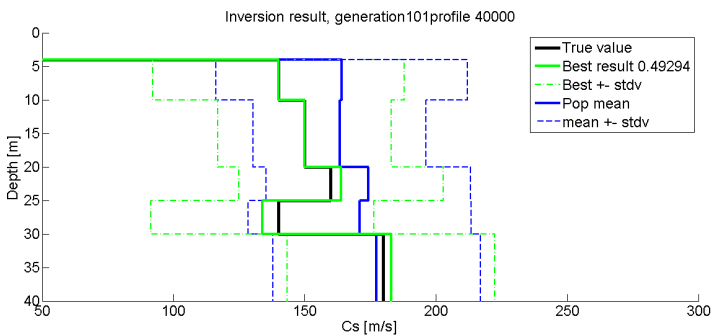


Figure 3.10: “Inversion crime” estimation of c_s inverted for the spectrum of a 240 m receiver, and measured for 4s in time.

The convergence is monitored through the diversity of the generation. A measure of the diversity of a population is given by its standard deviation. In figure 3.11 the standard deviation per layer and the sum across all layers is given per generation. Due to mutation the standard deviation will never reach zero, but will stagnate when enough generations have been produced.

3.3.3 Compressional wave velocity

A similar inversion is done for p-wave velocity profile. For this inversion the influence of the surface waves is neglected by an fk filter. The fk filter filters all phase velocities higher than the highest shear wave velocity in the actual shear wave profile. Now all events related to body waves are present in the part of the spectrum considered. The source used is a Ricker wavelet with central frequency of 90 Hz. The high frequency for the convolution posed restrictions on the time scale. The timestep is inversely related to the maximum frequency calculated, therefore only truncation in space was applied. In table 3.5 the background profiles are presented.

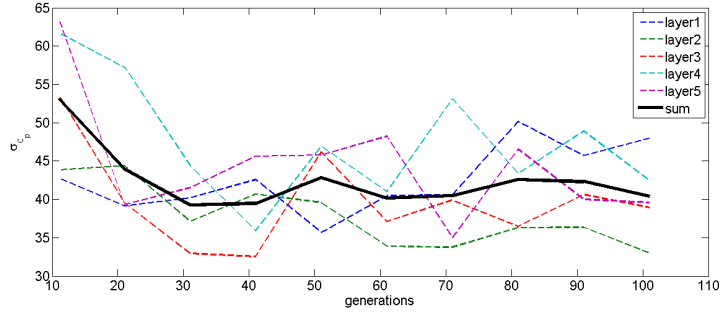


Figure 3.11: Course of standard deviation per layer and the sum across all layers with number of generations.

In tables 3.6 and 3.7 general settings for the forward model and inversion routine. The resulting best fit p-wave velocity profile is shown in figure 3.12. Even without visible convergence within 60 generations (figure 3.13), a proper velocity profile is found.

Table 3.5: Background profiles for density, layer thickness and s-wave velocity.

	Thickness	Density	c_s
layer i	m	kg/m^3	m/s
1	4	1000	0
2	6	1500	140
3	10	1600	150
4	5	1700	160
5	5	1500	140
Halfspace	inf	180	

Table 3.6: Settings for forward model of inversion truncated p-wave velocity inversion.

Settings	df/dt	f_{max}/T	dk/dx	k_{max}/X	n_t	n_x
	Hz/s	Hz/s	m^{-1}/m	m^{-1}/m	-	-
Forward model	0.125/7.828-3	255.875/4	2.44e-4/1	0.5/240	2048	4096

Table 3.7: Settings for forward model of inversion for truncated p-wave velocity inversion.

Settings	Gen.	Pop.	#conts	P_{mut}	#dads	$c_{p,range}$ m/s
Genetic algorithm	60	90	35	0.25	30	1500-2500

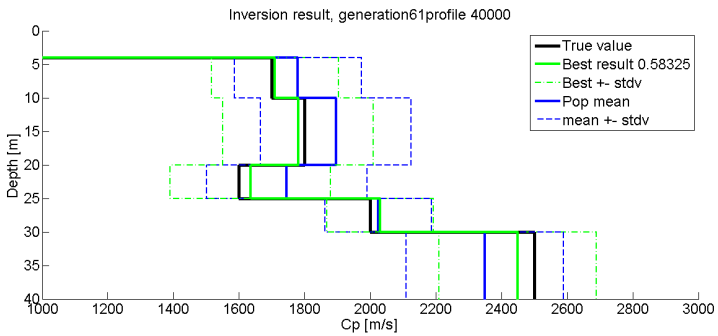


Figure 3.12: “Inversion crime” estimation of C_p inverted for the spectrum of a 240 m receiver, and measured for 4sin time.

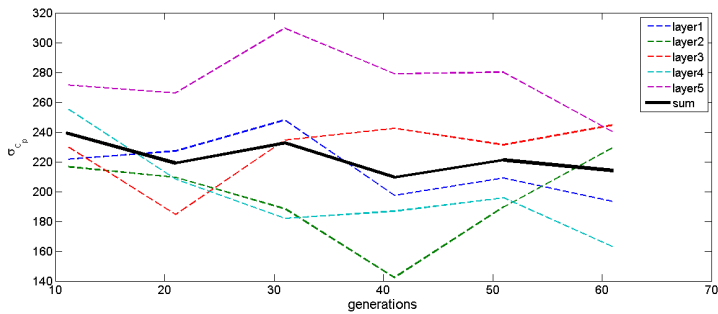


Figure 3.13: Course of standard deviation per layer and the sum across all layers with number of generations

3.4 Summary and conclusions

The cross-correlation between modeled and measured data is used to establish the fit of a solution. The cross-correlation is source independent and its use could be beneficial since often no or little knowledge is available regarding the source function. A stabilization factor based on the pre-defined initial model is introduced to avoid division by zero and to decrease the influence of noise.

The inversion process consisted of a genetic algorithm that is based on natural selection. A solution is found by using the diversity of a certain population to generate a new population that best fits the inversion problem. With enough generations the global solution is found. Mutation is introduced to mitigate the possibility of ending up in a local minimum.

The inversion algorithm is developed by de Winter [6] and is adapted for the inversion of p-wave velocity profile in this thesis. For the inversion of p-wave velocity it was found that guided modes and other body wave related events visible in the upper left quadrant of the SRS could be used in the ideal case using a synthetic measurement for a 4 layered model. However, the influence of surface waves should be neglected and higher frequency content is required for a proper inversion of compressional wave velocity.

The influence of receiver length and measurement time were presented by considering either a convolution algorithm or a FFT based process of truncation. The FFT based truncation was preferred since convolution is a slow when large windows are required. More importantly no space time domain process like scaling can be applied, which also need to be performed on the measurement data. A truncated signal allowed the inversion of a proper p-wave and s-wave velocity profile for a 4 layered model.

Chapter 4

Near-surface geophysical measurements in practice

As discussed in section 2.1 the propagation of waves through soil is dependent on the properties of the soil. The so called modes of propagation are defined by parameters such as layer thickness, density, bulk-, shear modulus, and Poisson's ratio. Background profiles regarding density and layer thickness can be obtained from cone penetration tests (CPTs) and borehole measurements and are therefore not part of the inverted parameters. When the subject of interest is the estimation of the remaining soil parameters, it is of vital importance that the characteristic modes are visible and distinguishable in the measurements. Seismic data is usually measured in the space-time domain as a discrete representation of the surface response and subsequently transformed to the fk domain. This chapter will elaborate on the acquisition of the surface response and the spectral analysis of the wavefield. The discrete- and finite sampling of the acquired data puts limitations on the usability of the data and will be discussed as well.

4.1 Data acquisition in space-time domain

Data acquisition is the principle step in seismic processing. It involves the experimental measurement of wave propagation in a soil of interest. Seismic waves traveling through a soil medium will generate vibrations of soil particles. The associated response can be captured by sensors for a given location in space. Usually, the response is expressed in velocities, accelerations or pressure due to their simplicity to be measured with respect to displacements. A time signal of a single receiver is called a seismic *trace* and is the elementary unit of seismic data. When the receivers are placed in a series along the surface, seismic data can be seen as a two dimensional

function of distance from the source (offset) and of time. The process of recording a series of receivers is referred to as multi-channel recording and results in the surface response called the shot record.

4.1.1 Measurement set-up

Measurements were performed in the IJsselmeer in the Netherlands. The IJsselmeer is a fresh water lake. The measurements are part of the joint research project between Siemens Windpower, Delft University of Technology, and Fugro Geoservices, referred to as DISSTINCT [26]. It is comprised of the measurement of locations W27 and W28 using hydrophone type receivers.

In an early stage of the project two measurement options were proposed:

1. The first option was Fugro's newly developed Gamba's system: A semi-stationary measurement set-up where a streamer of hydrophones is pulled behind a vessel. The streamer lies still on the seabed and one or multiple shots are performed. Once these shots are performed the streamer is pulled forward and the procedure is repeated. The shots could be performed every 15m.
2. The second option was a stationary measurement set-up where a streamer consisting of multiple receivers is placed on the seabed and the shots could be performed from various locations as many times as required to optimize the signal to noise ratio.

The shots were proposed to be shots at the end of or at a distance from the streamer i.e. end-off shots. In the end, option 2 was deemed to be most suitable since it allowed a more detailed measurement locally. In addition, the possibility to perform measurement with large offsets was preferred with respect to measurements of pressure wave related events. The drawback was that only a streamer array of 48 channels was available. The proposed solution was to concatenate two streamer locations per shot. This meant that one shot would be performed at a certain location, then the receiver would be relocated and another shot at the same location would be performed. The concatenation of these two separate data sets would resemble a single dataset with an effective length of twice the streamer length.

Two different measurement set-ups were proposed:

1. 2 x 48 channel streamer with end-off shot + relocation of source for double offset
2. 2 x 48 channel streamer with end-off shot + relocation of both source and streamer for double offset

Set-up 1: The first set-up was proposed by Fugro. The process of concatenating two datasets was extended to incorporate even more offset. For every shot location the source would be relocated, when all shots were performed the streamer would be relocated and the procedure was repeated. A maximum offset of 180 m is reached, see figure 4.3. It was assumed that the center of the double receiver array was located at the windturbine location. A two receiver overlap was proposed to help concatenate the datasets. A graphical representation of the procedure and measurement set-up is given in figure 4.1.

Set-up 2: The second set-up was proposed by Siemens and Delft University of Technology. This set-up was similar to the one proposed by Fugro except that in this set-up both source and streamer would be relocated. The location of interest is considered to be centered between source and the end of the streamer. A graphical representation of the procedure and measurement set-up is given in figure 4.2.

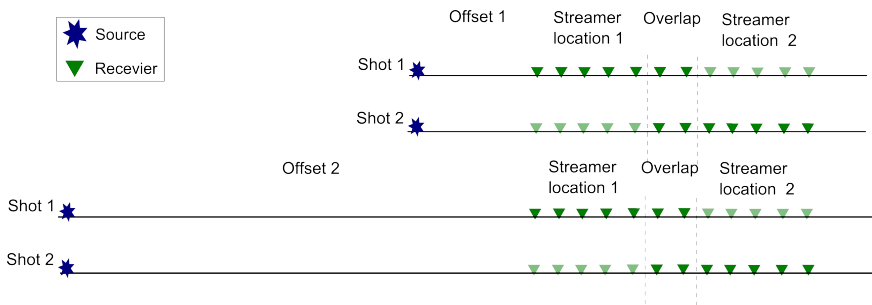


Figure 4.1: The measurement set-up proposed by Fugro Geoservices (set-up 1). The streamer is placed at a certain location and the shot is relocated to increase offset. The location of interest is assumed to be in the middle of the streamer where the two streamer overlap.

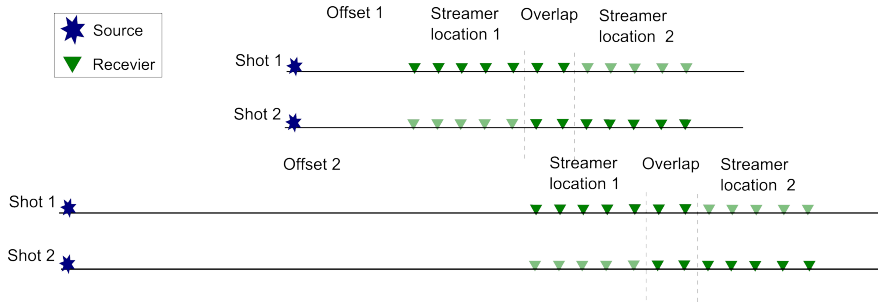


Figure 4.2: The measurement set-up proposed by Delft University of Technology (set-up 2). Both streamer and source are relocated to increase the offset. The location of interest is assumed to be centered between end of streamer and source.

The first set-up was chosen after a trade-off. The major drawback of the preferable option (set-up 2) was that the streamer would need to be relocated too often. For every relocation of the streamer the “straightness” of the array needs to be evaluated by aligning the direct pressure wave arrival. This procedure required the deployment of the streamer, performing a shot and checking whether the first arrival is a straight line and therefore the receivers would be in line. This process would need to be repeated until a satisfactory “straightness” is reached and, thereby would cost a lot of precious measurement time and inaccuracies regarding the alignment and concatenation of the arrays would build up with every relocation.

Performed measurements

Several practical issues made the performance of the initial proposed measurements not viable and decisions needed to be made with respect to the extent of the measurements. The deployment of the streamer turned out to be more difficult than anticipated. The following issues made the initial measurement set-up impossible:

- weather conditions caused major downtime
- equipment breakdown caused major downtime
- inappropriate survey boat
- low accuracy in positioning system

The measurements were performed from two vessels, named the Zeus and the Poseidon. The vessel with the array was placed in position and anchored up wind to prevent major displacements of the boat. The other vessel picked up the receiver and pulled it in position. Eventually the measurements involved the deployment of a 48 channel receiver array and a mini-airgun. Several offsets were performed to catch the near-field and the far-field of the wave-propagation through the soil.

The 48 receivers were spaced 1 m apart resulting in a single receiver length of 47 m. The shots performed were end-off shots, meaning that the shots were performed at the end of the streamers not on top of the streamer. A spacing of 45 m in between shots was applied until a total effective receiver length of 227m was reached. This would allow the concatenation of multiple shots into a “super shot” to increase spatial resolution, discussed in detail in section 4.1.4. An overview of the shots performed are given in figure 4.3.

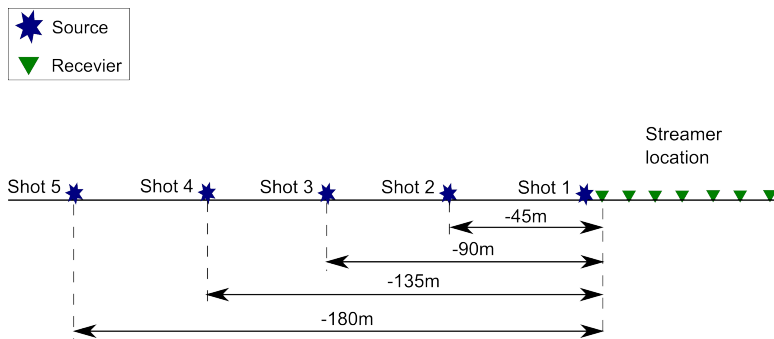


Figure 4.3: An overview of shots proposed, the eventual set-up is shown as a single streamer array. This set-up allowed a max. offset of 227 m (180 m offset + 47 m streamer).

Several remarks need to be made regarding the accuracy of the measurements. The low accuracy of the GPS system made the concatenation of the several datasets unreliable. Additionally, during the measurements of the W27 turbine location the data was misaligned with the line of shots. This required the correction of the effective receiver spacing with an angle of approximately 15 degrees to acquire a similar one dimensional shot record, see figure 4.4.

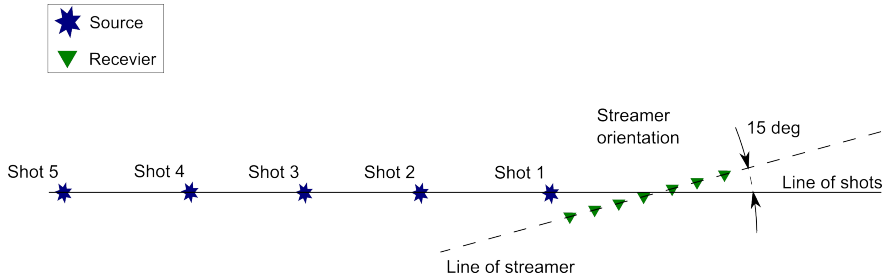


Figure 4.4: Topview of measurement performed at turbine location W27, a representation is given regarding the misalignment of the shot line w.r.t. the streamer line.

Receivers

In this section technical details of the measurement equipment is given. For detailed overview of the measurements a reference is made to the geotechnical report provided by Fugro Geoservices [23]. As mentioned before a string of 48 hydrophone receivers was used, in total a receiver length of 47 m was reached. Five subsequent shots were performed, see figure 4.3.

Hydrophones

Hydrophones measure differential pressures in the water along the surface. The specifications of the hydrophones used are summarized in table 4.1.

Table 4.1: Hydrophone streamer data.

Hydrophone streamer	
Type	Hydrophones HC 2000
Cut off frequency, f_c	4.5 Hz
Length	47 m
Traces	48
Trace spacing	1 m

Source

The shot performed was extensively tested on the first day of measurements. The results of these tests showed that for the specific site considered, the energy and frequency content of the Ggun 60 cu inch showed best performance. The performance of a typical source is defined mainly by attenuation and site response, both site specific characteristics. The theoretical limit of the a airgun source is 3500 Hz. This would allow higher acoustic modes to be visible in the f_k spectrum. Figure 4.5 represents the 1D Fourier spectrum of the first trace of the data and shows that for this site the source shows energy content with frequencies up to 200 Hz. However the highest peaks are located in the first 35 Hz.

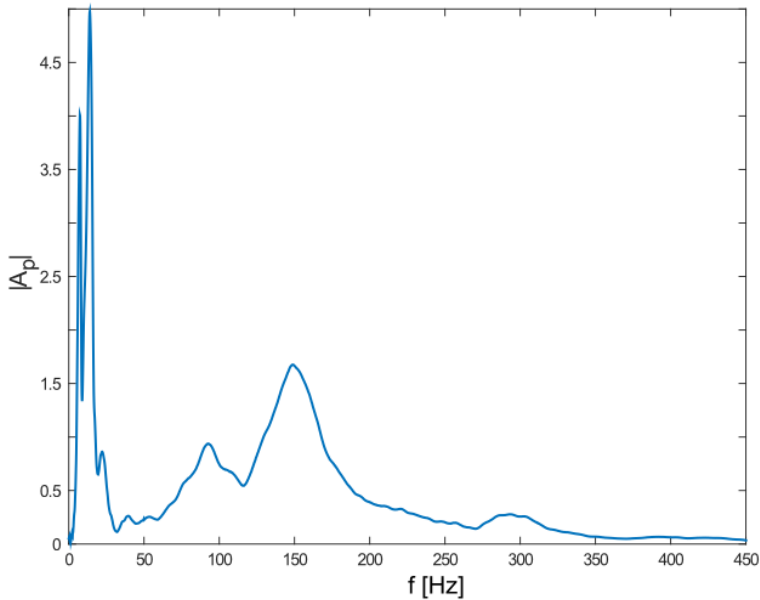


Figure 4.5: Fourier transform of the first trace showing frequency and energy content of the airgun source.

The source characteristics are displayed in table 4.2.

Table 4.2: Source specifications.

Source	
Source type	G-gun
Chamber size	60 cu inch
Pressure	100 bar

4.1.2 Locations and background profiles

The location of the shots performed correspond to locations W27 and W28. An overview of the Westermeerwind windpark and the measured locations is provided in figure 4.6.

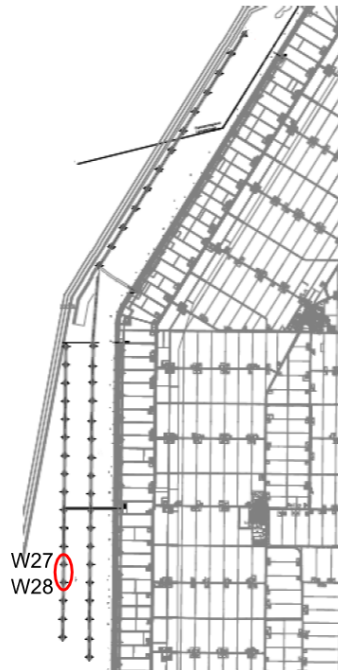


Figure 4.6: A schematic representation of the windfarm and the measured locations (W27 and W28).

The background data of layer thickness and layer density is obtained from CPT measurements performed at the site [13]. The resulted borehole tests resulted in a soil model of 8 layers. The halfspace was implemented at the location of a thick and medium dense to dense sand layer (layer 11 in table 4.3) located at 20 m below seabed (BSB). The very small peat layer (layer 10) located just above the thick dense sand layer (layer 11) is assumed to have a negligible contribution to the surface response spectrum (SRS) and will not be part of the inversion. The soil consists mainly of thicker dense sand layers alternated with thin clay and peat layers.

Table 4.3: Background profiles for density and layer thickness for turbine location W27.

layer i	Thickness m	Density kg/m^3	Soil type
1	4.4	1000	Fresh water, 11 °C
2	2	1900	Sand, very loose to loose, clayey
3	0.6	1500	Clay, soft
4	0.7	1000	Peat
5	5.3	2000	Sand dense
6	1	2000	Sand, medium dense, with clay lamination
7	6.5	2000	Sand, dense
8	3.3	2000	Sand, medium dense
9	1	1800	Clay, very silty, stiff
10	0.2	1100	Peat/Clay, very silty
11	10	2000	Sand, medium dense to dense

4.1.3 Post processing

A short summary is given of the pre-processing of the data as performed by Fugro Geoservices. The following procedures have been performed:

1. Check raw data quality in order to select the most proper datasets for the estimation process
2. Stack all the shots performed at every location using a cross-correlation algorithm
3. Correction of the delay time on all shots; difference between moment of shot and computer recording ($dt = 23.63$ ms)

Stacking of data is generally used to increase S/N ratio, in case multiple shots were performed at the same location.

4.1.4 Concatenation of multiple offsets

The datasets of the shot locations per site can be used to resemble a single longer dataset by placing them in subsequent order. This is called concatenation of the datasets. The concatenation of the several datasets is challenging, since the exact location of the shots was not exactly known. Any discontinuity in the measurement will cause distortion of the signal in the fk domain, therefore it is of importance to find the proper locations.

The separate shot records are concatenated by assuming that the first arrival in the shot record is the direct arrival of the pressure wave through the water. The Lubbers en Graaff's simplified equation [14] results in a speed of sound of fresh water at 11 deg C of:

$$c = 1405.03 + 4.624T - 0.0383T^2 \approx 1450ms^{-1} \quad (4.1)$$

As mentioned before the shot line and the streamer line were misaligned approximately 15 degrees for the W27 windturbine location, see figure 4.4. A transformation is made such that a equivalent 1D measurement is the result. This results in an effective receiver spacing of $dx \cos(\alpha) = 1 \cos(15) = 0.97$ m. The found offsets are summarized in table 4.4.

Table 4.4: Effective offset obtained after aligning the direct arrival.

Turbine location	Shot 1	Shot 2	Shot 3	Shot 4	Shot 5
	m	m	m	m	m
W27	-15.5	-59.6	-89.5	-142.5	-192

4.1.5 Reconstruction of concatenated datasets

The concatenated datasets did not fully cover the full offset range, due to the lack of knowledge regarding the shot positions. As mentioned in section 4.1.4 the separate datasets were concatenated by aligning the direct arrival with the speed of sound in water. The result of this process is shown in figure 4.7a: some missing signals and several bad traces. The traces were removed by setting the response of these traces manually to zero, see figure 4.7b.

Next a data reconstruction algorithm was applied based on the work of Trad [24]. The data reconstruction is based on a mixed linear and parabolic Radon transform of the input data. The linear Radon domain consists of bandlimited spikes for each linear event in the input data, the parabolic Radon domain with one bandlimited spike for each parabolic event. It is similar to the fk transform where each spike in the fk domain represents a monochromatic plane wave.

The algorithm will create a new dataset by inversion that:

1. will fit the measured data at the non-zero trace locations
2. consists of a summation of linear events and parabolic events (with the apex at zero offset).
3. will have the smallest L1 norm in the combined linear and parabolic Radon domain.

Actually, it solves an inversion problem that will describe the measured data with the least possible number of linear and parabolic events. Once these linear and parabolic events are matched at the measured locations they also have values at the location where there was no measurements and, thus, carries out interpolation.

In addition, at the measured locations we adopt the reconstructed signals such that noise was pushed out of the data as well, as noise cannot be described by a limited number of linear/parabolic events. The result of the sparse Radon reconstruction is shown in figure 4.7c.

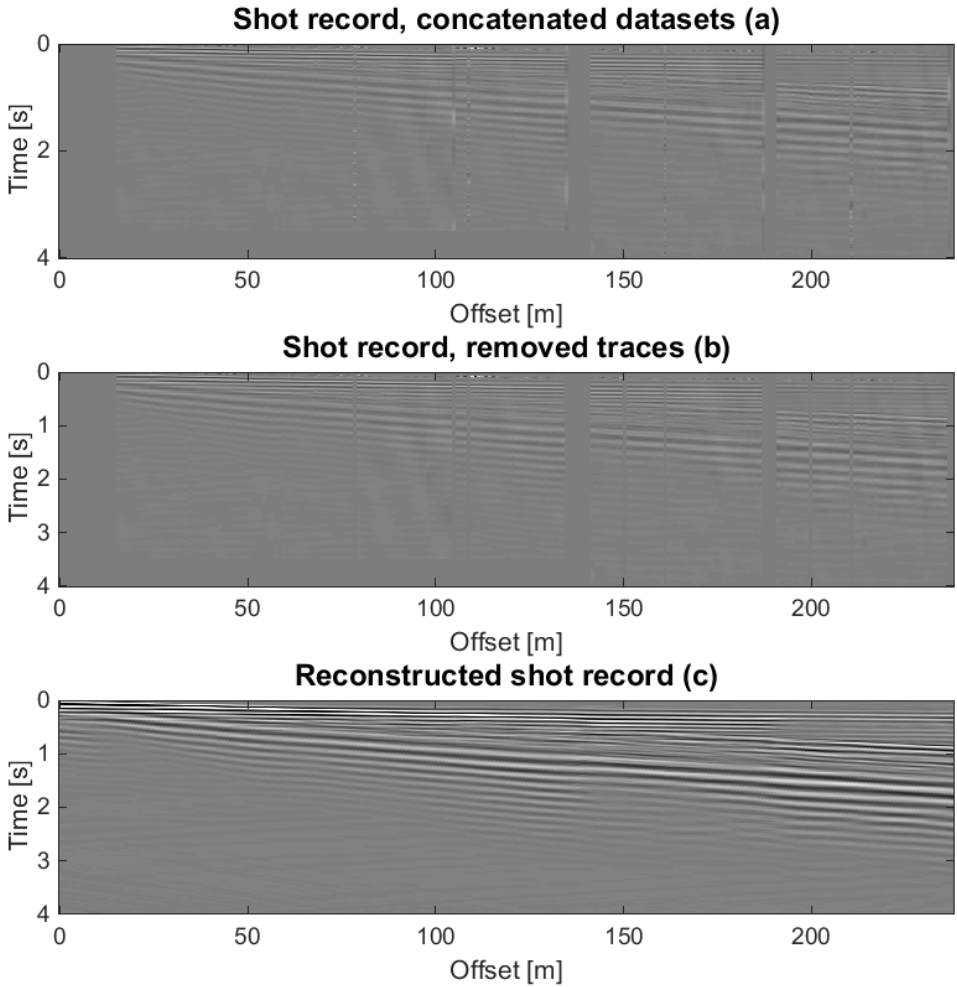


Figure 4.7: Process of reconstruction of the shot record: a) Concatenated datasets; b) Shot record with removed bad traces; c) Reconstructed dataset.

4.2 Spectral analysis

4.2.1 2D Fourier domain

The Fourier transform is the process of decomposing an arbitrary periodic signal into harmonic wave components, each with its own frequency-wavenumber combination, amplitude and phase. The theory in the following section was based on the book “Surface wave methods for near-surface site characterization” by Foti et. al. [10]. A detailed explanation of the theory used in this section is available in this book.

4.2.2 Restrictions and limitations

Wave propagation is recorded with a fixed time sampling and finite length. A finite number of receivers is deployed, which implies a discrete spatial sampling and maximum length of the array.

Acquisition of measurements is a matter of properly sampling the surface response. Sampling is done properly when the initial signal can be uniquely reconstructed from the samples taken. This results in the Shannen-Nyquist sampling theorem, which states that a signal is properly sampled when the sampling frequency/wavenumber is twice the highest frequency/wavenumber of interest in the analysis. The finite nature of the sampling process is the same as windowing with a *boxcar* function.

The same principles hold for sampling in time. The limitations on temporal sampling are on the other hand less severe, since the sampling can be done at a high enough frequency to capture the highest expected frequency and the time duration can be required easily to achieve proper temporal resolution.

4.2.3 Limits to wavenumber and frequency

The maximum resolvable wavenumber is determined by the receiver spacing. This wavenumber is usually called the Nyquist wavenumber and is described by the following equation.

$$k_{max} = k_{Nyquist} = \frac{1}{\lambda_{min}} = \frac{1}{2\Delta x}, \quad (4.2)$$

where λ_{min} is the smallest recoverable wavelength and Δx is the effective receiver spacing.

And similarly for frequency:

$$f_{max} = f_{Nyquist} = \frac{1}{T_{min}} = \frac{1}{2\Delta t}, \quad (4.3)$$

with T_{min} smallest recoverable period and Δt is the timestep used in the measurements.

Above the Nyquist wavenumber/frequency events present in the wavefield will be reconstructed as a shifted wavenumber with a wavenumber of $k_{alias} = k_{true} - 2k_{Nyquist}$, this phenomena is called aliasing. The range of waves that can be properly described is finite and ranges from $-k_{Nyquist}$ to $+k_{Nyquist}$. The receiver spacing of 0.97m defined in the measurement will allow for a maximum wavenumber of $k_{max} = \frac{1}{2\Delta x} = \frac{1}{2 \cdot 0.97} \approx 0.52 \text{ m}^{-1}$.

4.2.4 Streamer length or aperture

The length of the streamer or the aperture is the dominating factor for the spectral resolution of the measurements. A measurement can be seen as a finite representation of an infinite solution of the wavefield. This is in principle a multiplication of the full wavefield with a finite boxcar function in the space-time domain.

To clarify the next section it is best to recall a basic property of the Fourier transform. The most meaningful in the case of spectral resolution is the convolution theorem, which states that the convolution between two signals in a domain equals multiplication in the transformed domain. For our purpose the explanation is given in spatial frame of reference. For example if two functions in the space domain are multiplied, its Fourier transform will be the convolution of the functions in the wavenumber domain and vice versa;

$$g(x) \rightarrow G(k), h(x) \rightarrow H(k) \quad , \text{ then: } g(x) * h(x) \rightarrow G(k) \cdot H(k), \quad (4.4)$$

$$g(x) \rightarrow G(k), h(x) \rightarrow H(k) \quad , \text{ then: } g(x) \cdot h(x) \rightarrow G(k) * H(k), \quad (4.5)$$

where g and h can be arbitrary functions and G and H their corresponding Fourier transform representations, respectively. This example shows a transformation between the spatial domain (x) and the wavenumber domain (k), but also holds for the more well known transformation between temporal domain (t) and frequency domain (f).

When applied to the problem of the finite receiver, the multiplication of the boxcar function with the full wavefield can be represented by the convolution of the Fourier transformed boxcar function, i.e. the sinc function, with the SRS. For simplicity the explanation will be given using the sinc function. Usually in digital signal processing a windowed sinc function or a smooth boxcar function is used to increase the stopband attenuation (decay of sidelobing) with an additional loss of spectral resolution [21]. The process of windowed filters is usually a trade-off between stopband attenuation and resolution.

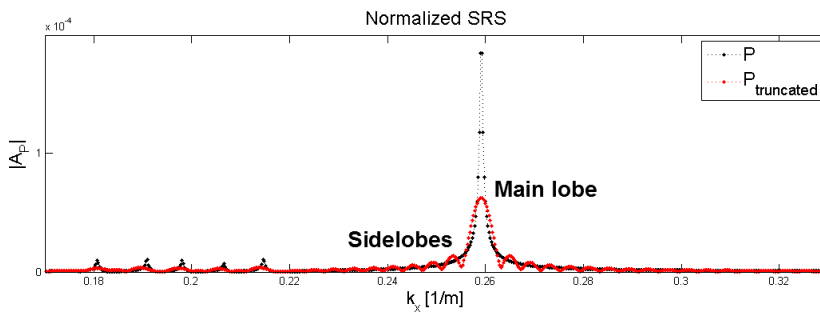


Figure 4.8: Truncated and untruncated example of a SRS for a modeled response as an example. Clearly visible is the spreading of energy over the main lobe inducing a decrease in spatial resolution and over the sidelobes.

What happens during the convolution is that the energy of the spectrum is spread out over the different wavenumbers. This energy will be primarily concentrated over the main lobe of the sinc function, called “spectral leakage”, and partially over the sidelobes of the sinc function, see figure 4.8. The major consequence of this spreading of energy is that events in the spectrum can be masked by either the spectral leakage of the main lobe or can get lost in the sidelobes or ripples.

When considering that the peaks of the dispersion curve, i.e. the modes of the soil response, are characteristic properties of the soil, they provide important information regarding the soil parameters investigated. It is of high importance to capture these modes as well as possible.

The role of spectral resolution is two-sided: on the one hand capturing as much as practically possible of the wavefield during seismic measurements is vital for the success of an inversion, and on the other hand during modeling of the wavefield the

spectral resolution should be high enough to capture all the characteristic modes of wave propagation. The capturing of wavefield components is handled in this section and the modeling of the response is handled in section 3.3.

As previously mentioned before in a seismic measurement the spatial resolution is directly related to the receiver length or aperture. It defines the information that is present in a measurement i.e. the minimum stepsize of wavenumbers that will contain information of the wavefield. It can also be seen as the width of the peaks that are present in a measurement.

$$dk = \frac{1}{\lambda_{max}} = \frac{1}{N_{rcv}\Delta x}, \quad (4.6)$$

in which the dk represents the stepsize in the wavenumber domain, λ_{max} is the maximum resolvable wavenumber and N_{rcv} is the number of receiver arrays. Zero-padding can be introduced to increase spatial resolution by virtually increasing N_{rcv} with a zero response (zero padding), but bear in mind that this procedure does not increase the information available in the measurement.

4.2.5 Scaling and windowing of the shot record

The traces are scaled with their root mean squared value (RMS) to decrease the high influence of the near field with respect to the far field. This causes the dispersion curves to be more pronounced in the data. In addition, the Scholte wave seems to have a similar energy levels as the higher mode, which is beneficial in the inversion of shear waves. In the far-field the measurement is governed by the Scholte wave and increasing the influence of the far field increases the visibility of the Scholte wave in the spectrum. The RMS value of the surface response is defined according to equation 4.7. The spectra before and after are plotted in figures 4.9.

$$P_{RMS}^{(meas)}(x) = \sqrt{\frac{1}{N} \sum_{t=1}^{N_t} |P^{(meas)}(x, t)|^2}, \quad (4.7)$$

where xx and tt are the samples of the data in space and time, the pressure P is the measured response. Notice that each trace or sample xx in the above equation has its own RMS value. The same RMS scaling is applied to the modeled data except that the modeled RMS value is calculated.

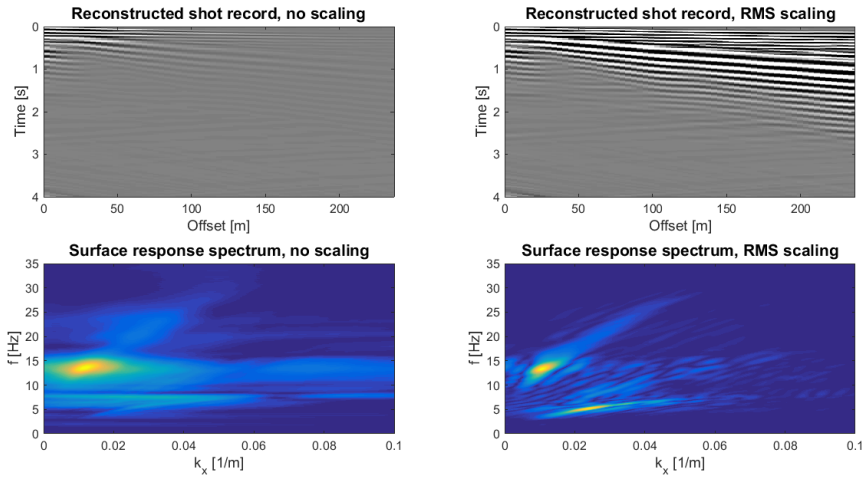


Figure 4.9: Top left: Shot record without scaling; bottom left: SRS without scaling; top right: RMS scaled shot record; bottom right: RMS scaled SRS.

Due to the increased amplitudes at the far offset the sidelobing of the solution will also increase, since a larger discontinuity is found at the boundaries. A stretched Hanning window is applied to the dataset to decrease sibelobbing i.e. a smooth box-car function is applied as a window. However, a decrease in spatial resolution is the consequence of this process. This window will also increase the influence of the first 16 traces in the dataset, these traces are filled and are therefore not completely reliable. Three options for the window and their corresponding SR spectra are shown in figure 4.10. The windows are tapered towards zero for the first and last traces of the window. The windows considered are Hanning windows where the first and last 25, 50 and 100 traces are tapered; this is represented in the top left inset of figure 4.10. The choice was made to taper the first and last 100 traces, this choice is explained in section 5.2.3.

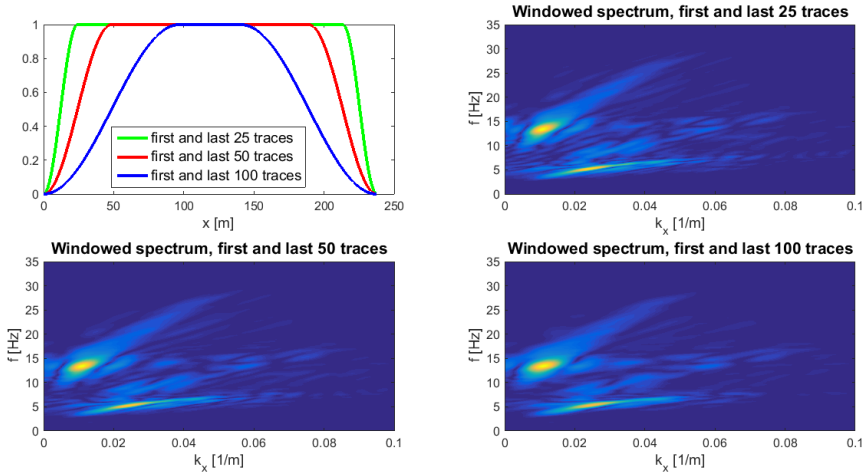


Figure 4.10: Windowed surface response spectrum. Top left: a representation of the different windows used; Top right: SRS windowed with the first and last 25 traces tapered to zero; Bottom left: SRS windowed with the first and last 50 traces tapered to zero; Bottom right: SRS windowed with the first and last 100 traces tapered to zero.

4.3 Summary and conclusions

A multi-channel surface array measurement was performed in the IJsselmeer in the Netherlands. It consisted of multiple concatenated shot records that allowed us to obtain a shot record with an effective length of 237m.

Two locations were measured of which only the data from turbine location W27 was deemed reliable for our purposes. The background profiles of density and layer thickness were obtained from CPT measurements and borehole tests. It showed small layers of loose sand, soft clay and peat overlaying thicker medium dense to dense sand layers. Overall the soil consisted of a combination of sand, clay and peat layers.

The data consisted of hydrophone measurements meaning that pressures at the soil-fluid interface were measured. The concatenation of the different shot record was performed assuming that the direct arrival seen in the measurements is the

pressure wave running through the water layer and assumed to be 1450 m/s. The concatenation using this approach showed gaps in the effective dataset and were filled.

Frequency content of the first trace showed that the source function contained significant energy up to 200Hz. Surface wave information were limited to the first 50Hz and a low pass filter was applied to the data to separate surface wave data.

The traces were scaled with their RMS value to increase the influence of the far field. This resulted in a more pronounced presence of the Scholte wave. A higher mode of propagation of surface waves was also found in the data. Scaling introduced sidelobing and a stretched Hanning window tapered the first and last 100 traces slowly to zero. The dataset was eventually transformed to the 2D fourier domain or fk domain. This domain was chosen for the inversion, since the dispersion curves are visible and the model is more readily solved in this domain.

Chapter 5

Full waveform inversion of in-situ measured seismic data

The genetic inversion program is able to invert c_s and c_p in the ideal case i.e. the “inversion crime”, where a synthetic measurement is created using the same forward model as the modeled response within the inversion loop. The inversion applied to real data is, however, completely different. Here several assumptions are made regarding soil modeling. Comparison between the two via the fitness of the solution, depends highly on these assumption. Firstly, the measurement data is provided and interpreted. Secondly, an initial soil model is defined from CPT measurements. In addition, several remarks are given regarding damping parameters in the soil. Finally, several runs are done using real measurements for estimating the shear wave velocity.

5.1 Measurement data

The shear wave related events are visible in the range from 0 to 50 Hz, since a low pass filter is applied to the data. This separated, to a large extent, the body wave related events from the surface waves. The SRS of the data is presented in figure 5.1. The figure clearly shows that the data is limited up to 35 Hz and 0.1 m^{-1} i.e. the lower left quadrant of the SRS. Two distinct dispersion curves are visible, one corresponding to higher phase velocities and one corresponding to lower phase velocities. The bottom low phase velocity dispersion curve is the Scholte wave, and is limited to the range between 3 to 6 Hz and 0.01 to 0.075 m^{-1} . The shape of the dispersion curve is governed by the soil within one wavelength of the waves consisting of the Scholte wave. For the Scholte wave this comes down to soil depths ranging from 13m to 100m.

The upper high phase velocity dispersion curve is related to higher modes of propagation of surface waves. It consists of a strong section and a weaker tail. The strong section is limited between 10 Hz and 15 Hz and 0.005 m^{-1} and 0.018 m^{-1} and the weaker tail extends to 35 Hz and 0.05 m^{-1} . If the higher phase velocity dispersion curve is indeed related to higher modes, the effects on the phase velocity of this higher mode is similar to the Scholte wave related to soil depths within one wavelength of the modes. For the strong section of the higher phase this is related soil depths ranging between 56m and 200m. The weaker tail corresponds to soil depths ranging between 20m and 56m.

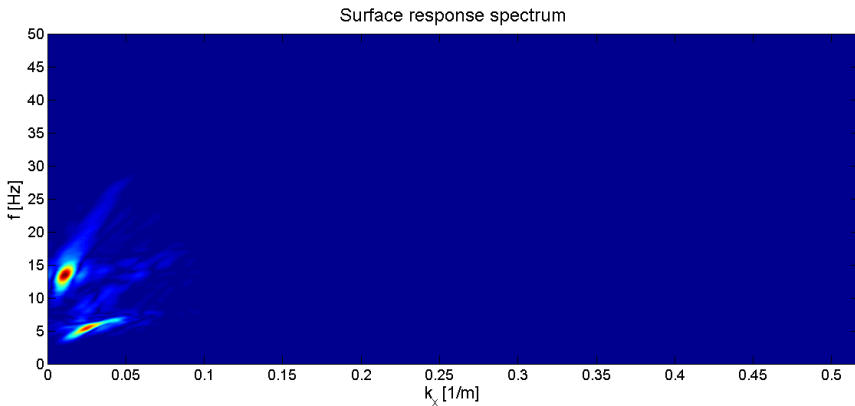


Figure 5.1: The full extent of the SRS of the measurement in the fk domain. It is clearly visible that the data is contained within the lower left quadrant of the spectrum.

Care must be taken when interpreting the strong section of the higher mode, because the soil depths governing the phase velocity of the waves are quite high with respect to the modeled soil layers. The modeled soil runs to 30 m and the wavelengths governing the higher modes strong section range from 56 to 200m, which means that the corresponding soil depths that this mode influences are two to seven times larger than modeled. Whether the stronger section of the higher mode is governed by the first 30 m is debatable, due to this high difference in influence depth and modeled depth.

The velocity of the fundamental mode or Scholte wave is mainly dependent on the near-surface layers in the model. If these layers have high velocities, the Scholte wave has a high phase velocity dispersion curve. On the other hand, if these layers consist of low velocity layers, the dispersion curve shows low phase velocity.

The main difference between the SRS of the modeled response and that of the measurements is that the dispersion curves of the measurements only consist of the lower left quadrant of the spectrum, while the modeled ones run throughout the spectrum. This might be caused by the limited knowledge of damping within the structure. So far the modeled response has been modeled with a small, time-related damping parameter to overcome the singularities of the dispersion equation. However, larger values of damping might exist in the soil. When larger values of damping ratios are considered, the peaks could match better. In addition, the dispersion curves of the surface waves are influenced by the layers of the soil that are located approximately as deep as the wavelengths of the surface waves are long. The same holds for the damping of these curves. Higher wavenumbers correspond to smaller wavelengths and vice versa, therefore the lack of visibility of the modes at higher wavelengths could be caused by higher damping values within the more shallow layers. Moreover, higher wavenumbers correspond to higher frequencies or more oscillations per time interval and, therefore, these waves will be damped out faster in time.

5.2 Initial soil model

Before the inversion can be started several choices must be made regarding the scaling and window used. To be consistent with the measurement data the same scale and window must also be applied to the modeled data. The effect of these processes might have more influence on the modeled data and will be investigated in this section. In addition, the influence of damping on the SRS is investigated. An initial soil model, consisting of 8 layers, is used and displayed in the table 5.1. The initial soil model is based on the CPT measurements performed for this windturbine location (W27), displayed in table 4.3. The very small deeper peat layer from table 4.3 (layer 10) is merged in the above clay layer, since the small layer might not be detected in the inversion. The soil layers run up to -20.6m below seabed, keep in mind that the halfspace represents a layer of 10m.

Table 5.1: Initial soil model based upon CPT measurements and MASW report proposed by Fugro Geoservices.

Start model	Depth from seabed	Layer thickness	Density	C_s	C_p
layer #	m	m	kg/m^3	m/s	m/s
layer 1	+4.4	4.4	1000	0	1450
layer 2	-2	2	1900	75	1500
layer 3	-2.6	0.6	1500	75	1450
layer 4	-3.3	0.7	1000	75	1600
layer 5	-8.6	5.3	2000	200	1650
layer 6	-9.6	2000	300	1700	
layer 7	-16.1	6.5	2000	280	1700
layer 8	-19.4	3.3	2000	260	1600
layer 9	-20.6	1.2	1800	260	1600
Halfspace	inf	2000	280	1600	

5.2.1 Damping

The damping considered is hysteretic and equal for damping ratios D_p and D_s . The surface response spectrum for different damping ratios is plotted in figure 5.2. Corresponding slices at frequencies of 8 and 25 Hz are presented in figure 5.3. These slices are normalized such that total energy of every spectrum is unity. As expected adding damping increases the width of the peaks. Typical damping ratios for hysteretic damping occurring in soil lie between 1% to 10%, [2] and [20]. In this thesis the damping ratios are assumed to be not greater than 5%.

5.2.2 Impact of RMS scaling

As explained in section 4.2.5 the RMS scaling increases the influence of the far field i.e. it can be seen as a reduction of the damping in the shot record. The result is that spectral resolution is increased, making the peaks smaller, see figures 5.4. However, the effect of sidelobbing increases due to the larger discontinuity at the edges of the truncation, 5.5. To ensure consistency between modeled and measured data the same processes must be applied. It must be noted that for damping ratios larger than 1%, no sidelobbing or little sidelobbing is encountered. For the data containing shear waves, the time of the measurement (T) and length of the receiver (X) are long enough to allow the signal to be almost completely damped out at the boundary of the window.

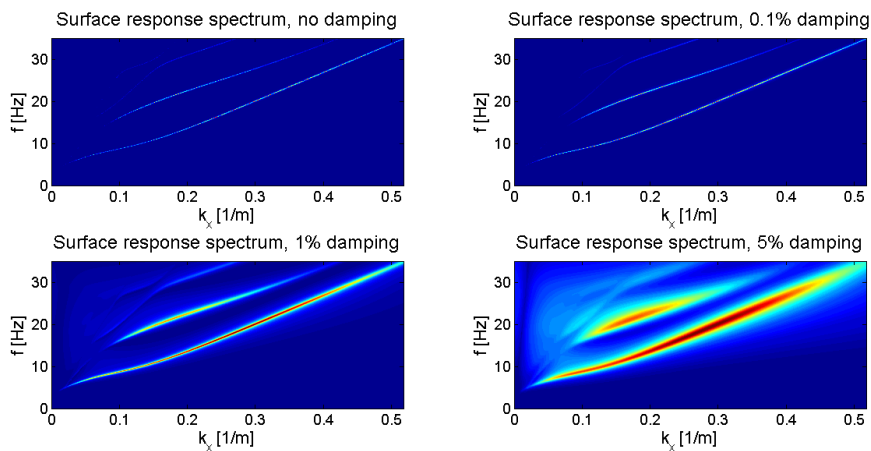


Figure 5.2: Surface response spectra for the initial soil model using damping ratios equal to 0, 0.1, 1 and 5%.

5.2.3 Windowed spectra

The effect of sidelobing can be reduced by applying a window. The windows are applied to the shot record (i.e. time offset domain) and are the same as defined for the measurements in section 4.2.5. To summarize, three stretched hanning windows are applied where the first and last 25, 50 and 100 traces are tapered to zero and are applied separately to the modeled data. The results are displayed in figure 5.6 for slices at frequencies of 12, 25 and 37 Hz. It can be seen that windowing does not have a large effect on the SRS data, especially between tapering the first and last 25 traces and 50 traces. These two datasets still show significant sidelobing, therefore the chosen window is the one with the first and last 100 traces.

5.2.4 Increase of amount of layers in model

The higher mode found in the measured data was assumed to be caused by modes governed by deeper layers. It is therefore questionable if an 8 layer model running up to 30m in depth would be able to capture these modes properly. Three separate runs are performed for the starting model using a 2 layer profile, a 4 layer profile and an 8 layer profile. The 2 layer model uses the first two layers in the starting model (represented in table in table 5.1) and the third layer is considered to be the

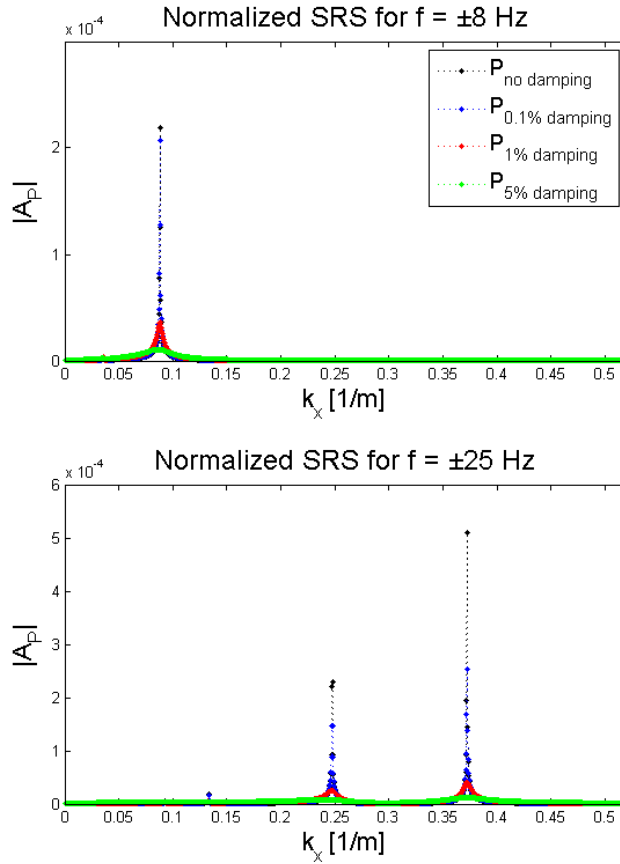


Figure 5.3: Slices of the surface response spectra for damping ratios equal to 0, 0.1, 1 and 5% for frequencies 8 and 25 Hz.

halfspace. The same holds for the 4 layer model, with the halfspace at location of layer 5 and the 8 layer model with the halfspace at location of layer 9.

The SRS of the separate runs are plotted in figure 5.7. The major differences are visible for the two layered model and only shows the Scholte mode properly, higher modes are not visible. However, the differences between 4 and 8 layers can not be distinguished. The differences lie in small variations in the dispersion curves and

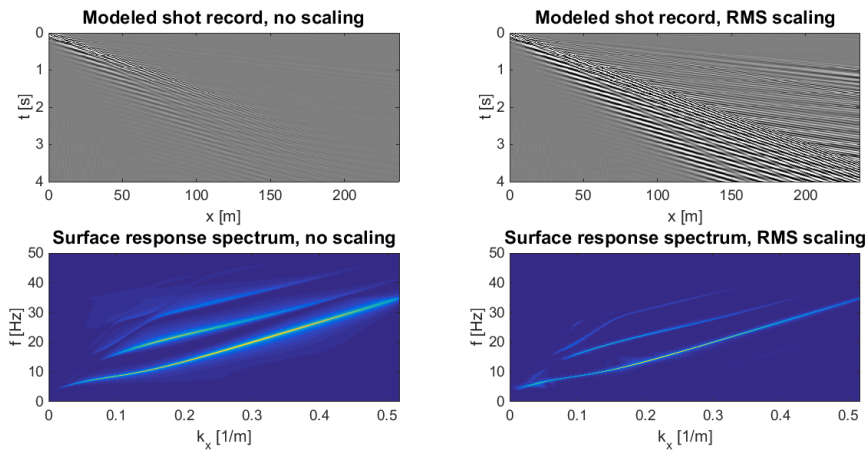


Figure 5.4: Top left: Shot record from initial model without scaling; bottom left: Surface response spectrum without scaling; top right: RMS scaled shot record from initial model; bottom right: RMS scaled surface response spectrum.

not necessarily in the amount of modes. An 8 layer model should be sufficient to capture the modes visible at the surface, and therefore also the higher mode visible in the measured data. On the other hand the curvature of the dispersion curves are not necessarily captured properly especially for the smaller wavenumbers i.e. longer waves. The differences between dispersion curves of the 4 layered model and 8 layered model might not be large enough to form a unique solution for deeper layers. However, the 8 layered model is used in the inversion, since modeling up to 30m is required.

5.2.5 Near-surface damping

One of the major differences between modeled and measured response are the visibility of the separate modes in the SRS. The modes of the measurements are visible within wavenumbers up to 0.1 m^{-1} . For the modeled response these modes run throughout the wavenumber spectrum. One explanation of this phenomenon can be given through damping. Remember that surface waves penetrate as deep into the soil as the corresponding wavelength. In addition, the damping of certain waves are dependent on this characteristic of surface waves. Waves with high wavenumbers (small wavelengths) are influenced by the near-surface layers. If in these near-

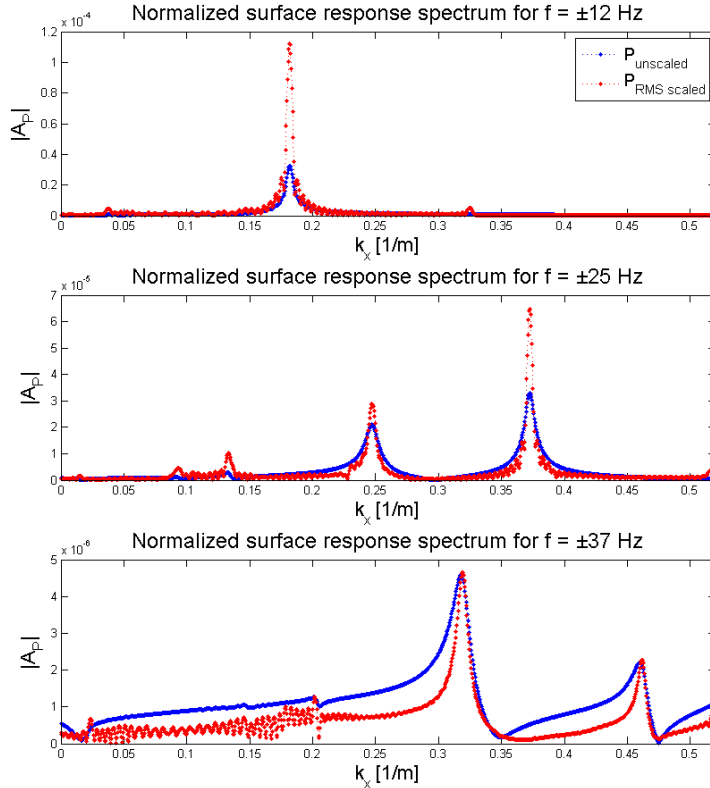


Figure 5.5: Slices of the SRS for the RMS scaled model and the unscaled model. Notice the smaller peaks and the increase in sidelobing in the scaled model.

surface layers the damping ratios are increased, the surface waves governed by these layers could be dissipated and a better fit between model and measurements can be found.

A larger damping coefficient of 3% is assumed in the first ± 10 m of soil corresponding to the first 4 layers. These layers consist of loose sand, clay and, peat overlaying a dense sand layer. The first 10 m are chosen because this corresponds to wavenumbers larger than 0.1 m^{-1} or wavelengths smaller than 10m. The resulting surface response spectrum is plotted in figure 5.8. The model shows indeed a reduc-

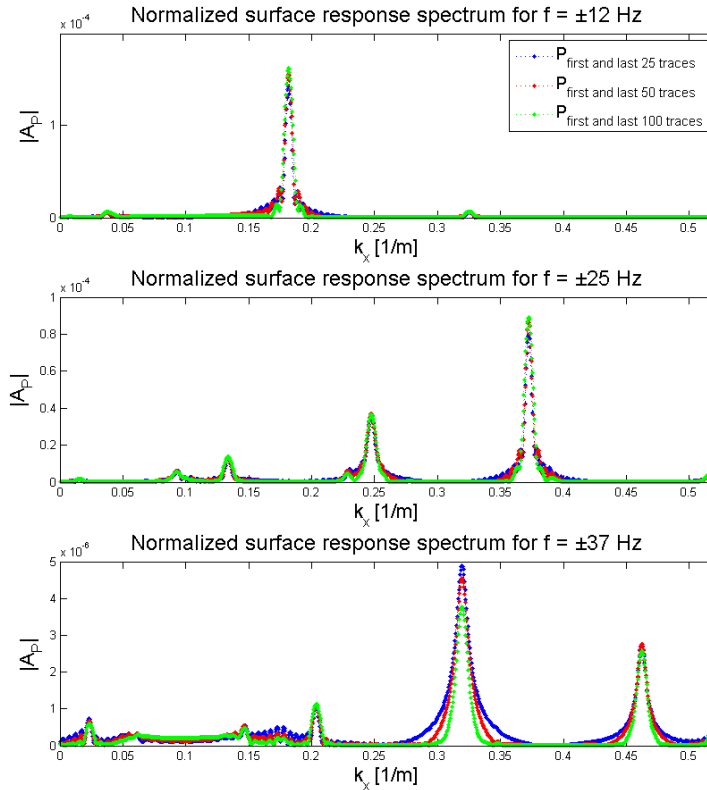


Figure 5.6: Slices of the windowed SRS. The windows applied are hanning windows, where the first and last 25, 50 and 100 traces are tapered to zero.

tion of the surface waves with increasing wavenumbers. Even though the modes are still visible at the higher wavenumbers, the energy is located in the lower wavenumber region. A high phase velocity non-dispersive event also becomes visible in the spectrum, a phase velocity of approximately 1500 m/s is found and suggests that it is related to the direct arriving p-wave or to a refraction. It is related to a body wave event, since it has a higher phase velocity than the maximum shear wave velocity found in the soil model.

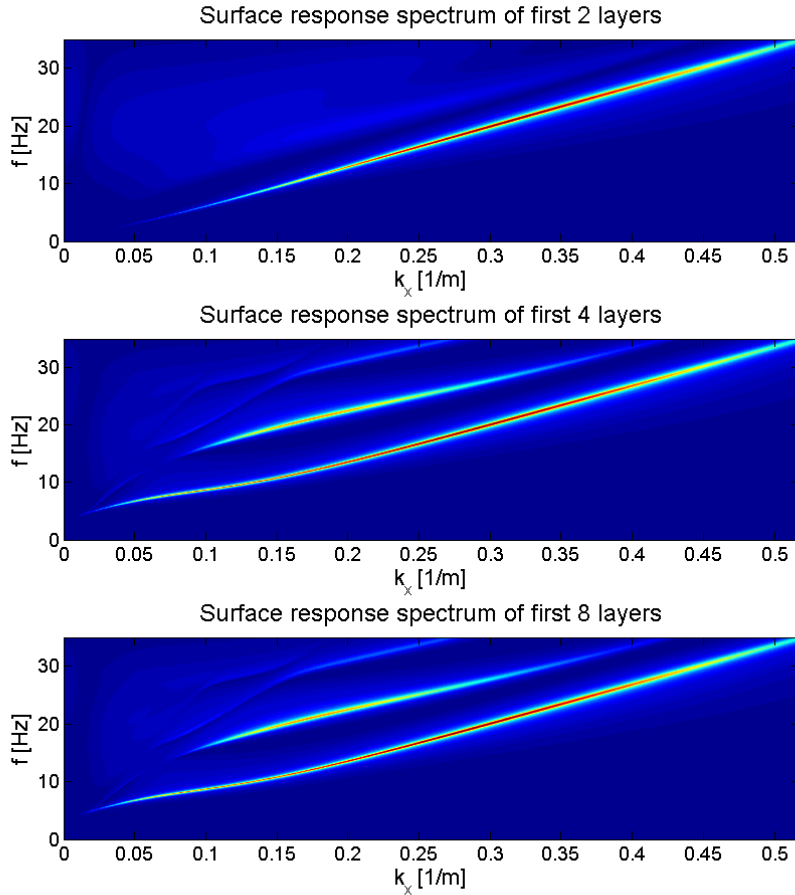


Figure 5.7: Surface response spectra for a 2 layer model, a 4 layer model and an 8 layer model.

5.2.6 Higher mode surface wave

The high energetic peak visible in the SRS of the measurements is –according to investigations by Fugro– related to higher modes of propagation of surface waves and governed by deep soil layers [23]. The high phase velocity surface wave should become visible if a high shear wave velocity is found in the structure. Since it is

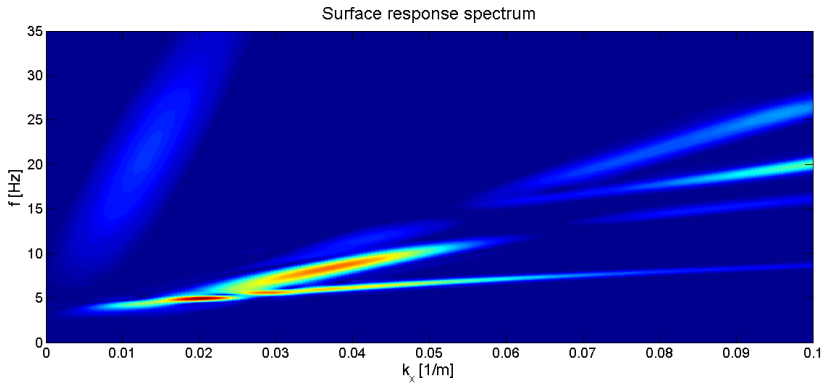


Figure 5.8: Surface response spectrum of model with 3% damping in the first 4 layers.

related to the deeper layers, the halfspace is chosen to have a velocity of 800 m/s. This value of shear velocity would include the mode visible in the measurements. The result is plotted in figure 5.9. Figure 5.9 shows that higher modes of surface waves become visible at a similar location of the high phase velocity surface wave in the measurement, although not as energetic. This does suggest that the model could find a higher mode surface wave or combination of modes that resembles the higher mode found in the measurements.

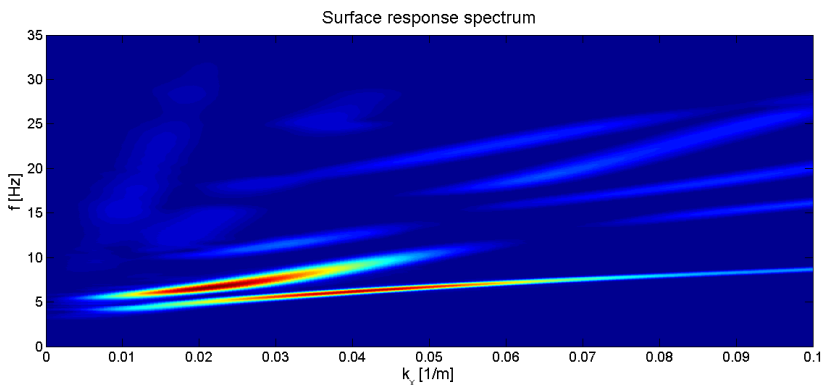


Figure 5.9: Surface response spectrum of model with 3% damping in the first 4 layers and high shear velocity in the halfspace

5.3 Inversion of measurement data

5.3.1 Inversion runs

For the inversion process the assumption has been made that c_p was known a-priori. The initial runs consisted of several cases with different starting profiles. The 8 layer model presented earlier will be used. The damping ratios are considered equal for D_p and D_s with a value of 1% except in the upper 4 layers of the soil where a value of 3% is applied for both damping ratios. The general settings of the run are summarized in table 5.2 and table 5.3. All runs were performed using a Ricker wavelet with a central frequency f_0 of 20 Hz. The starting shear wave velocity profiles and the considered ranges are displayed in table 5.4. The halfspace velocity, as discussed earlier in this thesis, set to a high value of 800 m/s and was not allowed to change. These settings of the program allowed us to verify 4200 runs in approximately ten hours using 4 nodes with 2 Intel quad core Xeon cpus (32 processors with 2,66 GHz) in a parallel configuration.

Table 5.2: Settings for forward model of inversion.

Settings	df/dt	f_{max}/T	dk/dx	k_{max}/X	n_t	n_x
	Hz/s	Hz/ms	m^{-1}/m	m^{-1}/m	-	-
Forward model	9.766e-2/5	99.9/4	5.05e-4/0.97	0.518/237	2048	2048

Table 5.3: Settings for inversion program.

Settings	Gen.	Pop.	$\#_{conts}$	P_{mut}	$\#_{dads}$
	-	-	-	-	-
Genetic algorithm	70	60	30	0.25	20

Table 5.4: Pre-defined profiles and the search ranges for the algorithm.

	Run	1	2	3
$c_{s,range}^{(1)}$	m/s	75 ± 25	75 ± 25	75 ± 25
$c_{s,range}^{(2)}$	m/s	75 ± 25	75 ± 25	75 ± 25
$c_{s,range}^{(3)}$	m/s	75 ± 25	75 ± 25	75 ± 25
$c_{s,range}^{(4)}$	m/s	200 ± 75	200 ± 75	400 ± 150
$c_{s,range}^{(5)}$	m/s	300 ± 75	300 ± 75	400 ± 150
$c_{s,range}^{(6)}$	m/s	280 ± 150	400 ± 150	400 ± 150
$c_{s,range}^{(7)}$	m/s	260 ± 150	400 ± 150	260 ± 75
$c_{s,range}^{(8)}$	m/s	260 ± 150	400 ± 150	260 ± 75
$c_{s,range}^{(HS)}$	m/s	800 ± 0	800 ± 0	800 ± 0

Inversion run 1

The shear wave velocity profile found for the inversion of the first run is displayed in figure 5.10 and 5.5. The thick yellow line presents the initial shear wave profile and the considered ranges from this profile are displayed in the shaded gray area. The blue line is the mean of the eleven best found results and the the dark green shaded area the standard deviation of these best found profiles around the main. A large standard deviation suggests that this profile is having trouble converging, this must be considered with respect to the range (a large range generally suggest a larger deviation).

The corresponding surface response spectra show significant differences between the two and explain the low fitness of the inversion, as seen in figure 5.11. It seems that the higher mode in the measurement cannot be properly produced by the model within the ranges considered in this case. However, the differences are so severe that it cannot be related to the difference in source spectra of measured and modeled response. This can be clearly seen when the contribution to the suitability per frequency-wavenumber combination is plotted in the bottom inset of figure 5.11. This contribution is the cross-correlation without summation across wavenumber and frequency, the integration of the figure results in the value presented by the suit in equation 3.1.

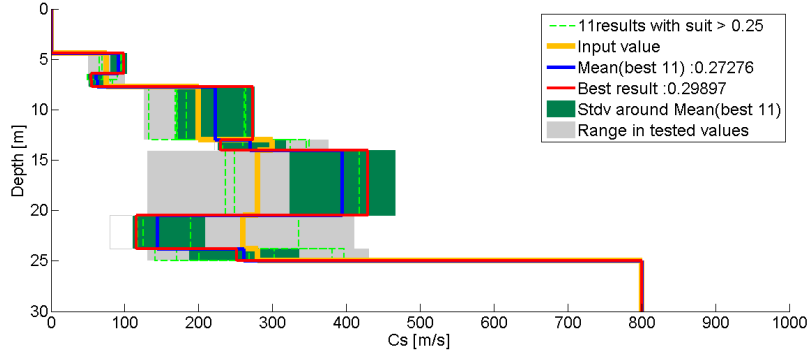


Figure 5.10: Results of the inversion of shear wave velocity for run 1.

Table 5.5: Results of inversion run 1.

Soil layer i	$c_{s,i}^{(best\ fit)}$	$\bar{c}_{s,i}^{(pop.best)}$	$\sigma_{s,i}^{(pop.best)}$
-	m/s	m/s	m/s
1	99	90.9	11.2
2	54	61.1	11.2
3	55	62.9	12.5
4	273	222.3	53.3
5	230	269.5	48.2
6	429	394.2	71.4
7	116	143.6	64.3
8	252	260.9	74.7
HS	800	800	0.0

A value of the suitability of approximately 0.3 was found and does not suggest a proper inversion. Only eleven results were found that have a similar or higher value than 0.25. This could suggest that 70 generations and a population size does not allow the solution to converge. However, this would also suggest that the starting profile is far from the actual profile.

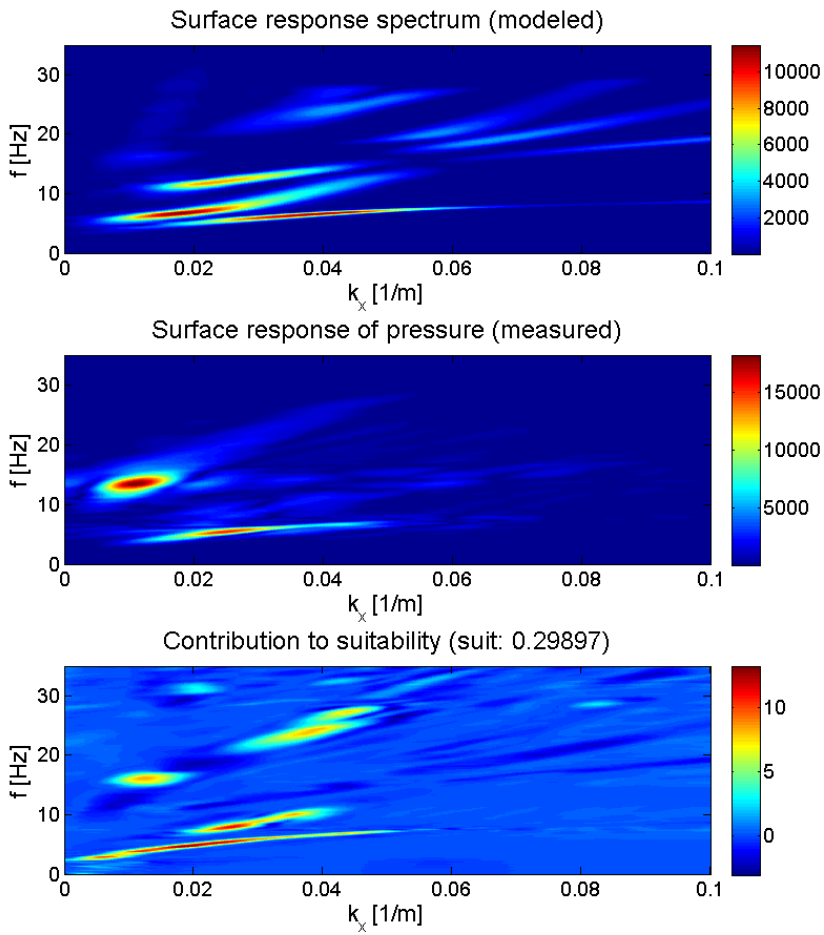


Figure 5.11: Dispersion spectrum of best fit result of inversion run 1 compared to the measured spectrum. The contribution to the suitability is plotted in the bottom inset.

Inversion run 2

To see if a larger deviation from this profile would be better suitable, a second run was performed by increasing the range of possibilities in the lower layers. From the large differences between the spectra especially in the higher modes, it was expected that higher velocities or differences in velocities are required to increase the fitness. The higher modes are probably related to larger depths, therefore deeper layers were proposed to have higher initial velocities. The results of the shear wave velocity inversion is provided in figure 5.12 and 5.6.

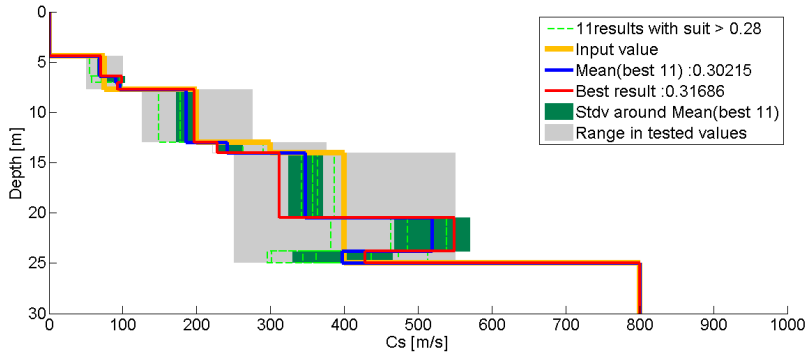


Figure 5.12: Results of the inversion of shear wave velocity for run 2

Table 5.6: Results of inversion run 2.

Soil layer i	$c_{s,i}^{(best\ fit)}$	$\bar{c}_{s,i}^{(pop.best)}$	$\sigma_{s,i}^{(pop.best)}$
	m/s	m/s	m/s
-	70	69.3	4.4
1	99	90.6	10.7
2	93	90.1	12.3
3	197	189.2	12.9
4	228	256.4	33.6
5	312	343.9	49.8
6	549	509.3	61.3
7	428	420.1	63.2
HS	800	800	0.0

This result shows a completely different profile with respect to the first inversion run, without a significant increase in fit. The most significant difference between run one and two is the difference of layer 7, for which the shear velocity in run one is converging to a low velocity and for run two it seems to converge to a high velocity, (± 120 m/s and ± 550 m/s).

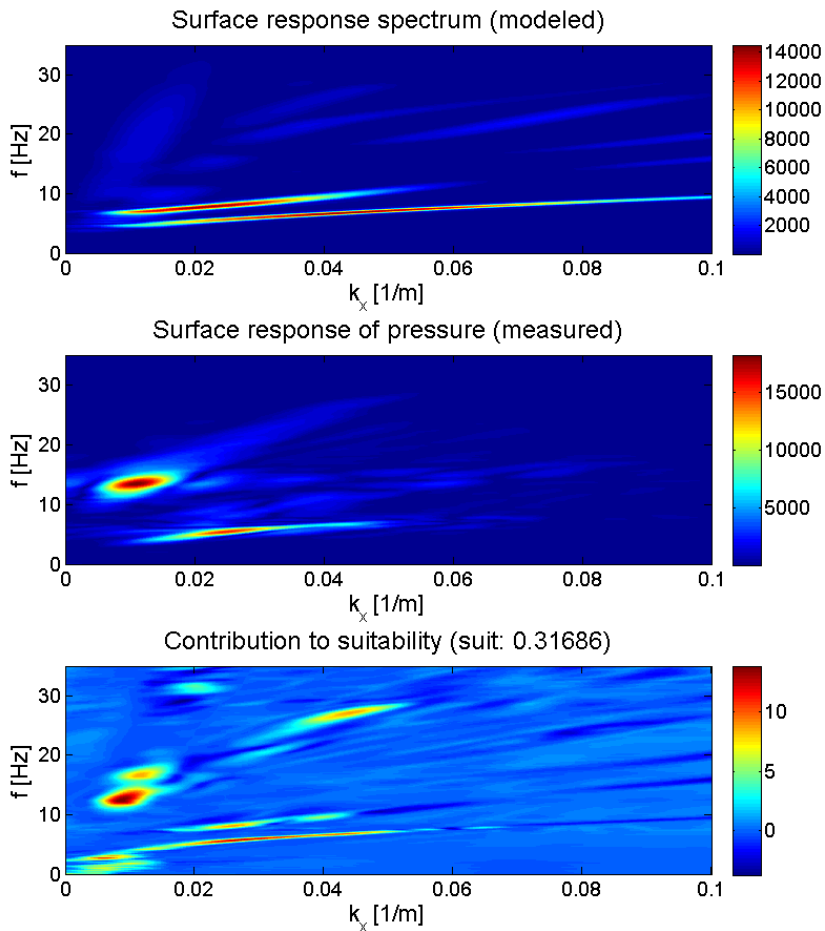


Figure 5.13: Dispersion spectrum of best fit result of inversion run 2 compared to the measured spectrum. The contribution to the suitability is plotted in the bottom inset.

The contribution to the suitability per frequency wavenumber shows similar results as before, again the Scholte wave has a high contribution and several higher modes make a contribution, see the bottom inset of figure 5.13. One thing that does stand out, is the high contribution of the highly energetic section of the higher mode visible in the measurement. This observation suggests that the higher mode in the measurement indeed is a combination of higher modes visible in modeled response and not a single mode. A slightly higher suitability is found compared the first inversion, a value of approximately 0.32. Eleven solutions were found with a fitness of 0.28 or higher.

Inversion run 3

To see the effect of increased velocities at the middle layers, three high velocity middle layers are considered in the last run. The results of the shear wave velocity inversion are plotted in figure 5.14 and table 5.7.

A significant increase in suitability with respect to the previous runs is the result. A value of 0.43 is found and the inversion suggests a very high near surface stiff layer in layer 5 as seen in figure 5.14. Another interesting result is that layer 6 seems to completely converge to the lower bound velocity. This would suggest that for a proper result this layer requires a low velocity.

A proper comparison between the surface response spectra is still not reached, although a relatively high energetic combination of higher modes is visible in the modeled response. The contribution to the suitability shows that indeed with this profile the highly energetic upper dispersion curve shows a better fit. A maximum suitability value of approximately 0.43 is found and eleven best results are found with a suitability of 0.4 or higher.

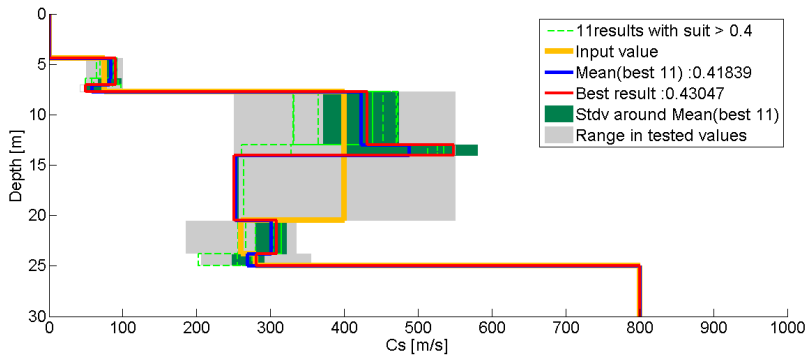


Figure 5.14: Results of the inversion of shear wave velocity for run 3.

Table 5.7: Results of inversion run 3.

Soil layer i	$c_{s,i}^{(best\ fit)}$	$\bar{c}_{s,i}^{(pop.best)}$	$\sigma_{s,i}^{(pop.best)}$
-	m/s	m/s	m/s
1	90	82.9	8.8
2	90	81.8	15.1
3	50	56.0	14.2
4	431	425.1	67.1
5	548	486.5	77.2
6	251	289.5	73.8
7	308	291.3	38.8
8	281	269.3	32.5
HS	800	800	0.0

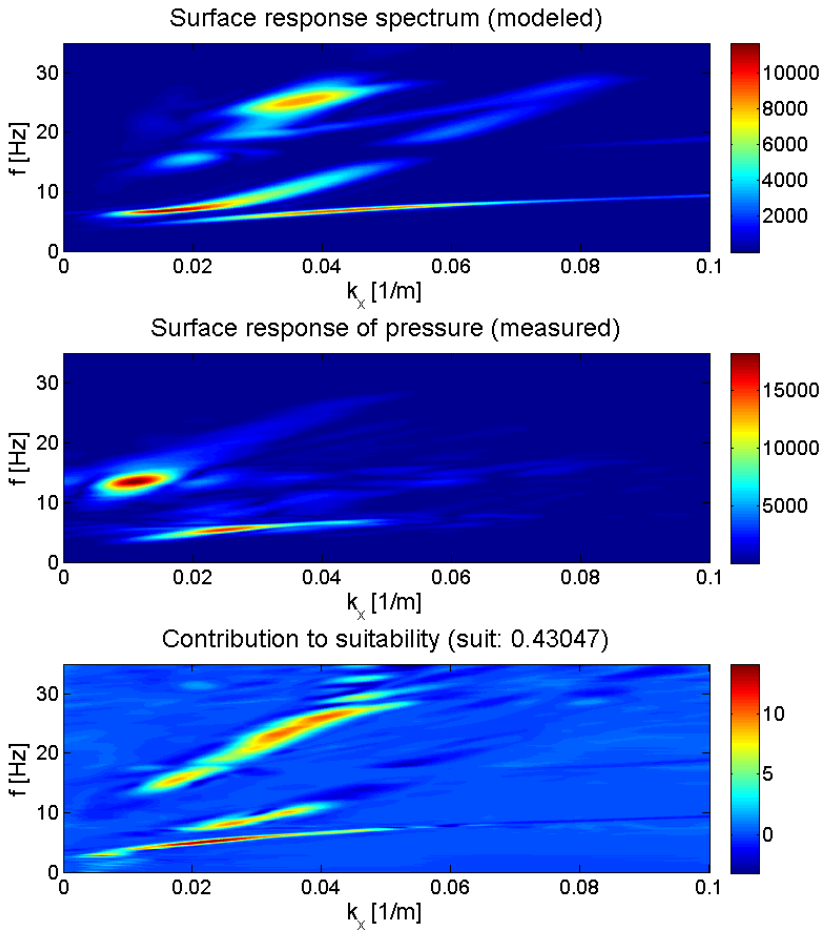


Figure 5.15: Dispersion spectrum of best fit result of inversion run 3 compared to the measured spectrum. The contribution to the suitability is plotted in the bottom inset.

Inversion run 4

A starting profile for run 4 is considered based upon the results of run 3. Smaller ranges of shear wave velocity are considered and the halfspace is allowed to vary. The initial model is given in table 5.8.

Table 5.8: Pre-defined profile and the search ranges for the algorithm considered for run 4.

	Run	4
$c_{s,range}^{(1)}$	m/s	90 ± 25
$c_{s,range}^{(2)}$	m/s	75 ± 25
$c_{s,range}^{(3)}$	m/s	75 ± 25
$c_{s,range}^{(4)}$	m/s	431 ± 75
$c_{s,range}^{(5)}$	m/s	548 ± 75
$c_{s,range}^{(6)}$	m/s	251 ± 75
$c_{s,range}^{(7)}$	m/s	308 ± 75
$c_{s,range}^{(8)}$	m/s	281 ± 75
$c_{s,range}^{(HS)}$	m/s	800 ± 100

A further increase in suitability is found and resulted in a value of 0.49. The best fitted result of shear wave profile is found in figure 5.16 and table 5.9. The most notable differences are that the value of shear wave velocity of layer 5 increases to over 600 m/s and suggest the presence of a hidden high velocity layer. Furthermore, the result layer 6 decreases to a velocity below 200 m/s . Finally the velocity of the halfspace seems to fit better when increased and suggests the presence of strong deep layers.

When considering the surface response spectra only a slight difference is noticeable, as seen in figure 5.17. Three high energy events are visible although different in size and slightly in position in the modeled spectrum. The mode corresponding to higher phase velocities visible in the modeled spectrum produces a better fit by matching with the tail of the higher mode visible in the measurements. The contribution to the suitability per frequency-wavenumber suggests on the other hand that a better fit is found through the tails of the dispersion curves, as seen in the bottom inset of figure 5.17. In the lower left corner of the spectra also a higher contribution to the suitability is found, however these results are questionable since they do not seem part of the specific curves.

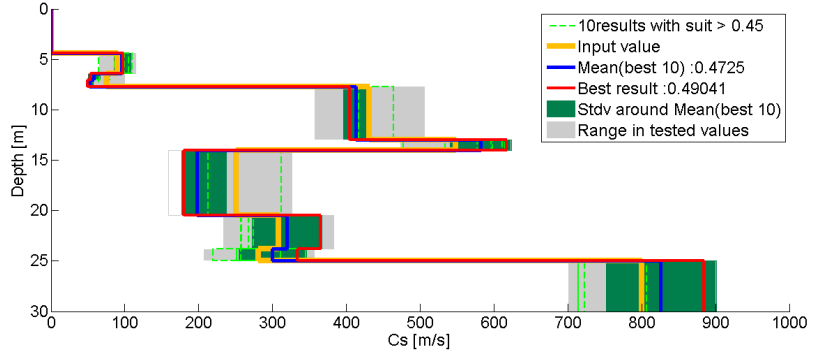


Figure 5.16: Results of the inversion of shear wave velocity for run 4.

Table 5.9: Results of inversion run 4.

Soil layer i	$c_{s,i}^{(best\ fit)}$	$\bar{c}_{s,i}^{(pop.best)}$	$\sigma_{s,i}^{(pop.best)}$
-	m/s	m/s	m/s
1	98	94.5	11.7
2	53	64.5	15.2
3	50	58.4	13.7
4	405	417.0	27.1
5	617	570.4	42.5
6	180	214.3	47.3
7	365	317.0	44.8
8	334	297.9	47.1
HS	884	831.1	64.1

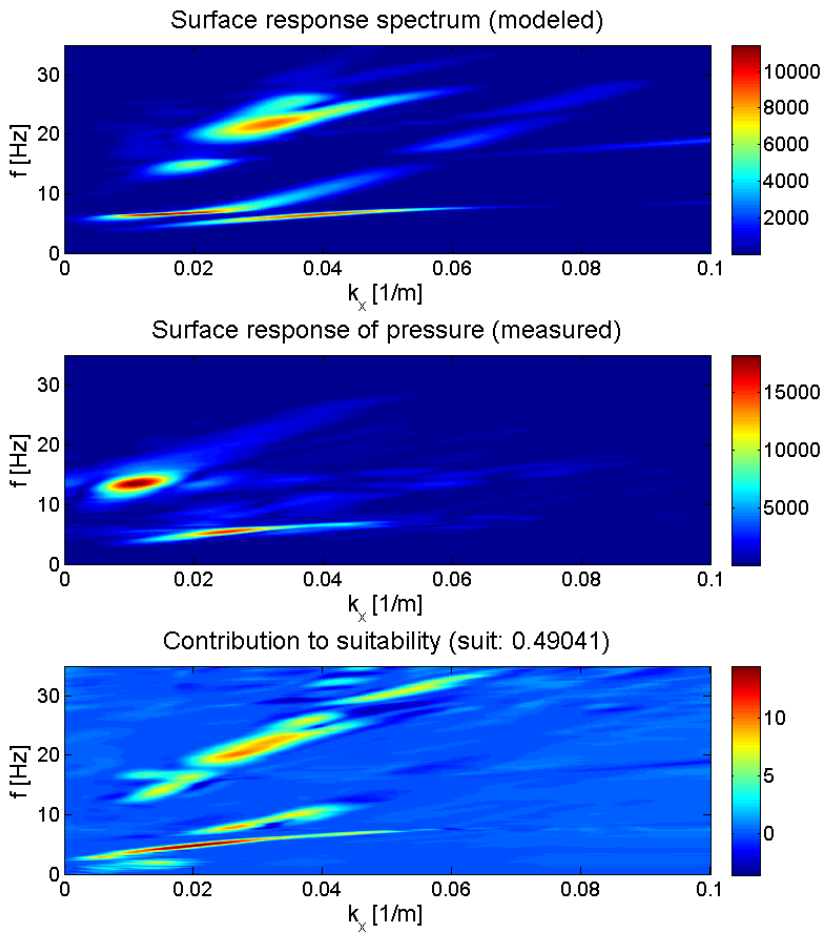


Figure 5.17: Dispersion spectrum of best fit result of inversion run 4 compared to the measured spectrum. The contribution to the suitability is plotted in the bottom inset.

5.4 Summary and conclusions

The SRS of the measurements showed that the majority of the data was contained in the lower left quadrant of the spectrum. To be precise the data was limited between 0 - 35Hz and between 0 - 0.1 m^{-1} . Two significant dispersion curves are visible, the Scholte wave and a combination of higher modes of propagation.

The initial model was introduced based on the background profiles for densities and layer thicknesses and resulted in a 8 layered model. A damping ratio of 1% was introduced with an additional 3% in the upper 4 soil layers. This showed a better fit between modeled and measured response. To be consistent with the measurement the same window and scaling is applied to the model.

Introducing multiple layers showed that at a certain point no or little influence in the SRS was found. Models up to approximately 10m showed little or no change in surface wave modes for the starting model introduced in the beginning of the chapter. This suggests that the higher mode in the measurement is influenced by the near surface. The 8 layer model should be able to model the higher mode in the measurement. However, this does suggest that within the first layers higher shear wave velocities must be present. Therefore a high velocity was introduced in the halfspace.

Several runs were proposed and resulted in a maximum suitability of 0.43 and suggested a high velocity in the near-surface. Continuation of this profile increased the fitness up to 0.49. The results did not yet show a satisfactory fitness and a better fit must be obtained. A better understanding of damping could result in a better fit.

Chapter 6

Conclusions

The main objective of this thesis was the estimation of dynamic properties of soil and application to in-situ measurements. In particular the s-wave velocity profile and p-wave velocity profile of the first 50m of the substratum. A full waveform inversion calculation combined with a genetic algorithm is used to invert for s-wave velocity and the program is adapted to incorporate p-wave velocity as well. A seismic measurement was performed at an offshore windfarm site in the IJsselmeer in the Netherlands. The inversion for the p-wave velocity profile is limited to ideal inversion or “inversion crime”. For the s-wave velocity profile estimation, the inversion was extended to actual measurement data.

Measurement inversion

- The main conclusion is that the differences between the spectra of the measured and modeled response are too big to make accurate statements regarding the success of the inversion algorithm. A fundamental physical property of the soil is clearly neglected in modeled response. The fit between modeled and measured data should be increased.
- Damping shows very high influence on the shape of the spectrum, not just the width of the modal peaks of the spectrum but the general shape as well as the extent and visibility of the modes.
- For the shear wave velocity profile the truncation of the signal in space and time seems of less importance than the influence of damping. Increasing the damping ratios to a range between 1% and 5% results in a better fit with respect to the width of the peaks. In addition, high near-surface damping decreases the visibility of the modes at larger wavenumbers and increases the fit.

- Inversions at this point are made with 4200 possible profiles (70 generations with population size of 60) and requires approximately 10 hours to run. The overall convergence of the program might not be reached and the program could converge prematurely to a local minimum. The full waveform is a computationally expensive process, therefore the time needed before convergence occurs could be significant. A better initial soil model should help with the convergence.
- Hysteretic material damping in its simplest form is introduced through a Kelvin-Voight model and considered to have similar values for shear wave damping and compressional wave damping. The near surface layers are assumed to have a damping ratio of approximately 3% and 1% in deeper layers. No influence of geometrical damping is considered. A more accurate or physically more correct damping model could be introduced, this would increase the convergence of the solution.

Potential of the algorithm

- In general, the velocities corresponding to the upper layers mostly affect the shape of the Scholte wave. A relatively close resemblance between the two was found, although the energy distribution was not found to be similar and could be improved by updating the damping ratios throughout the inversion process.
- The inversion of deeper layers was dominated by the high energetic peak of the higher mode of the surface waves found in the data. This caused the inversion to deviate largely from other methods of inversion. Fugro stated in their report that the inversion of the shear wave velocity for this specific site was only accurate for the inversion of the first 7 m. This supports the fact that the deeper layers could be inverted with higher accuracy using the full wave inversion, when a proper resemblance of the data is found.
- The significant differences in response spectra with changes in shear wave velocity per layer suggest that there indeed is a potential for the inversion of special cases such as near surface stiff layers. The phenomena of near-surface stiff layers might play an important role in soil structure interaction.
- In addition, the damping ratio profile has high influence on the SRS as well. This would suggest that the damping ratio profile could be inverted next to shear wave profile using full waveform inversion.

-
- The full waveform inversion at this point still requires user interpretation to verify what the algorithm is actually matching. This is in contradiction with conclusions of de Winter [6] who stated that no user interpretation was required. Although, the error sensitive process of actual mode picking is not required. The extent of user interpretation decreases with a better fit and requires less user interpretation.
 - The effect of truncation of the measurement data is small with respect to the influence of damping on the shape of the spectrum. For both shear wave and pressure wave velocity the inversion could be performed. However, in a later stage an increase of damping ratio was introduced from 0.1% to 1% and an additional increase in the upper 4 layers to 3%. The question arises whether the information within the measurement data range (0 - 35Hz and 0 - 0.1 m^{-1}) contains enough information to perform a proper inversion of the s-wave velocity profile.

Synthetic inversion

- Based on synthetic data the inversion of p-wave velocity and s-wave velocity was found to be possible. The inversion of the p-wave velocity profile required that the influence of surface waves was neglected in the inversion. In the synthetic data the separation of the surface waves from body wave related events could be easily performed, however, this was challenging in the actual measurements. The ability to estimate p-wave inversion from the performed measurement should be investigated further.

Chapter 7

Recommendations

There are several improvement opportunities for the inversion program. A better fit between model and measurements is absolutely necessary. A fundamental difference between modeled and measured response is visible and requires a improved soil model. In addition, several assumptions are made which contribute to the differences found. In this chapter several improvements are proposed and possibilities for further research are given.

Measurements performed

- First of all for only two locations data was obtained of which only one dataset was complete. This limited the inversion to only one dataset and no comparisons could be done. A better validation of the inversion program can be obtained when more data is available of different sites.
- An idea of the lateral variability of the soil can be obtained from performing the same shots on both sides of the receiver. Comparing the two results provides an idea of the lateral variation inside the soil of interest.
- The measurement where both receiver and source is displaced in order to let the wavefield propagate in the soil of interest as much as possible is preferred, provided in chapter 4. This would create a better idea of the soil of interest and therefore a better estimation of the parameters of the turbine site. However, in practice this was highly impractical and not performed.
- The geophone data was corrupted due to an incident with the deployment of the streamer. This resulted in a dataset where 20 of the 46 receivers displayed

no signal at all or a distorted signal. Geophone data could provide a meaningful addition to the interpretation of the results. Moreover, the entire inversion could be performed with geophone and hydrophone data.

- The lack of knowledge regarding the source spectrum was mitigated through a source independent misfit function. In theory the cross-correlation provides a fit independent of the source function, whether this works in practice must be verified. In addition, the source spectrum could become part of the inversion to improve the results. If this independent misfit function does not work satisfactory the source function could be included in the inversion process.
- The receivers used in the measurements are hydrophones which measure pressure response at the surface. No knowledge is known regarding the transfer function that describes the coupling between soil surface and hydrophone pressure. This could pose significant differences between modeled and measured response.

Inversion results

- The program is adapted such that inversion of p-wave velocity would be feasible, however the inversion required frequencies up to 250 Hz. Increasing the frequency range of the data increases the calculation time significantly, especially since wrapping in time and space due to the Fourier transform routine is quite severe for undamped systems. Increasing damping could decrease the effect of wrapping and a smaller time and space window can be applied.
- It is important that a proper model for damping is introduced in the model. This is a requirement for successful inversion of the measurement data.
- Proper knowledge regarding the initial soil model are of high importance i.e. background profiles of layer thickness, density, shear wave velocity, p-wave velocity and damping. It can decrease the user based interpretation and limits non-linearity of the inversion problem and is therefore beneficial for the success of the inversion. Malinowski [15] introduced the inversion of p-wave velocity profile and the attenuation factor from surface onshore seismic data using a visco-acoustic model. Results showed that attenuation factor and p-wave velocity could be successfully retraced. Prieux et. al. showed that this approach could be used as a reliable starting model for p-wave velocity, p-wave attenuation factor and even density for an subsequent elastic FWI [18] and [19]. The approach suggested a hierarchical process that included the estimation of the starting model from hydrophone data following an elastic FWI

process from geophone data. This approach could be interesting to investigate as a further step.

Assumptions regarding the model

- The model assumes perfectly horizontal stratification, however, this is not the case for actual soil. Significant different dispersion spectra can be obtained when the soil can vary laterally. The effect of lateral variation should be investigated.
- Behavior of offshore soil structures is found to be in very low frequency regions, approximately around 0.3 Hz. The dynamic properties and therefore also the behavior are estimated at much higher frequencies. Whether these parameters will give a good representation of soil behavior at the eigen-frequency of the windturbines, should be investigated.

Appendix A

Derivation of acoustic and elastic wave equations

This appendix shows the derivation of the acoustic- and elastic wave equations, and is the foundation of the forward calculation. The nonlinear equations of motion and continuity are provided. A combination between the two principles give the wave equations used in the forward model. Some important definitions and conservation laws are needed to derive the wave equations. The theory is mainly based on [25], [27] and [12].

A.1 Basic relations for wave propagation

Forces and stresses

Newton's law and Hooke's second law. Two important properties that are used: stress and strain. Stress tensor $\bar{\sigma}$ is the force working on surface with surface normal \bar{n} .

$$\lim_{\Delta S \rightarrow 0} \frac{\Delta \bar{F}}{\Delta S} = \bar{\sigma} \bar{n} \quad (\text{A.1})$$

Here ΔS is the surface with unit normal \bar{n} and $\Delta \bar{F}$ is the net force on this surface. The stress tensor is defined as:

$$\bar{\sigma} = \begin{pmatrix} \sigma_{xx} & \sigma_{xy} & \sigma_{xz} \\ \sigma_{yx} & \sigma_{yy} & \sigma_{yz} \\ \sigma_{zx} & \sigma_{zy} & \sigma_{zz} \end{pmatrix} \quad (\text{A.2})$$

The individual stress contributions are defined such that the stress $\sigma_{i,j}$ is defined that the stress in direction j working on the surface with normal in direction i .

$$\Delta F_x = \Delta y \Delta z [\sigma_{xx}(x + \Delta x) - \sigma_{xx}(x)] \quad (\text{A.3})$$

$$+ \Delta x \Delta z [\sigma_{yx}(y + \Delta y) - \sigma_{yx}(y)] \quad (\text{A.4})$$

$$+ \Delta x \Delta y [\sigma_{zx}(z + \Delta z) - \sigma_{zx}(z)] \quad (\text{A.5})$$

When dividing all terms in equation A.3 by the total volume ΔV yields the net volumetric force in x-direction

$$\frac{\Delta F_x}{\Delta V} = \frac{1}{\Delta x} [\sigma_{xx}(x + \Delta x) - \sigma_{xx}(x)] \quad (\text{A.6})$$

$$+ \frac{1}{\Delta y} [\sigma_{yx}(y + \Delta y) - \sigma_{yx}(y)] \quad (\text{A.7})$$

$$+ \frac{1}{\Delta z} [\sigma_{zx}(z + \Delta z) - \sigma_{zx}(z)] \quad (\text{A.8})$$

$$= \frac{\partial \sigma_{xx}}{\partial x} + \frac{\partial \sigma_{yx}}{\partial y} + \frac{\partial \sigma_{zx}}{\partial z} \quad (\text{A.9})$$

$$= \nabla \cdot \bar{\sigma}_x \quad (\text{A.10})$$

In a similar manner the results can be obtained for the net volumetric force in the other directions. This results in the following total net volumetric force vector:

$$\frac{\Delta \bar{F}}{\Delta V} = \nabla \cdot \bar{\sigma} \quad (\text{A.11})$$

Strain and displacement

The displacement vector $\bar{u}(\bar{r})$ expresses the displacement at location \bar{r} .

$$\bar{u}(\bar{r}) = [u_x(\bar{r}), u_y(\bar{r}), u_z(\bar{r})] \quad (\text{A.12})$$

The location \bar{r} is expressed in cartesian coordinates (x, y, z) . The spatial derivative of the displacement vector \bar{u} is given by:

$$\frac{\partial \bar{u}}{\partial \bar{r}} = \begin{pmatrix} \frac{\partial u_x}{\partial x} & \frac{\partial u_y}{\partial x} & \frac{\partial u_z}{\partial x} \\ \frac{\partial u_x}{\partial y} & \frac{\partial u_y}{\partial y} & \frac{\partial u_z}{\partial y} \\ \frac{\partial u_x}{\partial z} & \frac{\partial u_y}{\partial z} & \frac{\partial u_z}{\partial z} \end{pmatrix} \quad (\text{A.13})$$

Splitting equation A.13 in to an symmetric and an anti-symmetric part. The symmetric part is the strain tensor $\bar{\epsilon}$ and provides the ratio between deformation and original size or in more familiar form the strain of a bar element in one dimension $\epsilon = \Delta L / L$.

$$\epsilon_{ij} = \frac{1}{2} \left(\frac{\partial u_i}{\partial x_j} + \frac{\partial u_j}{\partial x_i} \right) \quad (\text{A.14})$$

$$\phi_{i,j} = \frac{1}{2} \left(\frac{\partial u_i}{\partial x_j} - \frac{\partial u_j}{\partial x_i} \right) \quad (\text{A.15})$$

For now the stress and strain of an cubic element at a certain location in space are defined. These two properties can be related through Hooke's law, or the constitutional relation. Before Hooke's law can be explained several other important relations must be derived. The following section derives conservation of momentum and conservation of mass.

A.1.1 Conservation of momentum

Conservation of momentum is a version of Newton's law and the definition is:

"The time rate of change of momentum of a volume is equal to the flux through the surface of the corresponding volume increased with the resultant force acting on the particles in the volume".

In equation form this can be written as:

$$\frac{\partial}{\partial t} \int_V \rho(\bar{r}) \bar{v} dV = \oint_S (\rho(\bar{r}) \bar{v}) \cdot \bar{n} dS + \bar{F}(V) \quad (\text{A.16})$$

Where \bar{F} is the net force on the cuboid and is equal to:

$$\bar{F}(V) = \oint_S \bar{\sigma} \cdot \bar{n} dS + \int_V \bar{f} dV = \oint_S \bar{\sigma}_n dS + \int_V \bar{f} dV \quad (\text{A.17})$$

In the above equations V is the integration volume, S is the surface of this volume, \bar{f} is the force per unit volume and \bar{v} velocity field. The stress in direction \bar{n} can be written is:

$$\bar{\sigma}_n = \bar{\sigma} \hat{n} \quad (\text{A.18})$$

with \hat{n} the unit normal vector in a direction in space. A simplified representation of Newton's law can be obtained when Gauss' theorem is applied to equations A.16 and A.17.

$$\int_V \frac{\partial(\rho\bar{v})}{\partial t} dV = - \int_V [\bar{v}\nabla \cdot (\rho\bar{v}) + (\rho\bar{v} \cdot \nabla)\bar{v}] dV + \bar{F}(V) \quad (\text{A.19})$$

$$\bar{F}(V) = \int_V \frac{\partial\bar{\sigma}_j}{\partial x_j} dV + \int_V \bar{f} dV \quad (\text{A.20})$$

The volume integral can be discarded since it holds for any volume and a simplification is the result:

$$\frac{\partial(\rho\bar{v})}{\partial t} + \bar{v}\nabla \cdot (\rho\bar{v}) + (\rho\bar{v} \cdot \nabla)\bar{v} - \frac{\partial\bar{\sigma}_j}{\partial x_j} = \bar{f} \quad (\text{A.21})$$

The assumption is made that the density and pressure only vary with small deviation from their initial value.

$$\left| \frac{\Delta p}{p_0} \right| \ll 1 \quad (\text{A.22})$$

$$\left| \frac{\Delta \rho}{\rho_0} \right| \ll 1 \quad (\text{A.23})$$

The linearized form of equation A.21 is the result and is referred to as the linearized equation of momentum:

$$\rho_0(\bar{r}) \frac{\partial^2 u_i(\bar{r}, t)}{\partial t^2} - \frac{\partial \sigma_{i,j}(\bar{r}, t)}{\partial x_j} = \bar{f}_i(\bar{r}, t) \quad (\text{A.24})$$

A.1.2 Conservation of mass

For any system it holds that mass needs to be conserved and is the last criteria required to describe particle motion. The definition of conservation of mass can be described as follows:

“The total amount of mass in a control volume V does not change in time”

$$\frac{\partial}{\partial t} (\bar{r}) dV = - \oint_S \rho(\bar{r}) \bar{v} \cdot \bar{n} dS + \frac{\partial}{\partial t} \int_V i_m dV \quad (\text{A.25})$$

Where i_m is the density of volume injection. This equation can be rewritten to a simplified form:

$$\frac{\partial \rho(\vec{r})}{\partial t} + \nabla \cdot (\rho(\vec{r}) \vec{v}(\vec{r})) = \frac{\partial i_m}{\partial t} \quad (\text{A.26})$$

No that the basic equations for a medium are derived the stress and strain can be related and Hooke's law can be formulated. Subsequently the wave equation is derived. First this is done for an acoustic medium end then a derivation is made for elastic media.

A.2 Acoustic media

One of the largest differences between acoustic media and elastic media is the existence of shear stresses in elastic media. In acoustic media no shear stresses exist and pressure can be related to stress according to:

$$\sigma_{ij}(\vec{r}, t) = -p(\vec{r}, t) \delta_{ij} \quad (\text{A.27})$$

The acoustic pressure p is equal to the sum of the longitudinal stresses:

$$\sigma_{xx} + \sigma_{yy} + \sigma_{zz} = -p \quad (\text{A.28})$$

A.2.1 Hooke's law in acoustic media

Conservation of mass without mass injection reads:

$$\frac{\partial \rho(\vec{r})}{\partial t} + \Delta(\rho(\vec{r}) \vec{v}(\vec{r})) = 0 \quad (\text{A.29})$$

Assumption of adiabatic processes corresponding to changes in pressure and volume. Meaning that there is no heat transfer in and out of the system, resulting in the fact that changes of internal energy can be described according to the acoustic equations of state:

$$\frac{\partial p}{\partial t} = \frac{1}{\chi \rho} \frac{\partial \rho}{\partial t} \quad (\text{A.30})$$

The property χ is the adiabatic compressibility described by:

$$\chi = \frac{1}{c^2 \rho} \quad (\text{A.31})$$

Where c is the speed of sound of an acoustic media. Substituting this relation into the equation of state gives:

$$\frac{\partial p}{\partial t} = \frac{1}{c^2 \rho^2} \frac{\partial \rho}{\partial t} \quad (\text{A.32})$$

Combining this relation with the conservation of mass without mass injection, equation A.29 yields the Hooke's law of an acoustic media:

$$\frac{1}{\rho c^2} \frac{\partial p}{\partial t} = -\nabla \cdot \bar{v} \quad (\text{A.33})$$

A.2.2 The acoustic wave equation

The conservation of momentum for an acoustic medium can be written as:

$$\nabla p = -\rho \frac{\partial \bar{v}}{\partial t} \quad (\text{A.34})$$

The acoustic wave equation can be found when the time derivative of the acoustic form of Hooke's law, equation A.33, is combined with the divergence of the conservation of momentum, equation A.34:

$$\frac{1}{\rho c^2} \frac{\partial^2 p}{\partial t^2} - \nabla \cdot \left(\frac{1}{\rho} \nabla p \right) \quad (\text{A.35})$$

An additional body force could be added on the right hand side for completeness.

A.3 Elastic media

The constitutive equation or Hooke's law is the three dimensional elastic equivalent to a one dimensional spring model.

$$\bar{\sigma} = -\bar{c}\bar{\epsilon} \quad (\text{A.36})$$

Where \bar{c} is a material dependent stiffness tensor.
Or:

$$\sigma_{ij} = \sum_{k=1}^3 \sum_{l=1}^3 c_{ijkl} \epsilon_{kl} \quad (\text{A.37})$$

The summation across k and l is usually not written down and is also known as the Einstein summation convention.

Or:

$$\sigma_{ij}(\bar{r}, t) - c_{ijkl}(\bar{r}) \epsilon_{kl}(\bar{r}, t) = -\sigma_{ext,ij}(\bar{r}, t) \quad (\text{A.38})$$

Where $\sigma_{ext,ij}$ is caused by an external strain tensor h_{kl} .

$$\sigma_{ext,ij}(\bar{r}, t) = c_{ijkl}(\bar{r}) h_{kl}(\bar{r}, t) \quad (\text{A.39})$$

The stress tensor can be written in terms of the displacements by using equation A.15:

$$\sigma_{ij} = c_{ijkl} \frac{1}{2} \left(\frac{\partial u_k}{\partial x_l} + \frac{\partial u_l}{\partial x_k} \right) - \sigma_{ext,ij} \quad (\text{A.40})$$

Isotropic media

Another assumption made regarding material behavior is that the elastic media responds the same in all directions, i.e. the solid is called isotropic. Hooke's law without external forces can be written as:

$$\begin{bmatrix} \epsilon_{xx} \\ \epsilon_{yy} \\ \epsilon_{zz} \end{bmatrix} = \frac{1}{E} \begin{bmatrix} 1 & -\nu & \nu \\ \nu & 1 & \nu \\ \nu & \nu & 1 \end{bmatrix} \begin{bmatrix} \sigma_{xx} \\ \sigma_{yy} \\ \sigma_{zz} \end{bmatrix} \quad (\text{A.41})$$

The Young's modulus or elastic modulus describes the force required to stretch the material in a certain direction. Usually what happens when material is stretched in one direction is that it contracts in the other direction. The ratio between the stretched elongation corresponding contraction is called the Poisson's ratio ν .

$$E = \frac{\text{stress}}{\text{strain}} = \frac{\sigma}{\epsilon} \quad (\text{A.42})$$

$$\nu = \frac{\text{transverse strain}}{\text{longitudinal strain}} = -\frac{d\epsilon_{transverse}}{d\epsilon_{axial}} \quad (\text{A.43})$$

Hooke's law can be inverted to give the stress as a function of strain:

$$\begin{bmatrix} \sigma_{xx} \\ \sigma_{yy} \\ \sigma_{zz} \end{bmatrix} = \begin{bmatrix} \lambda + 2\mu & \lambda & \lambda \\ \lambda & \lambda + 2\mu & \lambda \\ \lambda & \lambda & \lambda + 2\mu \end{bmatrix} \begin{bmatrix} \epsilon_{xx} \\ \epsilon_{yy} \\ \epsilon_{zz} \end{bmatrix} \quad (\text{A.44})$$

This equation is described in terms of the Lamé coefficients, and are elastic parameters related to the shear modulus, Young's modulus and Poisson's ratio through:

$$\lambda = \frac{\nu E}{(1 - 2\nu)(1 + \nu)} \quad (\text{A.45})$$

$$\mu = \frac{E}{2(1 + \nu)} \quad (\text{A.46})$$

Hooke's law can be written in terms of displacement when rewriting set of equations A.44.

$$\sigma_{ij} = \lambda (\nabla \cdot \bar{u}) \delta_{ij} + 2\mu \epsilon_{ij} \quad (\text{A.47})$$

Where δ_{ij} is the Kronecker delta. Combining the above equation with equation A.15, provides Hooke's law in terms of displacement:

$$\sigma_{ij} = \lambda \frac{\partial u_i}{\partial x_i} + \mu \left(\frac{\partial u_i}{\partial x_j} + \frac{\partial u_j}{\partial x_i} \right) \quad (\text{A.48})$$

Which can also be provided in vector form:

$$\bar{\sigma} = \lambda (\nabla \cdot \bar{u}) \bar{I} + \mu \left[\left(\frac{\partial \bar{u}}{\partial \bar{r}} \right) + \left(\frac{\partial \bar{u}}{\partial \bar{r}} \right)^T \right] \quad (\text{A.49})$$

A.3.1 The elastic wave equation

The elastic wave equation can be obtained when taking the divergence of Hooke's law, equation A.49, and substituting this in the linearized form of the equation of momentum, equation A.24:

$$\frac{\partial}{\partial x_i} \left(\lambda \frac{\partial u_i}{\partial x_j} \right) + \frac{\partial}{\partial x_j} \left[\mu \left(\frac{\partial u_i}{\partial x_j} + \frac{\partial u_j}{\partial x_i} \right) \right] - \rho \frac{\partial^2 u_i}{\partial t^2} = -\bar{f} + \frac{\partial_{ext,ij}}{\partial x_j} \quad (\text{A.50})$$

In vector form this becomes:

$$\nabla [\lambda (\nabla \cdot \bar{u})] + \nabla \left[\mu (\nabla \bar{u}) + (\nabla \bar{u})^T \right] - \rho \frac{\partial^2 \bar{u}_i}{\partial t^2} = \bar{f} + \nabla \cdot \bar{\sigma}_{ext} \quad (\text{A.51})$$

Appendix B

Fourier transforms and conventions

The transformation from FK domain to XT domain is done using a FFT algorithm, developed by DELPHI department of Technical University Delft. It consists of a complex and real fourier transform. This appendix elaborates on the differences between real and complex fourier transform. additionally several conventions are required for the algorithm to work properly, these are stated in this appendix as well.

B.1 The Fourier transform

Every signal can be represented by a summation of harmonic waves, with different amplitudes and phases. This is called the fourier transform and allows the transformation between time-offset (xt) domain to the frequency-wavenumber (fk) domain. The wave equations are for simplicity solved in the fk domain and the fourier transform applied to the wave equations are defined as:

$$\tilde{f}(\kappa_x, z, \omega) = \int_{-\infty}^{\infty} \int_{-\infty}^{\infty} f(x, z, t) \exp^{i(\kappa_x x - \omega t)} dx dt \quad (\text{B.1})$$

The inverse fourier transform is defined as follows:

$$f(x, z, t) = \int_{-\infty}^{\infty} \int_{-\infty}^{\infty} \tilde{f}(\kappa_x, z, \omega) \exp^{-i(\kappa_x x - \omega t)} d\kappa_x d\omega \quad (\text{B.2})$$

B.2 Truncation in time and space

The same transform is applied to take the receiver length and measurement time of the measurement into account. To apply a similar transform to the measured data and to truncate the signal, the discrete variant is required. The process of truncation involves a complex inverse Fourier transform across wavenumbers to offset and a real inverse fourier transform from frequency to time. At this point the signal can be truncated and transformed back. Again a real Fourier transform is applied from time to frequency and a complex transform is applied from offset to wavenumber. First the real Fourier transform is presented and then its complex representation.

The shot record is a real valued signal and allows us to state that the the real part in frequency domain is *even* and the imaginary part is *odd*. Or in other words the spectrum corresponding to negative frequencies is the complex conjugate of the spectrum corresponding to positive frequencies. The real fourier transform changes an N point signal into two N/2+1 point signals. The two output signals show the amplitudes of their corresponding cosine and sine waves (the harmonic components). The forward real discrete fourier transform representation is given as:

$$ReX[k] = \frac{2}{N} \sum_{n=0}^{N-1} x[n] \cos(2\pi kn/N) \quad (B.3)$$

$$ImX[k] = \frac{2}{N} \sum_{n=0}^{N-1} x[n] \sin(2\pi kn/N) \quad (B.4)$$

Complex addition of the cosine and sine waves allows the representation of the complex output signal. It's inverse counterpart can be represented as follows:

$$x[n] = \sum_{k=0}^{N/2} ReX[k] \cos(2\pi kn/N) + \sum_{k=0}^{N/2} ImX[k] \sin(2\pi kn/N) \quad (B.5)$$

The input of the routine requires only the calculation of half the frequencies in the response.

Since it cannot be said that the response of pressure or velocities has an *even* real part and an *odd* complex part across wavenumbers, a complex transform must be applied. The complex transform, transforms a N point complex signal to an equivalent N point complex signal. The forward complex discrete fourier transform

can be represented as:

$$X[k] = \frac{1}{N} \sum_{n=0}^{N-1} x[n] e^{-i2\pi kn/N} \quad (\text{B.6})$$

And the inverse complex discrete fourier transform:

$$x[n] = \sum_{k=0}^{N-1} X[k] e^{i2\pi kn/N} \quad (\text{B.7})$$

The amount of samples N is required to be a power of two i.e. 128, 256, 512, 1024, etc. It should be mentioned that a more sophisticated FFT algorithm could reduce calculation times, especially when larger datasets are required to be transformed. The signals are required to run from 0 - N-1 for the real transform. The built up of the spectrum for the transformation should be 0 - (N-1) df, and 0 - (N/2) dk, -(N/2-1)dk - -dk.

Appendix C

Mathematical conventions

This appendix elaborates on the mathematical background and the conventions used in this thesis. Additional information is given in the form of basic mathematical definitions or operations.

C.1 Coordinate system

The coordinate system used in the thesis is depicted in figure C.1. Every layer has a local z axis that are used to derive the wave equations in section 2.2.

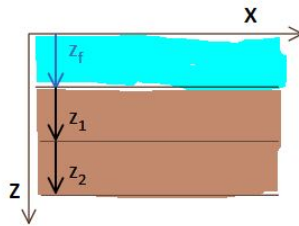


Figure C.1: Coordinate system used in this report. The local z -coordinates are also shown in this figure.

C.2 Calculation of the full wavefield

A solution to equation C.1 cannot be found if the determinant of matrix M equals 0. However, by adding damping the matrix M will not be singular.

$$M\bar{A} = \bar{f}. \quad (\text{C.1})$$

A standard approach is applied to find the indices of vector \bar{A} where the square of the residual is minimized:

$$\|M\bar{A} - \bar{f}\|^2. \quad (\text{C.2})$$

This thesis uses slightly adapted equations for calculation stability. First the rows of M are scaled such that they have the same order of magnitude:

$$M_{sca} = R_{sca}M. \quad (\text{C.3})$$

Based on M_{sca} , a hermitian matrix N can be calculated:

$$N = M_{sca}^* M_{sca}. \quad (\text{C.4})$$

N is inverted through LDU decomposition, and the solution can be calculated via:

$$\bar{A} = N^{-1} (M_{sca}^* (R_{sca}\bar{f})) \quad (\text{C.5})$$

C.3 Einstein summation convention

The divergence of vector \bar{w} can be written as:

$$\nabla \cdot \bar{w} = \sum_{x_i=x,y,z} \frac{\partial w_i}{\partial x_i} = \frac{\partial w_x}{\partial x} + \frac{\partial w_y}{\partial y} + \frac{\partial w_z}{\partial z}.$$

In the Einstein summation convention, the summation is left out:

$$\nabla \cdot \bar{w} = \frac{\partial w_i}{\partial x_i}.$$

Appendix D

A short guide to the numerical inversion tool

The Fortran program written by de Winter [6] is adapted to incorporate the inversion of pressure wave velocity. In addition, a FFT based convolution of the surface response is incorporated and allows the program to take the effect of a finite measurement length and time into account. The program is able to calculate a soil response provided a source function and proper background profiles. The full waveform model can be used to invert shear wave velocity and compressional wave velocity of soil up to 30m. This guide gives an overview of the most relevant options and adaptations to the inversion algorithm. This appendix is an adaption of the guide provided by de Winter.

D.1 Program functions

The program is able to invert either synthetic or actual measurement data. The synthetic data can either be finite-difference based or analytically produced based on the full waveform approach. The analytically produced data is obtained from a single run of the forward model. A sensitivity calculation can be done in two different manners; the sensitivity of the response and/or the sensitivity in the suitability. This function is not used in this thesis. A schematic representation of the functions are depicted in figure D.1.

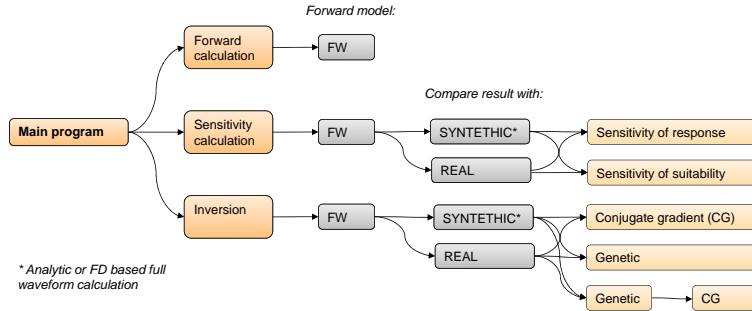


Figure D.1: Schematic figure of the functions of the Fortran program. The grey boxes represent options, and the orange boxes represent the different subroutines.

D.2 Program outline

The full waveform calculation uses the coefficient matrix M and each of the main components use the same forward model. The structure of the program is such that changes made to the program only need to be defined in one subroutine. For example a change in matrix M needs to be defined in one subroutine and is used by all subroutines that require M . A Schematic representation of the program outline is depicted in figure D.2.

D.3 Short explanation of the subroutine

Main program: The main program is responsible for the overall handling of the program; defining all properties, setting and saving the settings and calls to the different subroutines all start from the main program. Here the settings for the forward calculation and the inversion algorithm must be applied. Here the choice of measurement data must be defined before the program is started; either hydrophone data or geophone data is used. The hydrophone data option uses surface response of pressure where the geophone data uses the response of velocity.

Commonblock: This is not a subroutine, but a module used to declare variables. Each subroutine that uses the Commonblock is able to change and/or use the variables in this module. Since almost all subroutines make use of Commonblock, it

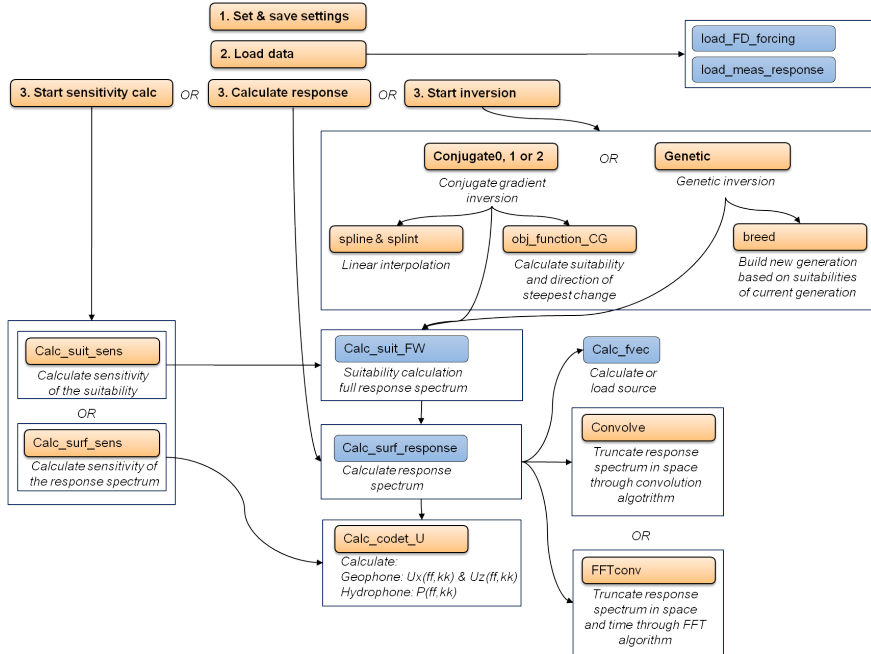


Figure D.2: Schematic representation of the program outline showing all dependencies and functions of the different subroutines. An arrow represents a call to a subroutine. The blue color means that this subroutine is specific for the full waveform approach, orange represents a general subroutine of the program.

can also be seen as some kind of ‘global’ memory. It includes all important indices defining the type of calculation made, general filepaths, background properties, and specific settings for the different subroutines. Most of the variables themselves get an explicit value in the **main program**.

Conjugate Gradient: Nonlinear(0),(1) or linear(2) CG scheme, basics of the nonlinear scheme. For a detailed view regarding this topic reference is made to [6]. This local search method is not used in this thesis.

Genetic: Genetic inversion scheme, see figure D.3 for parallelized general scheme.

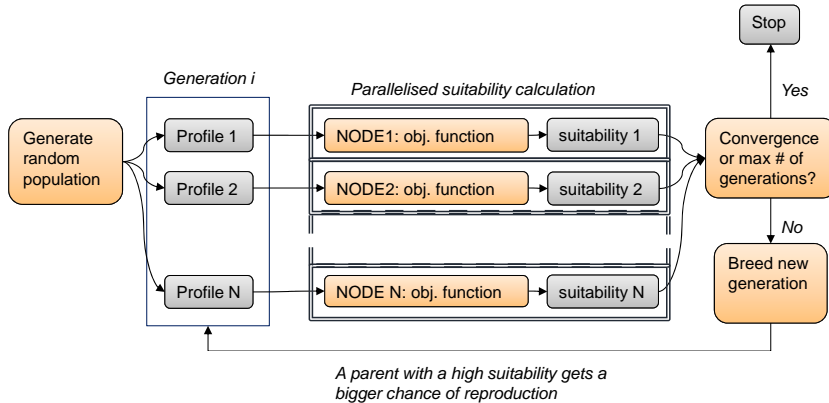


Figure D.3: Schematic representation of reproduction applied in the genetic scheme, based on the suitabilities of the different profiles.

Breed: The breed function needs both the population with all different profiles, and the suitabilities of these profiles to build a new generation. This is done via tournament selection, which is followed by crossover and single mutations. The selection and mutation is schematically drawn in figure D.4.

Suitability calculation: The suitability calculation is explained in section 3.1 for the comparison of (surface) wave spectrum. Basically, the routine **calc suit FW** calculate the suitability for a specific shear wave velocity profile and/or compressional wave velocity profile. Other soil properties are global variables, and therefore known in any subroutine that uses the **Commonblock**.

Calc surf response: Calculates the response spectrum as explained in section 2.3.

Calc codet U: This is the most important subroutine for the calculation of the response; it includes the response matrix M for a number of configurations regarding number of soil layers and halfspace or rigid bottom boundary conditions closing the domain. The input includes; soil profile properties, the applied forcing, wavenum-

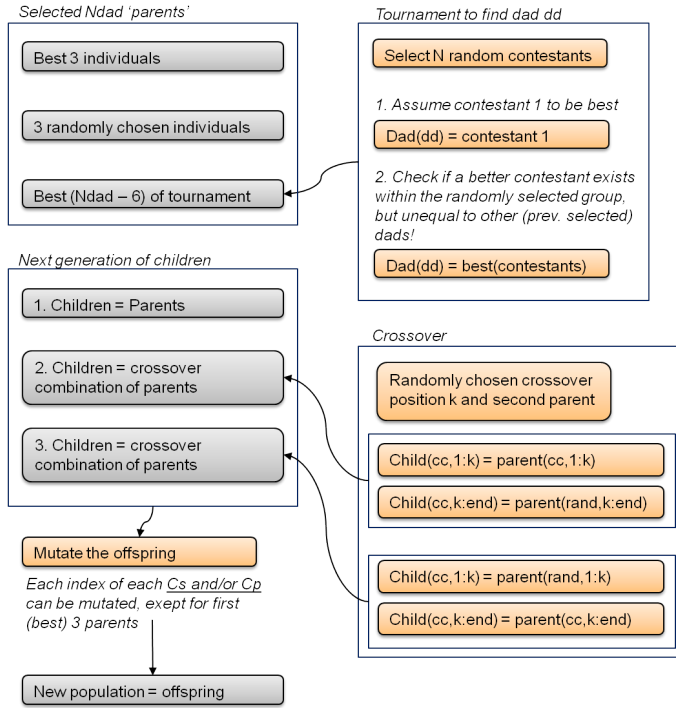


Figure D.4: Schematic representation of reproduction applied in the genetic scheme, based on the suitabilities of the different profiles.

ber, frequency and configuration indices. For this input, the output of this function is the displacements for a given frequency and wavenumber.

D.3.1 Truncation

The program can take into account the influence of receiver length in two different ways; either by a FFT based convolution or a general convolution algorithm. The FFT based convolution allows the truncation in space and time, as well as processing of data in xt domain. The convolution algorithm is limited to receiver length. A schematic representation of the general process is found in figure D.5.

FFTconv: This routine takes the surface response spectrum and uses the FFT algorithm **fft—old** for the two dimensional Fourier transform that allows the truncation of the signal in offset and time. The input of the signal requires powers of two for the number of steps taken in frequency and wavenumber. For pressures and vertical velocity the program only requires the spectrum of positive wavenumbers and frequencies, since these signals are symmetric across wavenumbers and the xt domain signal is real valued, provided that the model is symmetric i.e. horizontally stratified. However, for horizontal velocity or a non-symmetric model the input requires negative as well as positive wavenumbers. This subroutine also provides the possibility to process the data in xt domain; windowing and scaling can be applied in this routine, for consistency these processes must be the same as applied to the measurement data. The characteristics of these processes must be applied in this subroutine. A schematic overview of the processes are given in figures D.6 and D.7. The processes consist of two steps: the first step is the truncation of the data and the second step is the application of the scaling and windowing to the truncated result obtained in step 1.

Convolve: The convolution algorithm can be used to take into account the influence of receiver length. A window must be applied before the start of the inversion, this can either be calculated or defined externally.

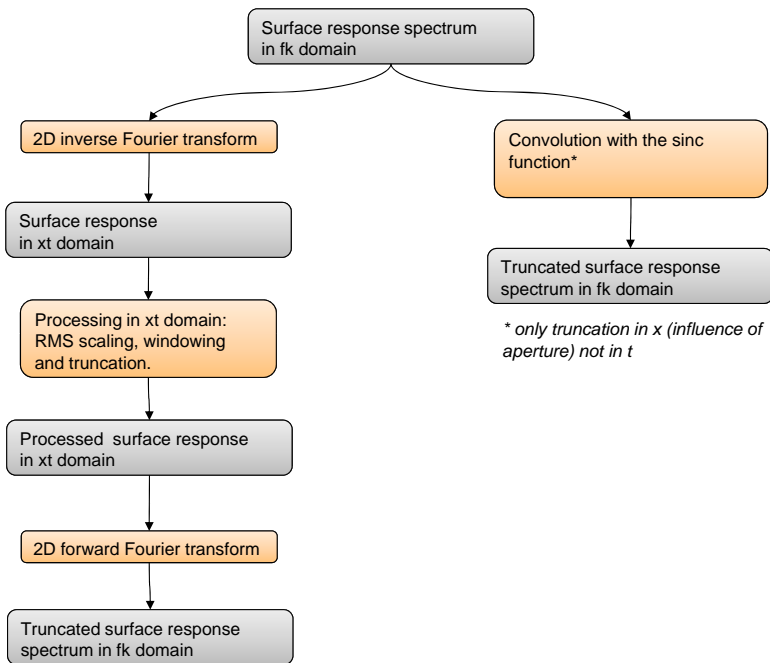


Figure D.5: Schematic representation of the processes used to truncate the calculated response spectrum.

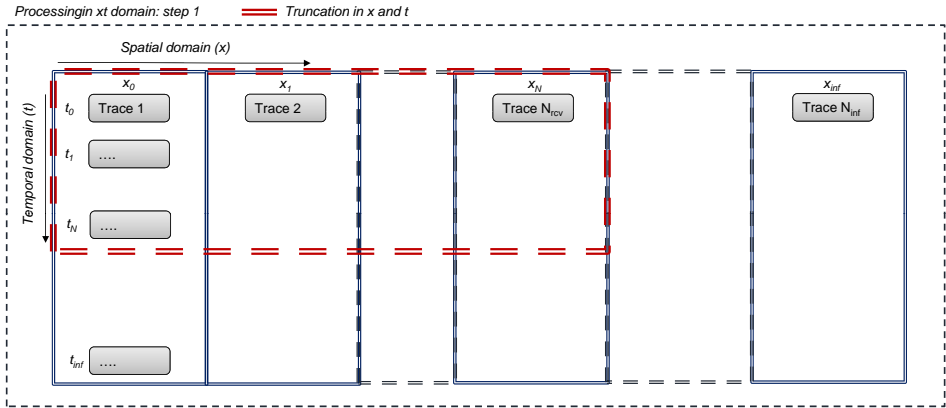


Figure D.6: Schematic representation of the truncation process based on FFT.

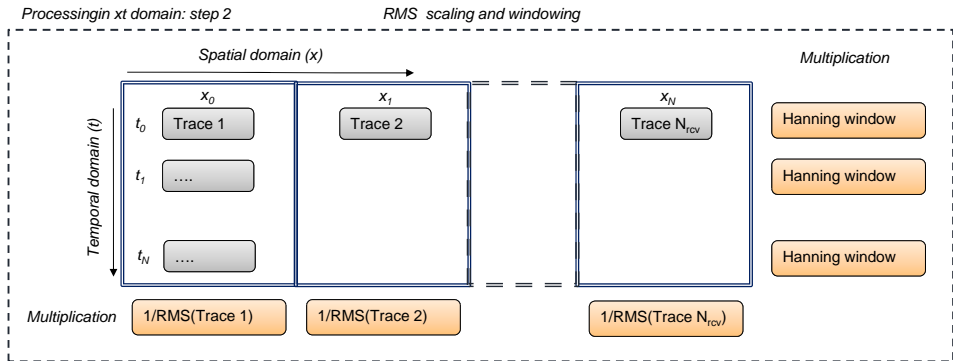


Figure D.7: Schematic representation of the processes applied in the xt domain.

D.4 Basic input and output of the program

D.4.1 Input

Almost all of the variables used in the program can be defined in the **main program**, but the calculation also needs some external files:

- **External source spectrum**, unless the Ricker wavelet is used, the program needs both a specific folder referring to the measurement data or synthetic data (to be provided as *FDID*, the length of the folder name is to be provided in the **Commonblock**). This folder contains the source function, the source spectrum data consist of an amplitude file, and an accompanying file containing the frequency steps used for the amplitudes.
- **Measurement response spectrum or external synthetic response spectrum**, or more specifically; the *fk*-transformed measured pressure or velocities in both *x*- and *z*-direction, together with two files giving the wavenumber and frequency points on which the data is defined. Both the folder where the data can be found, *FDID*, as the specific first part of the filename *FDspec* need to be provided in the main program. The length of both characters needs to be given in **Commonblock**. For this calculation, it is important to set *fact ff* and *fact kk* to 0.
- **FW response** In case of inversion based on a result of a single forward calculation, the result of this forward needs to be available in the RESULTS directory that is used for the inversion as well. (This is automatically the case if the version, profile and number of soil layers is not changed after calculating the soil response spectrum).

D.4.2 Output

Depending on the calculation started, the program provides several output files. To start, for each combination of the program *version*, the number of soil layers *n soil*, and profile *profile* a separate results directory is build in the general RESULTS folder. Two files that are always generated are:

- **'Program settings version'**: showing all important program settings used for that particular run of the program.
- **'Soil input props version'** shows the soil input properties used for the inversion.

The result of the response calculation contains a file with the response spectrum for the full waveform calculation. The genetic inversion saves four files per 10 generations:

1. **'Cs pop generation i '** and/or **'Cp pop generation i '** Containing all the shear wave velocity vectors of compressional wave velocity in generation i
2. **'Cs suit generation i '** and/or **'Cp suit generation i '** Containing the suitability of the shear wave velocity vectors and the compressional wave velocity in generation i
3. **'Cs pop mean - stdv generation i '** and/or **'Cp pop mean - stdv generation i '** Containing the mean and the standard-deviation of that population.
4. **'Cs Distance i '** and **'Cp Distance i '** Containing the distance in the population (a numerical expression for the convergence of the profile), and the error. The error is calculated in a comparison with the actual shear- or compressional wave velocity profile, and therefore only makes sense if this profile is known i.e. not usable in the inversion of actual measurement data.

Appendix E

Additional inversion results

This appendix shows several additional results that were not incorporated in the report. The results mostly concern longer runs of the performed runs in chapter 5. In addition, a run using the spectrum of the first trace resembling the source input was performed.

The settings for the forward model and inversion algorithm are displayed in tables E.1 and E.2.

Table E.1: Settings for forward model of inversion.

Settings	df/dt	f_{max}/T	dk/dx	k_{max}/X	n_t	n_x
	Hz/s	Hz/ms	m^{-1}/m	m^{-1}/m	-	-
Forward model	9.766e-2/5	99.9/4	5.05e-4/0.97	0.518/237	2048	2048

Table E.2: Settings for inversion program.

Settings	Gen.	Pop.	$\#_{conts}$	P_{mut}	$\#_{dads}$
	-	-	-	-	-
Genetic algorithm	150	90	35	0.25	30

E.1 Additional run 1

The source function used is a Ricker wavelet with central of 20 Hz. The run performed used a pre-defined soil profile based on the outcome of run 4 in chapter 5 displayed in table E.3.

Table E.3: Pre-defined profile and the search ranges for the algorithm considered for run 5.

	Run	4
$c_{s,range}^{(1)}$	m/s	100 ± 50
$c_{s,range}^{(2)}$	m/s	100 ± 50
$c_{s,range}^{(3)}$	m/s	100 ± 50
$c_{s,range}^{(4)}$	m/s	405 ± 300
$c_{s,range}^{(5)}$	m/s	617 ± 300
$c_{s,range}^{(6)}$	m/s	180 ± 100
$c_{s,range}^{(7)}$	m/s	365 ± 100
$c_{s,range}^{(8)}$	m/s	281 ± 100
$c_{s,range}^{(HS)}$	m/s	800 ± 300

Only 9 results are found that have a suitability higher than 0.5. This suggest that convergence is still not reached. The large increase in suitability is completely dominated by an better fit of the higher modes as can be seen in figure E.2.

Table E.4: Results of inversion run 5.

Soil layer i	$c_{s,i}^{(best\ fit)}$	$\bar{c}_{s,i}^{(pop.best)}$	$\sigma_{s,i}^{(pop.best)}$
	m/s	m/s	m/s
-	100	98.8	20.7
1	50	57.8	13.4
2	50	52.2	6.3
3	400	375.6	92.7
4	905	848.3	86.7
5	125	164.4	50.5
6	445	407.2	52.2
7	410	381.1	29.6
8	825	900.6	124.7
HS			

A further increase in suitability is found and resulted in a value of 0.58. The best fitted result of shear wave profile is displayed in figure E.1 and table E.4. An even higher phase velocity behavior was found at layer 5 of over 900 m/s . Furthermore, the result layer 6 decreases to a velocity of 125 m/s .

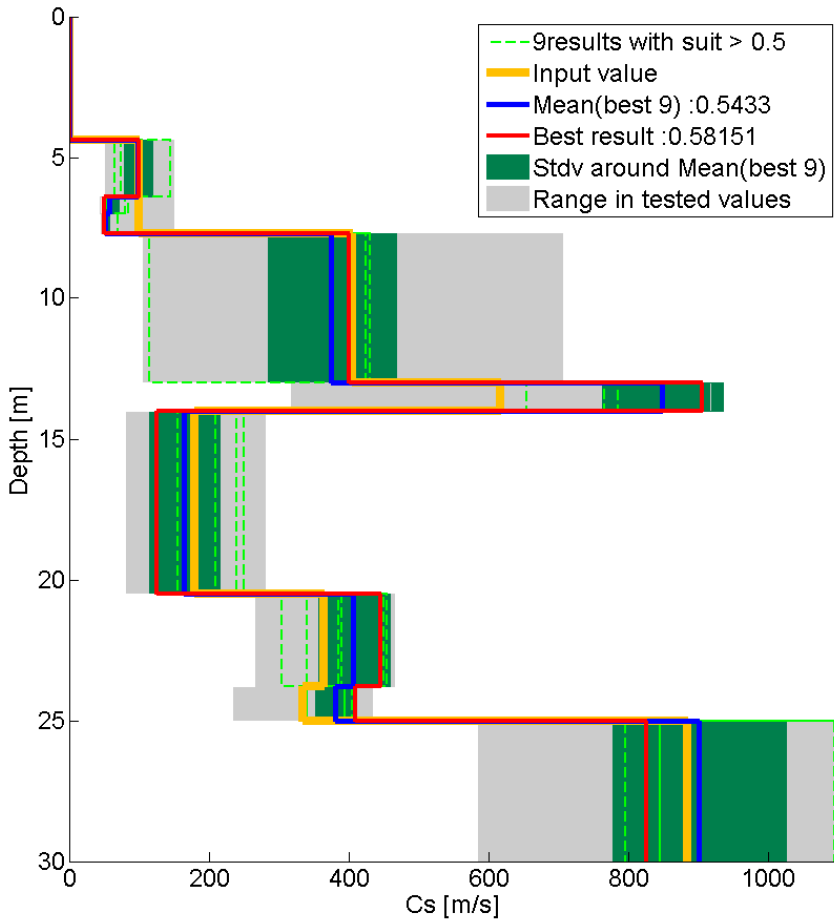


Figure E.1: Results of the inversion of shear wave velocity for run 5

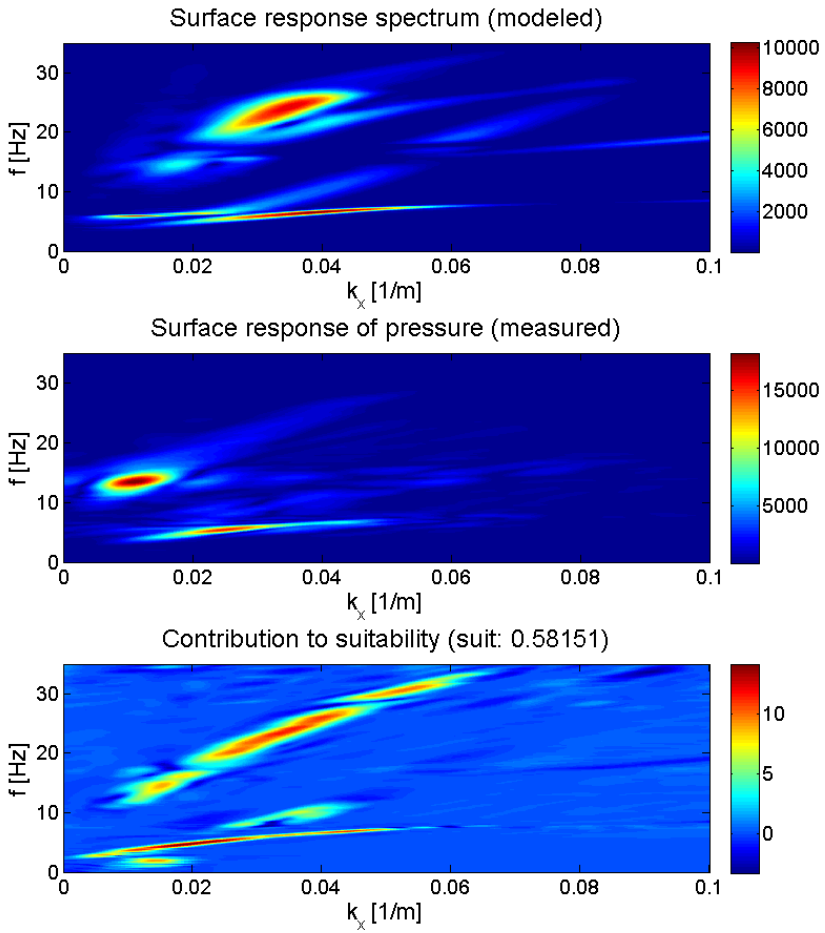


Figure E.2: Dispersion spectrum of best fit result of inversion run 5 compared to the measured spectrum. The contribution to the suitability is plotted in the bottom inset.

E.2 Additional run 2

The source function used for this run was the absolute valued Fourier transform representation of the first trace signal. The run used the same pre-defined soil profile as the first additional run and is displayed in table E.3. The results show a value of approximately 0.52 for the best fit result and 8 results are found with a fit higher than 0.45.

The general profile found is quite similar to the first run, although the values do not correspond completely. The velocity found in the layer exceeds 1100 m/s and is fairly high for shear wave velocities found in general. However, the layers 5 and 7 seem to converge completely for the 8 results found. A proper fit is not found through a better representation of the actual source function. It could be interesting to invert the source function as well, as mentioned in the recommendations.

Table E.5: Results of inversion run 6.

Soil layer i	$c_{s,i}^{(best\ fit)}$	$\bar{c}_{s,i}^{(pop.\ best)}$	$\sigma_{s,i}^{(pop.\ best)}$
-	m/s	m/s	m/s
1	100	98.8	3.3
2	55	60.0	15.2
3	50	55.6	6.0
4	405	409.47	14.9
5	905	818.8	4.6
6	170	179.4	134.7
7	415	416.3	21.1
8	430	392.5	68.7
HS	1155	911.3	193.7

The SRS show a completely different energy distribution. The higher modes are less present in the data and is probably caused by the energy distribution of the source function across frequency. When comparing the spectra of measured and modeled response, presented in figure E.4, it seems that the higher modes are less present and suggest a worse fit. However, due to the source in-dependency of the suitability the higher modes match almost as well as the previous run.

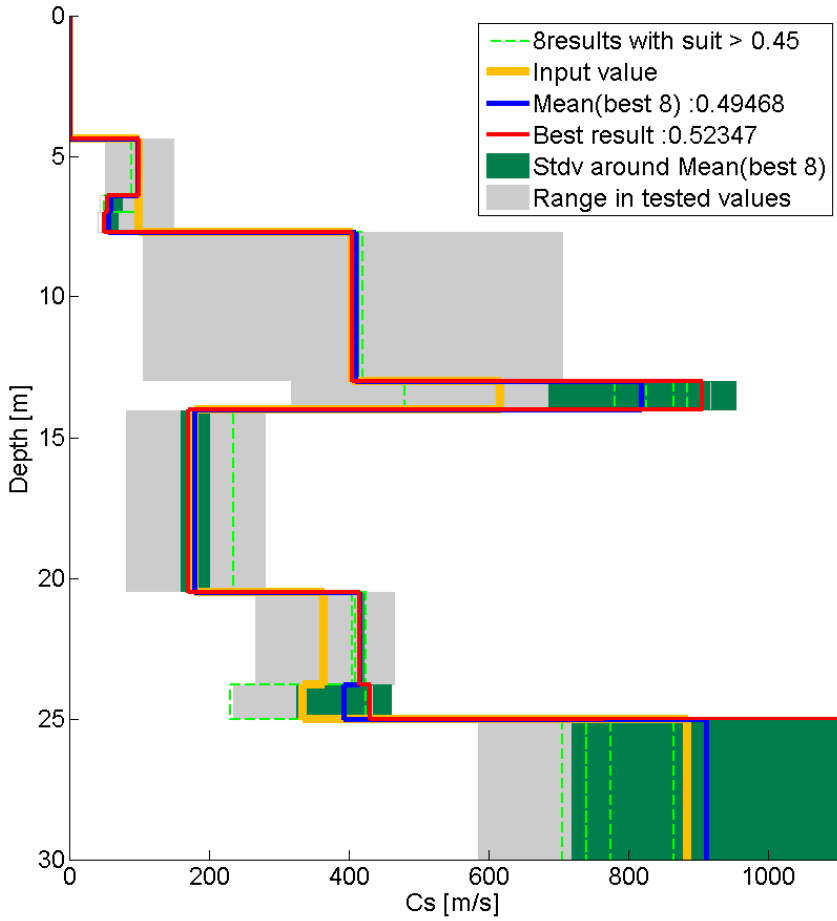


Figure E.3: Results of the inversion of shear wave velocity for run 6

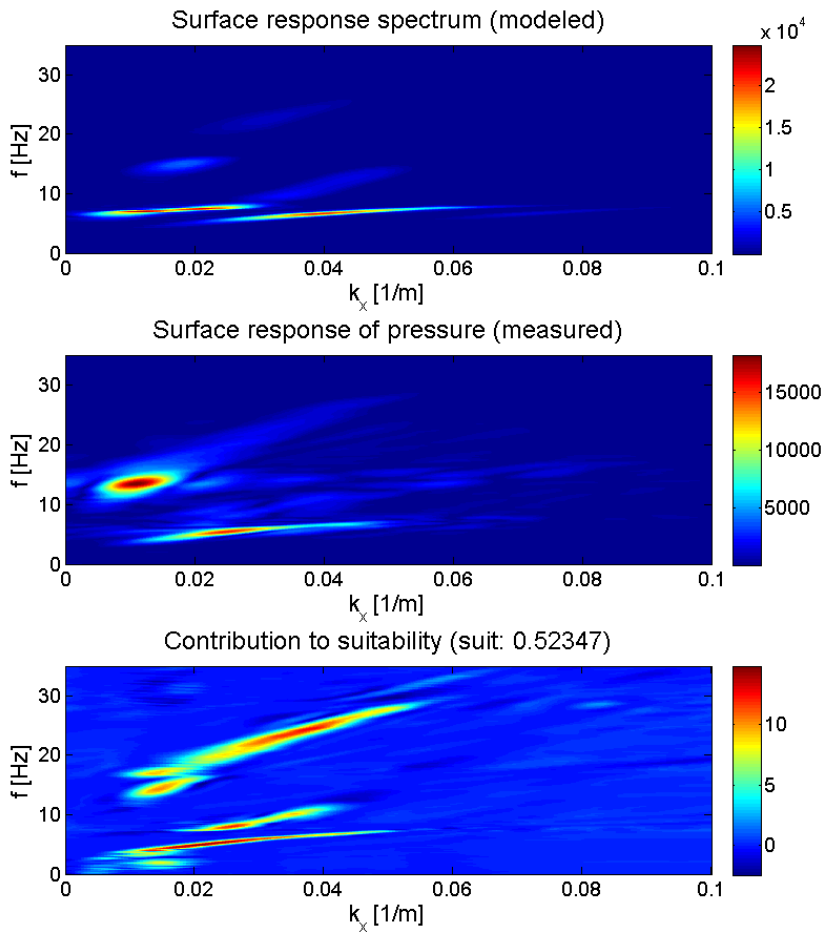


Figure E.4: Dispersion spectrum of best fit result of inversion run 6 compared to the measured spectrum. The contribution to the suitability is plotted in the bottom inset.

Appendix F

Possible improvements

During measurements possible improvements were observed and are summarized in this appendix.

- For a better measurement of streamer location and airgun shot locations, D-GPS receivers could be attached to the buoys. This will also decrease the amount of pre-processing of the datasets.
- Due to the large amount of shots that need to be performed larger compressors could be part of the equipment. This reduces the amount of time required for the air tanks to be filled for a next set of shots. In addition, a more efficient use of the air should be implemented especially when the airtight seal was compromised due to accumulation of dirt.
- The approach for the deployment of the receiver is best implemented as follows: the measurement vessel should be anchored up-wind and the propulsion should be disengaged. The streamer will then be transferred to the survey vessel, which will deploy the streamer. The streamer will be deployed in direction of the wind. A sufficiently large anchor should be used to anchor the measurement vessel, a lot of precious measurement time was used to ensure anchoring of the vessel.
- The sparker source does not work in the fresh water surrounding of the IJsselmeer.
- The airgun locations should be implemented after the deployment of the streamer. The airgun shots should be provided in line with the streamer. Enough time is available between consequent shot locations to implement the coordinates in the GPS system.

- The captains of the boat should be informed in an earlier stage of the project, especially with respect to the tools required. The practical insight these people provided would have allowed a more efficient measurement when these insights would have been provided in an earlier stage.
- An investment should be made regarding airgun frames. Multiple frames for different airguns would increase the amount of effective measurement time, since a lot of measurement time was lost in replacing the airguns.
- Invest in a larger time window for the measurements. Usually a week is too small to perform a proper seismic measurement. In a different view also more preparation must be done in advance, since a lot of equipment did not work properly.

Bibliography

- [1] K. Aki and P.G. Richards. *Quantitative seismology*. University science books, 2002.
- [2] S.A. Badsar. *In situ determination of material damping in the soil at small deformation ratios*. PhD thesis, Department of structural mechanics, Civil Engineering, Katholieke universiteit Leuven, 2012.
- [3] D Boiero, C Strobbia, L Velasco, and P Vermeer. Guided waves-inversion and attenuation. In *75th EAGE Conference & Exhibition incorporating SPE EUROPEC 2013*, 2013.
- [4] Daniele Boiero, Margherita Maraschini, and LV Socco. P and s wave velocity model retrieved by multi modal surface wave analysis. 2009.
- [5] A.K. de Groot. Determination of dynamic soil properties from in-situ offshore low-frequency seismic measurements. Master's thesis, Delft University of Technology, 2014.
- [6] C.E. de Winter. Inversion of near-surface seismic measurements to estimate soil stiffness relevant for offshore wind turbines. Master's thesis, Delft University of Technology, 2014.
- [7] G.G. Drijkoningen and D.J. Verschuur. Seismic data processing, 2003. Center for Technical Geoscience, Civil Engineering, TU Delft.
- [8] Fabian E Ernst and Gérard C Herman. Tomography of dispersive media. *The Journal of the Acoustical Society of America*, 108(1):105–116, 2000.
- [9] FE Ernst. Multi-mode inversion for p-wave velocity and thick near-surface layers. In *14th European Meeting of Environmental and Engineering Geophysics*, 2008.

- [10] Sebastiano Foti, Carlo G Lai, Glenn J Rix, and Claudio Strobbia. *Surface wave methods for near-surface site characterization*. CRC Press, 2014.
- [11] Sebastiano Foti, Luigi Sambuelli, Valentina L Socco, and Claudio Strobbia. Experiments of joint acquisition of seismic refraction and surface wave data. *Near surface geophysics*, 1(3):119–129, 2003.
- [12] A. Gisolf and D.J. Verschuur. *The principles of quantitative acoustical imaging*. Eage Publ. by, 2010.
- [13] D. Grotegoed, W. Bleijenburg, and D. Bouwmeester. Determination of py curves for monopile foundations, 2012. Geophysical report Ballast Nedam, DISSTINCT.
- [14] J Lubbers and R Graaff. A simple and accurate formula for the sound velocity in water. *Ultrasound in medicine & biology*, 24(7):1065–1068, 1998.
- [15] M Malinowski, S Operto, and Alessandra Ribodetti. High-resolution seismic attenuation imaging from wide-aperture onshore data by visco-acoustic frequency-domain full-waveform inversion. *Geophysical Journal International*, 186(3):1179–1204, 2011.
- [16] Everhard Muyzert. Near surface models derived from ground roll, guided waves and scholte waves. In *69th EAGE Conference & Exhibition-Workshop Package*, 2007.
- [17] Claudio Piatti, LV Socco, Daniele Boiero, and Sebastiano Foti. Constrained 1d joint inversion of seismic surface waves and p-refraction traveltimes. *Geophysical Prospecting*, 61(s1):77–93, 2013.
- [18] Vincent Prioux, Romain Brossier, Stéphane Operto, and Jean Virieux. Multiparameter full waveform inversion of multicomponent ocean-bottom-cable data from the valhall field. part 1: imaging compressional wave speed, density and attenuation. *Geophysical Journal International*, page ggt177, 2013.
- [19] Vincent Prioux, Romain Brossier, Stéphane Operto, and Jean Virieux. Multiparameter full waveform inversion of multicomponent ocean-bottom-cable data from the valhall field. part 2: imaging compressive-wave and shear-wave velocities. *Geophysical Journal International*, page ggt178, 2013.
- [20] M. Schevenels, G. Lombaert, and G. Degrande. Determination of the dynamic soil properties by refracted p-wave and surface wave characterization at a site

- in lincent (belgium), 2011. Department of structural mechanics, Civil Engineering, Katholieke universiteit Leuven.
- [21] Steven W Smith. *Digital signal processing: a practical guide for engineers and scientists*. Newnes, 2003.
- [22] L.V. Socco, S. Foti, and D. Boiero. Surface-wave analysis for building near-surface velocity models established approaches and new perspectives. *Geophysics*, 75(5):75A83–75A102, 2010.
- [23] Chauveau. T. Geophysical report disstinct research project wind farm westermeerwind, ijsselmeer, the netherlands, 2015. Geophysical report Fugro Geoservices, DISSTINCT.
- [24] Daniel Trad, Tadeusz Ulrych, and Mauricio Sacchi. Latest views of the sparse radon transform. *Geophysics*, 68(1):386–399, 2003.
- [25] C. van Dongen. Slides advanced wave propagation. TU Delft, 2013.
- [26] W.G. Versteijlen and S.N. Voormeeren. Efficient support structure design through improved dynamic soil structure interaction modeling, 2013. Project proposal, DISSTINCT.
- [27] C.P.A. Wapenaar and A.J. Berkhout. *Elastic wave field extrapolation: Redatuming of single-and multi-component seismic data*, volume 2. Elsevier Science, 1989.
- [28] Jianghai Xia, Richard D Miller, Choon B Park, and Gang Tian. Inversion of high frequency surface waves with fundamental and higher modes. *Journal of Applied Geophysics*, 52(1):45–57, 2003.

